

ADVANCED NANOSTRUCTURES FOR ENERGY STORAGE AND CONVERSION

by

ROBERT JOHN WAINRIGHT

(Under the Direction of Ramaraja Ramasamy)

ABSTRACT

For the purpose of energy conversion from the hydrogen oxidation reaction (HOR) and oxygen reduction reaction (ORR), never-before synthesized platinum-cobalt nanowires grown on activated carbon were applied to a rotating ring-disk dual-electrode (RRDE) to study their performance, efficiency, and kinetics toward the ORR compared to a benchmark commercial catalyst.

Also, majority {010} facet growth-directed lithium iron phosphate (LFP) was produced by a solvothermal synthesis via capping agents to host short lithium diffusion distances in lithium ion battery (LIB) cathodes for increased specific capacity at high power rates. The ultrathin nanosheets produced were characterized by SEM, TEM, AFM, XRD, Raman spectroscopy, and electrochemically tested by cycling them between two voltage thresholds. Further, multiple carbon-addition techniques were employed to enhance conductivity and charge transfer to the nanosheet active material. These ultrathin, micron-sized nanosheets synthesized from a bottom-up approach, yielding the thinnest to date, 12 nm profile in the direction of lithium diffusion.

Keywords: Nanosheet, Nanoplatelet, Nanowire, Growth Directed, Capping Agent, Electrocatalyst, Power Density, Alloying, Electrochemical Cell, Coin Cell, Graphene

ADVANCED NANOSTRUCTURES FOR ENERGY STORAGE AND CONVERSION

by

ROBERT JOHN WAINRIGHT

B.S. Agricultural Engineering (Electrical/Electronics and Mechanical Systems),

University of Georgia, 2013

A Thesis Submitted to the Graduate Faculty of The University of Georgia

in Partial Fulfillment of the Requirements for the Degree

MASTER OF SCIENCE

ATHENS, GEORGIA

2015

© 2015

Robert John Wainright

All Rights Reserved

ADVANCED NANOSTRUCTURES FOR ENERGY STORAGE AND CONVERSION

By

ROBERT JOHN WAINRIGHT

Major Professor: Ramaraja Ramasamy

Committee: Tina Salguero
 Zhengwei Pan

Electronic Version Approved:

Suzanne Barbour
Dean of the Graduate School
The University of Georgia
August 2015

DEDICATION

My deepest gratitude goes to my friends, family, fellow students and peers, as well as professors who constantly gave their thoughts, time, and energy to help guide me through this degree. Without their amiable demeanors and words of encouragement and advice, these projects would have seemed much more difficult and may have never progressed as far nor taught me nearly as much!

I would like to give special thanks to my lab mates' positive attitudes and elevating thoughts and actions. Thank you all for offering me your friendship and always lending support by taking the time to listen and provide optimistic feedback despite your hectic schedules. Thank you all so much for teaching me everything you did about science, for opening up and sharing yourselves, your cultures, and for genuinely caring about me and my research/experimentation and giving helpful suggestions and guidance to stay focused on the goal of graduation, even when things frequently did not go as planned. Many thanks to a true electrochemist/experimentalist, Yogeswaran Umasankar AKA "Yogesh" (our former Post Doc.), Naren (my biotechnologist ☺), Jarryd (thanks for revising my writing and it's been a pleasure experimenting with a chemist), Yi Fang (thanks for the car rides, ordering supplies, and friendship), Yan Zhou (also thank you for the car rides, friendship, and chemistry expertise ☺), Maryam (helped me with battery material synthesis), Veronica (helped me with fuel cell catalyst synthesis), David (set up the fuel cell test station so I didn't have to ;)), Bryan (thanks for running the lithium ion battery project I partly designed so I didn't have to), Leigh Karas, and Nick Stom. Thanks for the fun Spring 2014 Electrochemical Society Conference Dr. Ramasamy, Yogesh, Naren, Yi, and Yan!

I am also extremely grateful for my immediate family for always listening, even when they knew nothing about my experimental difficulties. Thank you so much to my Mom, Dad, and older brother, Reeve, for always being there for me and constantly reminding me that all of the struggles of research were only temporary and that this would be over before I knew it and to simply enjoy the journey and exposure to equipment while it lasted: you were right; the time flew by and now that things started to click, I wish I had longer here to learn and take advantage of the equipment and experienced and knowledgeable students and professors.

It will be strange for me to soon never again walk through the door of the Nano-Electrochemistry Lab (NEL) at The University of Georgia and greet all of my lab mates in the same place at the same time and never again have the freedom and equipment to study nanomaterials for energy under the direction of a professor that extended me creative freedom to study areas of personal interest in nanoscience and electrochemistry.

Thus, I attribute virtually all success herein to my principal investigator (PI) and mentor, with whom it was a great pleasure working for the past three years, Dr. Ramaraja P. Ramasamy. Through his advisership and consultation, I have apprenticed to become an electrochemist and nanoscientist in the fields of materials science and energy storage and conversion. One of the biggest privileges I was given was being able to work in the areas in which I am interested: inorganic nanomaterials for electrochemical energy storage and conversion, such as lithium ion batteries and nano-electrocatalysts. I will forever be grateful for him providing me the tutorage and opportunity to work and learn in his laboratory while making friends and colleagues as I built a well-developed, interdisciplinary research network.

It was an honor to have met and worked with those in my lab as well as other professors in our research facilities such as Dr. Zhengwei Pan (a personal mentor whom I initially befriended

on rides to and from his Nanotechnology class and our building, Riverbend Research Lab South) and his research group, as well as Dr. Tina Salguero and her students whom so kindly provided salient advice, let me reserve and share their equipment, use their supplies, and provided material characterization; I am also highly grateful to (primarily) two of her students, Timothy Pope and Gregory Neher (whom also collaborated and helped run much of the XRD, TEM, AFM, and Raman characterization as well as some nanosheet synthesis, carbon coating, battery making, etc., shown herein), who taught me so much about lithium ion batteries as well as nanosheets and materials synthesis. Matthew Davidson in the Salguero Lab also helped provide insight into the reactions and to make me feel more at-home in a lab across campus. I am also grateful for Drs. Pan (Physics and Engineering) and Salguero (Chemistry) for agreeing to serve on my committee as materials scientists/experts to help guide me in materials synthesis and characterization techniques.

Also, thank you Jared McKnight for being an awesome co-TA who would do anything above and beyond to greatly help the students as well as myself and our Fluid Mechanics professors! Also special thanks to Drs. Brock Woodson and Peter Carnell, who hired me as a TA for their Fluids classes and were great instructors and a pleasure for whom to work and provided my personal funding (minus research expenses) for the entire second year.

I am also very appreciative for all of my graduate-level course professors (including Dr. Minko, a polymers expert with whom I also formed a collaboration in superhydrophobicity via fluoro-silanation of Li3-1.7, terminology explained later) as well as everyone else that I met through different student organizations, collaborative corporations, and in daily research. I am thankful for the chance to use all of the equipment that I had access to at The University of Georgia,

as well as the chemical supplies from my own lab and borrowed from others, including the vast reserves of Dr. Jason Locklin.

Lastly but by far not least, I would like to thank my amazing girlfriend, Jessica Ozbolt, for being my closest friend, who weathered the trials and tribulations with me regarding difficulties in [my] research: synthesizing repeatable nanostructures and [the kicker] getting them to have high electrochemical activity. Thank you so very much Jessica for listening to my rather dry stories about the arduous lab days and nights, day in and day out. Thank you for having prepared dinner upon my arrival home on a near-nightly basis, for shouldering the majority of the house (and then apartment) chores, and taking care of the boys (Saint and Dozer, my knucklehead lab-mixes) when I frequently had to work from morning until bedtime (especially the second year when I TAed Fluid Mechanics on top of the usual research/experimentation and 6000 and 8000 level classes, etc.). Also, thank you for driving the majority of our vacations so I could do graduate work, and thank you so very much for all the rides to and from the Chemistry building to run experiments while avoiding the hour round-trip waiting for/riding the River's Crossing bus! Many thanks for helping me in more ways than I can name, and I will always cherish all of our wonderful memories and am truly grateful and blessed to have shared the past four years with such a heartfelt, admirable, smart and talented, wonderful person!

I would also like to thank all of my friends in Athens, including, but not limited to: Brandon Savage (my best friend whom recently started Pharmacy School at Mercer in Atlanta, Georgia), Tim Enright (we serendipitously met on the bus, and he introduced me to polymers and many ideas of nanoparticles, surface modification, and organic synthesis), Andrey Zakhara (helped watch my dogs when I was really busy), Oleksandr Trotsenko (my friend and a roommate of the former two: all in Dr. Minko's nanoparticle/polymers lab that moved down from New York a semester into my

graduate program that has made all the difference), Ricky Kerns, Corbin Newton, Ross Furlong, Ryan Furlong (these four are childhood friends from back home), Patrick, Khush Brahmhatt, Mac White, Miriam Perryman, Mark Trudgen, Michael LeCompte, David Henry, Matt Becton, Josh Willis, James Bale, (previous nine from the College of Engineering, CENGR), Evan White, Anandi, Jeremy Yatvin (previous three from Dr. Locklin's Polymers Lab), Greg Neher, Tim Pope, Matt Davidson, Matt Bloodgood (these four from Dr. Salguero's Lab), Pradip Basnet, Lu Zhu (two previous from Dr. Zhao's Lab), Emily and Kevin (Dr. Starai's Lab), Sam White, Ash, Clayton Gilbert, Mikhil Desai, and many, many more!

And again, thank you all so much to everyone who helped give me advice, worked/collaborated with me, was a friend, or merely a friendly acquaintance I saw/knew in passing!

Acknowledgements

I would like to thank Dr. Zhengwei Pan for graciously letting me use his tube furnace, giving me rides to class, letting me come talk nanotech, and most of all, for being a good friend. I would also like to thank Dr. Tina Salguero for supplying her expertise, equipment I was allowed to use, all of the resources I consumed for my research in her lab, and for her experienced/well-trained/great Ph.D. students (Timothy Pope and Gregory Neher) who helped me tremendously! Also, special thanks to everyone in my lab (Dr. Ramasamy [PI], Dr. Yogeswaran Umasankar [former Post-Doc], Jarryd Ashby, Narendran Sekar, Yi Fang, Yan Zhou, Veronica Zhang, Maryam Manouchehri, Bryan Grommersch, David Flake, Leigh Karas, and Nick Stom), all of the students in my classes, my professors, my friends, my girlfriend Jessica Ozbolt, and everyone else involved! I will always remember everything you all did to aid in my success and look forward to coming back to visit and learning of all of your successes throughout the years! I can't thank you all enough, and it would have been far more difficult and not possible without all of your support!

TABLE OF CONTENTS

Acknowledgements	xi
------------------------	----

CHAPTER 1

SYNTHESIS AND CHARACTERIZATION OF ADVANCED NANOMATERIALS	1
Nanomaterials.....	1
Materials Characterization	1
X-ray Diffraction (XRD).....	1
Scanning Electron Microscopy (SEM)	3
Transmission Electron Microscopy	4
Atomic Force Microscopy	5
Raman Spectroscopy.....	7
Fourier Transform IR Spectroscopy	9
Energy-dispersive X-ray Spectroscopy	11

CHAPTER 2

GRAPHENE: FROM SYNTHESIS TO APPLICATIONS	15
Introduction	15
Graphene Synthesis	17
Exfoliation via Intercalation Compounds.....	17
Synthesis of Graphene Oxide.....	17

Reduction of Graphene Oxide	18
Graphene from Silicon Carbide	21
Chemical Vapor Deposition.....	22
Roll to Roll Chemical Vapor Deposition.....	23
Graphene to Graphane	24
Exfoliation of Graphite	25
Applications of Graphene	25
Photo catalysis: Semiconducting Nanomaterials	27
Photovoltaics.....	28
Dye-Sensitized Solar Cells	29
Water-Splitting.....	30
Electronics.....	31
Biosensors	35
Medicine	40
Graphene in Space	41
Future Developments	42
Conclusions	42

CHAPTER 3

ADVANCED NANOMATERIALS FOR ENERGY STORAGE AND CONVERSION IN LITHIUM ION

BATTERY (LIB) CATHODES AND LITHIUM IRON PHOSPHATE SYNTHESIS AND CHARACTERIZATION	45
Introduction	45
Lithium Iron Phosphate (LFP).....	47
Hydrothermal Synthesis of LFP.....	48
Solvothermal and Hydrothermal Syntheses and Suppression of LFP Growth in the <010>	51
Experimental Synthesis of LFP Nanosheets.....	53
Results.....	54
Raman Characterization.....	68
Conclusions	69

CHAPTER 4

LITHIUM IRON PHOSPHATE NANOSHEET ELECTROCHEMICAL EVALUATION IN LITHIUM ION

BATTERY (LIB) COIN CELLS	70
Lithium Ion Diffusion Coefficient in LFP.....	73
Conductivity	73
Experimental.....	74
Preparation of LFP-NS/C	74
Surface Carbon Coating	74
Graphene Addition.....	76

Battery Assembly.....	77
Battery Preparation	79
Results.....	80
Conclusions	82

CHAPTER 5

PLATINUM AND PLATINUM-COBALT NANOWIRES FOR ENERGY CONVERSION IN PROTON

EXCHANGE MEMBRANE FUEL CELLS (PEMFCs)	84
An Introduction to Proton Exchange Membrane Fuel Cells	84
Electrochemistry of Hydrogen Fuel Cells	86
Non-Noble Metal Catalysts.....	90
Small Diameter Supported Platinum Nanowires.....	91
Mixed Composition Nanowires.....	92
Core-Shell Nanostructures.....	93
Hollow Nanostructures	94
PtCo/C Nanoparticle Synthesis	95
Carbon Functionalization	96
Experimental Synthesis of PtNWs/C.....	96
Experimental Synthesis of PtCoNWs/C.....	97
Catalyst Ink and Electrode Preparation	98

Electrochemical Characterization	98
Results and Discussion	99
Characterization	99
Electrochemical Analysis.....	104
Conclusions	113
APPENDIX	115
Appendix Figures.....	115

CHAPTER 1

SYNTHESIS AND CHARACTERIZATION OF ADVANCED NANOMATERIALS

Nanomaterials

Recent advances in materials synthesis have led to much invested interest in their synthesis and characterization in pursuit of novel properties. Nanomaterial uses range from increasing surface area to catalyzing chemical reactions to providing new and interesting properties like superhydrophobicity, superconductivity, and plasmonic resonance. These and other interesting traits have drawn much attention to controlled and scalable synthesis of nanomaterials.

There have been many successful techniques devised to synthesize nanomaterials. Many approaches are available to synthesize nanostructures of controlled morphology, including aqueous phase synthesis (capping agents, emulsions, stabilizers), aqueous/organic solvent interface synthesis, hydrothermal or solvothermal synthesis, polyol reduction, chemical vapor deposition (CVD), metal-organic chemical vapor deposition (MOCVD), thermal vapor deposition (TVD), physical vapor deposition (PVD), electrodeposition, extreme ultraviolet lithography (EUVL), focused ion beam (FIB) machining, directed self-assembly (DSA), molecular beam epitaxy (MBE), atomic force microscopy (AFM), nano-printing, atomic layer deposition (ALD), vacuum arc deposition, solid-state synthesis, vapor-liquid-solid (VLS) method, etc.

Often, wet synthesis methods are more practical from an industrial standpoint to scale up synthesis in bulk batches, whereas other techniques feature much more slow growth of the nanostructures, like CVD, where nano- or micro- structures are deposited on a surface and are

limited to the available surface area and slow growth-kinetics due to low-density chemical species in the gas-phase. Therefore, from an engineering, practical product development standpoint, often, a wet-phase or solution-based synthesis offers a much larger scale of production and can produce structures more economically than gaseous-state reactions.

Materials Characterization

There are many materials characterization techniques that are often employed to gather information about synthesized or unknown materials. For brevity and relevance, only the major characterization techniques used herein will be discussed, but there are numerous other methods that can be similarly utilized to gain further understanding of materials.

X-ray Diffraction (XRD)

X-rays are scattered by electrons in crystalline materials and form diffraction patterns that can be used to characterize the material by comparing it to a library of standard, known material XRD patterns. Source x-rays propagate in phase to the sample and get elastically scattered by atoms in crystalline configurations. A detector is used to detect discrete energy levels as a function of the Bragg angle. The Bragg angle (Θ) is related to the geometry between the diffraction angles by the relationship:

$$2d_{hkl}\sin\Theta = n\lambda \quad [1.1]$$

Here, d_{hkl} is the interplanar spacing in the crystal lattice, n is an integer number of wavelengths, and λ is the wavelength of the incident x-rays.¹

This was discovered by W.H. Bragg and W.L. Bragg to explain why crystal face cleavage causes different reflection angles of incidence denoted theta (Θ).¹ The geometric relationship of the equation is shown in Figure 1.1:

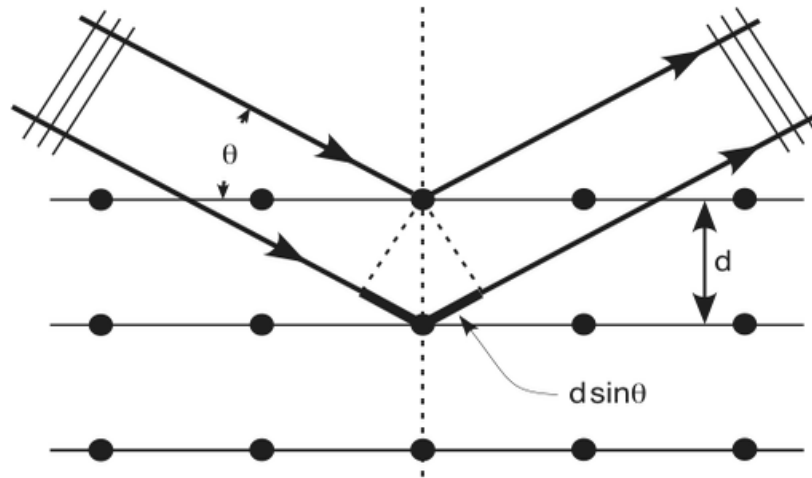


Figure 1.1. Schematic of the mechanism of Bragg diffraction.²

This is known as x-ray interference, or Roentgenstrahlinterferenzen, also known as x-ray diffraction (XRD). This is a very powerful characterization technique that is capable of characterizing periodic, repeating crystals as was hypothesized centuries earlier. This discovery was invaluable to materials characterization, and the Braggs's received the Nobel Prize in Physics in the year 1915 for characterizing the crystal structures of ZnS, NaCl, and diamond. Bragg's Law is commonly used to differentiate the x-ray scattering pattern of crystals, but the structure of all states of matter can be studied with beams from the electromagnetic spectrum, including electrons, neutrons, protons, and ions, etc., by using wavelengths of similar length to the crystal lattice spacing of the structures under study.³ This technique is one of the most powerful material crystal structure identification methods due to a highly repeatable signal that is easily matched to XRD crystallographic pattern material libraries that contain the signature patterns for nearly all known crystalline materials, allowing a material scientist the ability to check crystalline sample composition in less than thirty minutes in most cases.²

Scanning Electron Microscopy (SEM)

Scanning Electron Microscopy uses the various electron emissions from a sample which is stricken by a focused beam of electrons derived from an electron gun under ultra-high vacuum (UHV) conditions (which also prevent beam interference by gaseous species). The electron beam is focused to the sample by the condensing lenses and scanning coils, allowing the researcher to change the focus of the sample. When the electron beam hits the sample, electrons from the sample are emitted, and these secondary electron emissions can be scanned and analyzed by the electron probe microanalyzer (EPM). Figure 1.2 displays the configuration of the SEM:

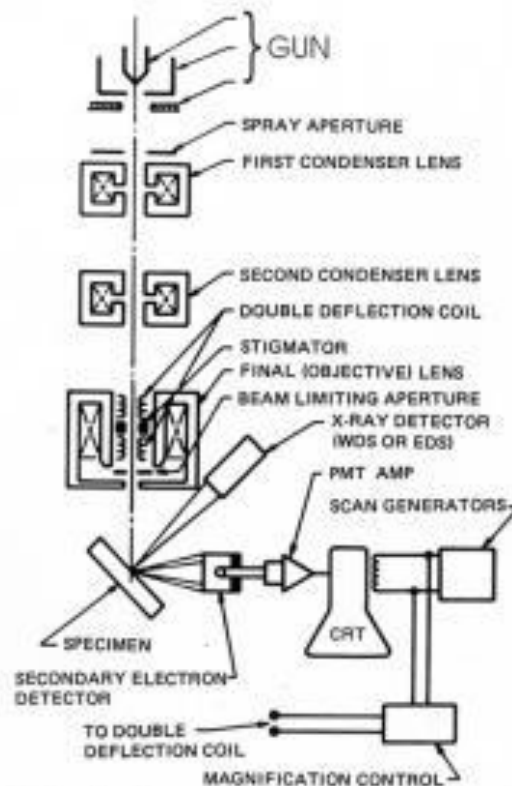


Figure 1.2. Schematic of a typical SEM design.⁴

SEM utilizes these secondary electron emissions as well as backscattered electrons from the sample to generate an image of the sample in question. By changing the excitation level of the coils, the electron beam can be increased or decreased in diameter. A lower excitation level of the

coils diffracts the electron beam less strongly, resulting in a higher-resolution image.⁵ Images of the sample are obtained through the use of the Everhart-Thornley (E-T) electron detector, capturing backscattered electrons (BSEs) and secondary electrons (SEs) with the positively charged E-T detector that collects the emitted electrons. These electrons, after interacting with the sample, are mapped via fluorescent imaging in the cathode ray tube (CRT) of the SEM. The images produced are semi-three-dimensional and allow the researcher a high resolution image that gives insight into the overall as well as surface morphology and is one of the most widely used techniques in nanomaterials characterization.

Transmission Electron Microscopy

Transmission electron microscopes (TEM) consist of an electron gun that acts as a cathode, firing an electron beam through the Weinheltd cylinder to focus the beam and adjust the resolution of the image.⁶ This beam transmits through the sample to the viewing lenses, allowing the observer to obtain the two-dimensional qualitative analysis of the sample.⁷ . The operation consists of an electrical supply that supplies high voltage to the cathode which is heated and ejects electrons under UHV; the electrons are concentrated by the first lens (electromagnetic coil) to form a more intense beam, and then a second lens (electromagnetic coil) is applied.

The specimen sits on a copper grid, and the electrons that pass through the specimen interact with the grid, and the third lens (projector lens) magnifies the image on a fluorescent screen at the machine's base. The sample may be rotated and moved using goniometers to obtain images of specific areas of the sample. Analysis of the electrons that pass through the sample consist of the intensity of the electron in question: a higher intensity electron transmission would suggest a lower mass thickness. This final TEM image is then viewed directly through either a viewing portal via binoculars on the side or a signal processor and TV monitor.⁸ TEM is another qualitative

analytical technique used to characterize samples and enhance images of organic and inorganic samples. The samples obtained in TEM are two dimensional, with analysis of the sample dependent on the darkness of the image of the sample. TEM can then be used to quantify the size-distribution of the nanoparticles of the sample by transforming the darker portions of the scans to a two-dimensional image of the sample in whole.⁹ Measurements of the nanoparticle sizes are then quantified by measuring the size of the pixels of the image.⁹ TEM allows for a higher quality resolution over SEM, and the crystal structure of the sample in question can be analyzed through selected area electron diffraction (SAED). However, these images lose one spatial dimension compared to SEM.

Atomic Force Microscopy

Atomic force microscopy (AFM) allows for the analysis of a sample's physical surface properties. An AFM microscope utilizes the force derived from a laser beam aimed at a lever which moves across a sample. The probe can maintain contact with the surface through electrical controls as it is controlled to move across the surface of the sample. As the lever moves across the sample, the force applied to the point of the lever deflects the laser, which is recorded by a photodetector.¹⁰ The photodetector then records the various angles and positions of the deflected laser off the cantilever as shown in Figure 1.3.¹⁰

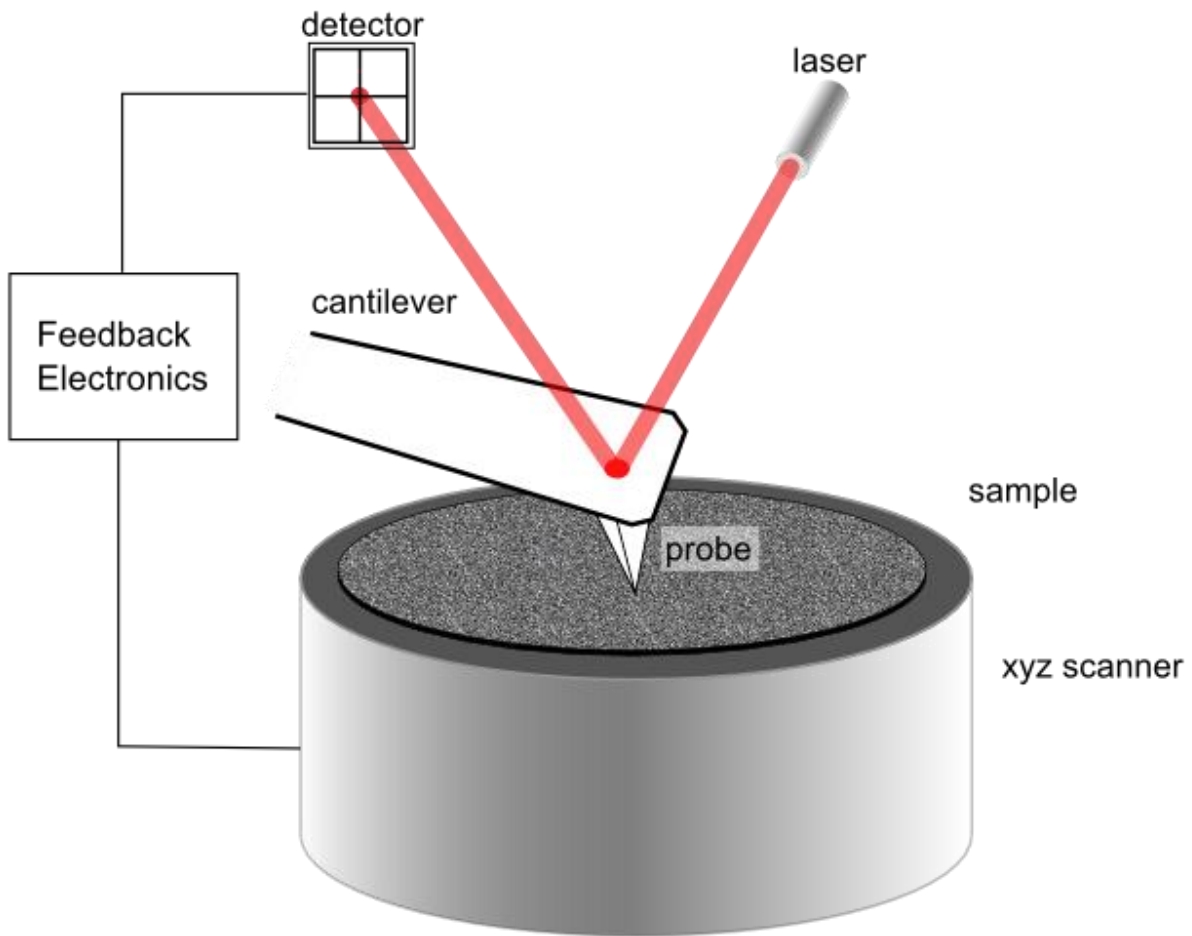


Figure 1.3. Schematic of an AFM setup.¹¹

This technique allows for a wider range of samples, as a vacuum is not needed to conduct the analysis. AFM is conducive to analyzing a broader array of media that would not be available for more volatile characterizations. Some probes can also use different properties to analyze the sample, including the magnetic field, electrical properties, or intermolecular interactions. Images obtained from the photodetector are typically displayed in a multicolored, two-dimensional layout that can then be reprogrammed into a three-dimensional display of the physical features of the surface to the level of nanometers. The different colors depict different topographical heights of the sample surface as shown in Figure 1.4.¹¹

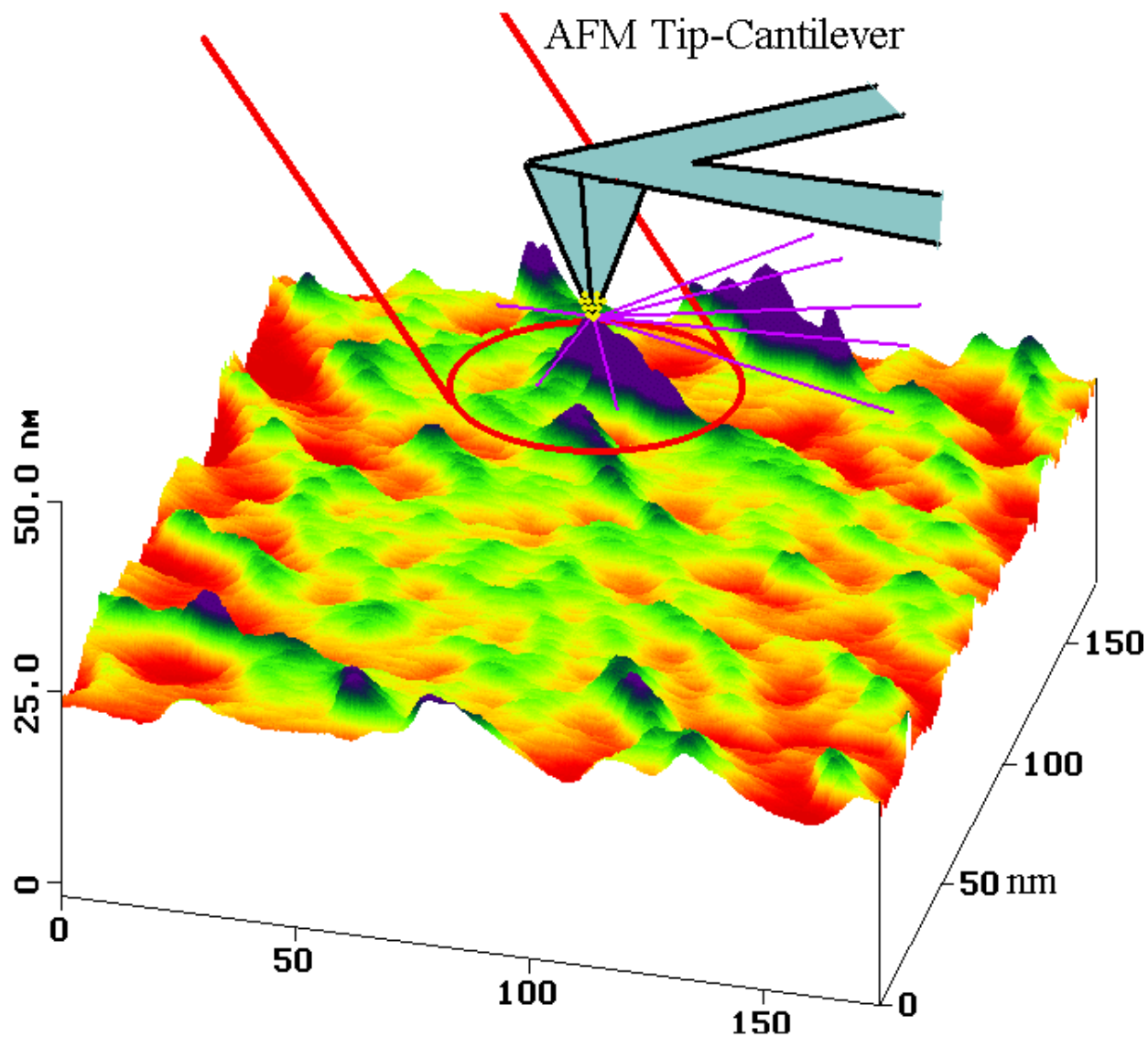


Figure 1.4. Schematic of an AFM tip cantilever and a surface.¹²

Raman Spectroscopy

Raman Spectroscopy is a technique that can be used for qualitative and quantitative analysis. When a monochromatic light source is shined on a sample, the light that scatters is almost all of a single frequency – that of the excitation source. This phenomenon can be described as elastic scattering. The rest of the light undergoes a shift in energy due to chemical interactions that occur between the incident monochromatic light and the various molecules in the sample. These

molecular bonds all contain vibrational energy of distinct characteristic levels, so when they become excited, the frequencies of scattered light vary in accordance with the percentage of types of bonds present. This is known as inelastic scattering, and the discrepancy between the two types of scattered light can be plotted to create a spectrum similar to an IR transmission. An image is shown below in Figure 1.5 that graphs them together, allowing for easy comparison of the two.¹³

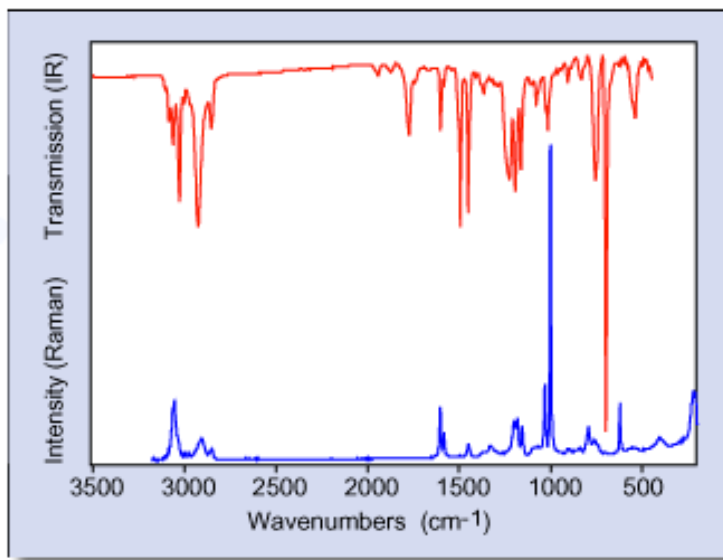


Figure 1.5. Raman Spectroscopy and IR transmission are depicted together.¹³

Because Raman bands are created by the oscillations of an induced dipole, they are not as intense as the bands that arise from symmetrical molecules. Asymmetric molecules also have bands, but because the oscillations are not as strong, they appear much weaker than their IR counterparts. IR bands are caused by the interaction of light and the dipole, but the entire difference between the two lies in the oscillating nature of symmetric molecules, as well as heavier molecules that vibrate more as well as multiple-bond vibrations.¹³

Similar to IR, Raman Spectroscopy can measure a sample's chemical constitution quantitatively and qualitatively. The Raman bands are proportionate to the molecular bond concentrations, and their sharpness can be easier to analyze than the broader bands from an IR

transmission. Because Raman can analyze the type of bond based on how heavy it is, and therefore how significant the oscillations are, it can provide valuable insight that IR cannot. Ultimately, these two techniques are best used complementarily to reveal a sample's molecular signature.¹³

Fourier Transform IR Spectroscopy

As was seen with Raman Spectroscopy, Fourier Transform Infrared Spectroscopy (FTIR) is also a quantitative as well as qualitative characterization method that relies on the varying extent that chemical bonds in matter absorb infrared radiation. When samples are exposed to infrared radiation, molecular bonds react in predictable and documented patterns of emitted energy. This energy is recorded and analyzed in FTIR spectrometers; these work by emitting infrared radiation from a source, which is split into two beams with a device called an interferometer, where the beams each hit their respective mirror: one stationary and one mobile.

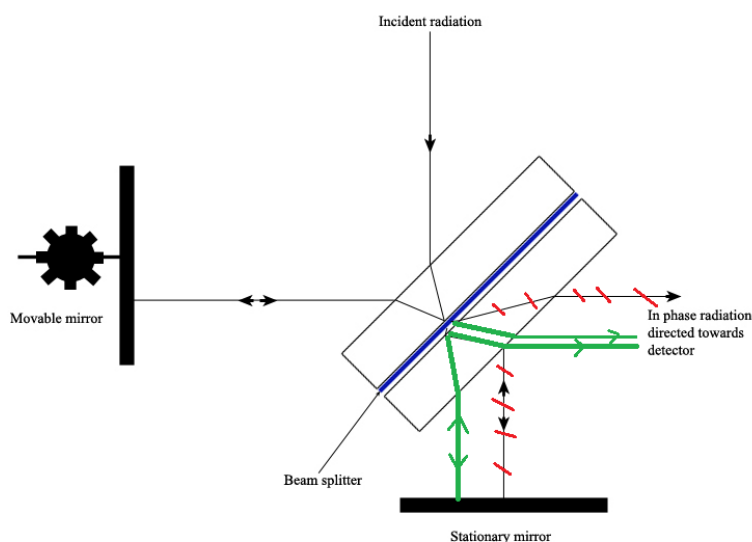


Figure 1.6. Schematic of an interferometer.¹⁴

When the beams of light interact upon returning to the mirror, they create constructive and destructive interferences at different wavelengths as the mobile mirror moves in a highly controlled fashion during the analysis.¹⁵ These different frequencies of the recombined circularly polarized

light allow samples to be irradiated by light separately at different individual wavelengths. As the sample absorbs the infrared radiation and the bonds of the molecules become excited, the atoms vibrate, and the FTIR spectrum depicts this excitation in the form of spectral absorption. With the adjustable beams of light, several different wavelengths can be applied to the sample over a period of time, and the detector is able to incorporate all frequencies of the analysis and computes the complete IR spectrum of the sample using the Fournier transform algorithm, Equation 1.1.¹⁴

$$f(\nu) = \int_{-\infty}^{\infty} f(t)e^{+i2\pi\nu t} dt \quad [1.1]$$

With the utilization of the different frequencies, one can obtain the interferogram with the detector. Equation 1.1 gives the relation between the frequencies sent by the radiation source and time of the tests.¹⁴

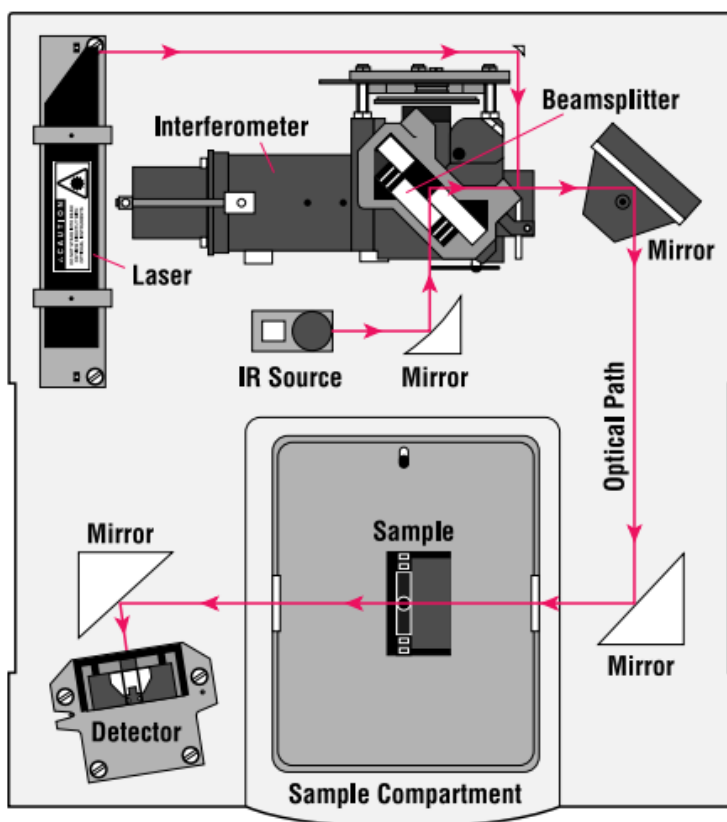


Figure 1.7. Schematic of a spectrometer arrangement.¹⁶

Energy-dispersive X-ray Spectroscopy

Energy-dispersive X-ray spectroscopy (EDX) is a technique used to identify particular elements and their proportions in a sample. First, a scanning electron microscope (SEM) is used to generate an image. From here, an X-ray spectrum of the image will be generated to give the characteristic and continuum X-ray results – the characteristic X-rays will show up as energy peaks over the background continuum X-rays and will depict the various elements in the sample. These elements will be distributed based on their atomic number, with the Y-axis showing counts and the X-axis giving the energy levels at each of the corresponding counts.¹⁷

To produce a characteristic peak, first, a high-energy incident electron is fired at the sample. This will eject an electron from an inner shell, and the void will be replaced with an electron from an outer shell. The “superfluous energy” emitted as the outer shell electron moves to the inner shell will be captured as an X-ray characteristic of the atom, and the X-rays of different energy levels will form characteristic peaks at distinct energy levels in the spectrum.¹⁷

EDX can also be used to gain information about a specific part of the sample by keeping the electron beam at one spot rather than scanning the entire sample. This is useful for finding the density of an element at a certain part of the sample and can be used repeatedly to create a map of the elements as they lie in the sample. An example of such a map is shown below: ¹⁷

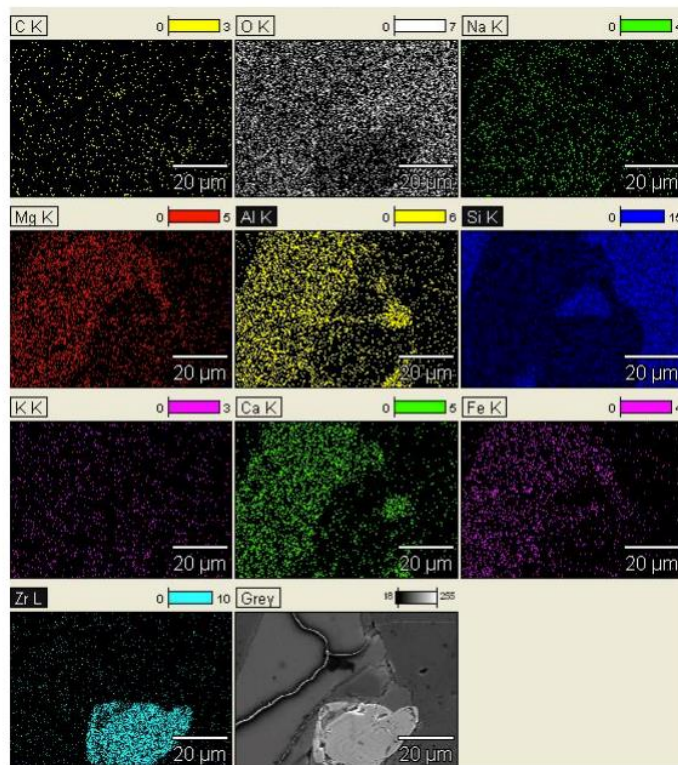


Figure 1.8. Elemental Mapping via EDX.¹⁷

As you can see, the multiple scans of the same sample show how the various elements are distributed throughout unevenly.¹⁷

In order to determine the element from the characteristic radiation line, Moseley's Law needs to be employed. Moseley's law states that:

$$E = C_1 (Z - C_2)^2 \quad [1.2]$$

In the equation, E serves as the energy of the emission line for a given X-ray series, Z is the atomic number, and C₁ and C₂ are constants. With increasing atomic number, the X-rays for each series increase. K, the inner shell, is the series with the highest excitation potential, and the further out a shell is, the lower its overall potential. This trend is vital to analyze the elements in the sample.¹⁷

EDX has a limit of detection of around 1000-3000 ppm, and the background continuum needs to be accurately assessed. This can be done through either an estimation process where the

background is subtracted wherever it does not fit the peaks, or it can be accounted for by a fitting model using an algorithm to define the continuum as an analytical function. In order to get the Peak to Background Ratio, the following equation must be used.¹⁷

$$P/B = 1/Z [(E_0 - E_C) / E_C]^{n-1} \quad [1.3]$$

In this equation, E_C is the critical ionization energy, E_0 is the accelerating voltage, Z is the atomic number, and n represents a constant based on a particular element and shell.¹⁷⁻¹⁸

The X-ray detector itself is comprised of a collimator assembly, an electron trap, a transparent window to allow X-rays in while preserving a vacuum inside the detector, a crystal typically made of “silicon, into which is drifted lithium”, a Field Effect Transistor (FET), and a cryostat. An image of an X-ray detector is shown below.¹⁷

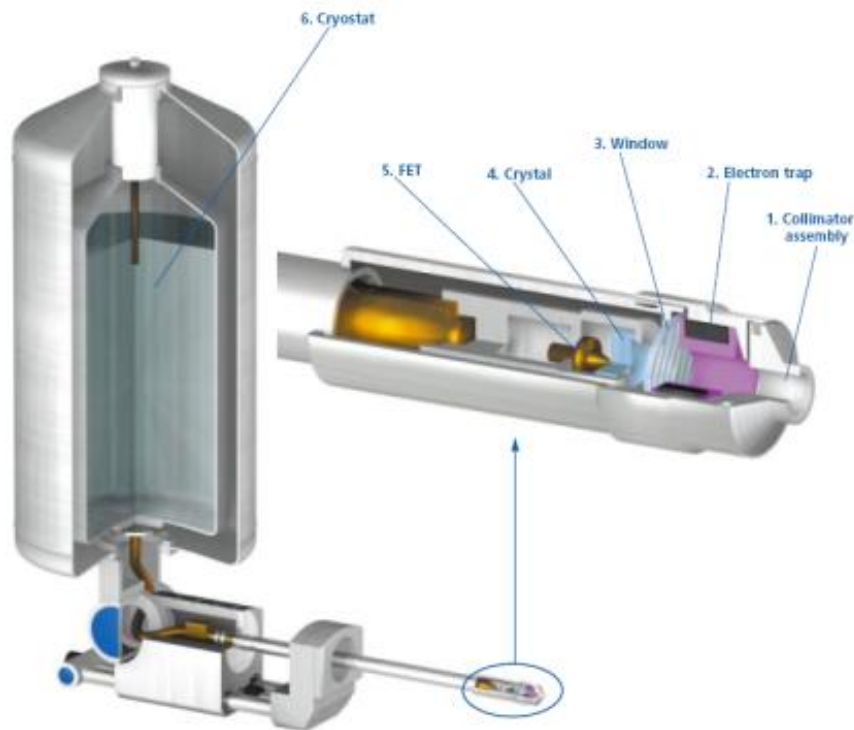


Figure 1.9. X-Ray Detector Schematic.¹⁷

The collimator assembly is the first object the X-rays come into contact with. It ensures that the detector only picks up X-rays from the appropriate excited area. Next, the electron trap, a pair of magnets, deflects any electrons that might cause unwanted “background artifacts.” After the X-rays pass through the window, they strike the Si (Li) crystal, creating energy. This energy is absorbed by the crystal through “a series of ionizations” that create electron-hole pairs, after which the electrons move into the conduction band of the semiconductor.

The hole acts as a free positive charge within a crystal lattice, and then a voltage is applied to both ends of the crystal to produce a charge signal. This signal intensity is “directly proportional to the energy of the incident X-ray.” Once the signal is received, it undergoes amplification. The FET does this by measuring the charges of the X-rays and outputting it as voltage. The FET and crystal need to be cooled periodically so that the signals can be separated from the electronic background noise inherent to the detector – this is done using a cryostat with liquid nitrogen.¹⁷

CHAPTER 2

GRAPHENE: FROM SYNTHESIS TO APPLICATIONS

Introduction

Diverse and overwhelming attention from nearly all corners of science has been devoted to graphene due to its remarkable electrical, thermal, optical, and mechanical properties, to name a few. This chapter investigates many paths to the synthesis of graphene, as well as the many potential applications that result from a material with such extraordinary characteristics. Synthesis techniques include the synthesis of graphene oxide and the reduction of graphene oxide by thermal, chemical, electrochemical, and photonic means, as well as the synthesis of graphene from graphite exfoliation, epitaxial growth on silicon carbide, chemical vapor deposition, and also the transforming of graphene into graphane. The potential applications of graphene include, but are by no means limited to, photo catalysis, electronics, fuel cells, composites, membranes, water filtration and purification, and medicine. This review serves as an overview of many of the synthesis techniques and myriad applications of graphene, introducing many of the key concepts that pertain to these two areas.

Graphene has been one of the most widely studied nanomaterials since its isolation in 2004 by Andre Geim and Konstantin Novoselov at the University of Manchester.¹⁹ Prior to the isolation of graphene, carbon nanotubes were at the top of the research totem and remain one of the most studied nanomaterials. By the two structures having virtually identical properties beside conformation, the science community was already well versed in the highly thermally and

electrically conductive, nearly transparent (transmits approximately 98% of incident electromagnetic radiation also known as light in the visible spectrum), and mechanically robust properties of the phenom nanomaterial, graphene.

There are so many amazing properties that go along with this profound material, but one of the major impedances to its properties and widespread implementation is the difficulty in the synthesis of graphene in pure form. Many attempts have been made to synthesize high-quality graphene of substantial size, but these attempts have all fallen short of perfect formation and shortchange the material by drastically compromising its properties.

Synthesizing graphene oxide (GO), by the modified Hummers' method, is a highly used technique to create the oxidized form of graphene that can then be reduced by several methods to reduced graphene oxide (rGO). This form of graphene has inherently poor quality due to the harsh oxidation treatment, and flakes are typically synthesized on the few-hundred nanometer to several micrometer scale.²⁰ Certain techniques for the exfoliation of graphite can produce higher-quality graphene, but this process is extremely slow and the small flake limitation still exists.

Chemical vapor deposition (CVD) has received increased interest due to its ability to make small domains of high-quality graphene, but due to random deposition of carbon atoms, discontinuous grain boundaries form, making the bulk film properties mediocre. Further, graphene synthesized by CVD typically forms multi-layer graphene unless formed on copper, which helps to limit the graphene to a single layer at very low pressure.²¹ There have been attempts to scale up CVD processes using copper foils that run roll to roll, but these attempts have not been very successful in generating high-quality graphene.²²

Graphene Synthesis

Exfoliation via Intercalation Compounds

One method to synthesize graphene consists of intercalating graphite with tetrabutylammonium hydroxide (TBA).²³ For this, they exfoliate commercial expandable graphite (160-50 N, Grafguard) which is intercalated with sulfuric acid and nitric acid, which exfoliates violently upon heating due to the released gaseous species from the intercalant during a 60 second heating to 1000 °C in forming gas (mixture of hydrogen and nitrogen gas) to yield few-layer graphene. Then, the exfoliated graphite was ground and intercalated with oleum (fuming sulfuric acid with 20% free SO₃) and inserted TBA in the oleum intercalated graphite in N,N-dimethylformamide (DMF). They then sonicated the oleum intercalated, TBA inserted graphite in a DMF solution of 1,2-distearoyl-sn-glycero-3-phosphoethanolamine-N-[methoxy(polyethyleneglycol)-5000] for 60 minutes, forming a homogeneous suspension. After centrifuging to remove large material from the supernatant, 90 % single-layer graphene, which is easily transferred to water and organic solvents.²³

Synthesis of Graphene Oxide

The Hummers' method can be used to prepare graphitic oxide in which oxidation of graphite occurs by mixing graphite in H₂SO₄ and slowly adding KMnO₄ and NaNO₃ while keeping the temperature below 20 °C; then, a large amount of distilled water and hydrogen peroxide are added, followed by filtering the graphitic oxide and washing it with HCl to remove remaining ions.²⁴ The modified Hummers' method utilizes a pre-conditioning step in which the graphite is initially heated at 80 °C in concentrated H₂SO₄ with P₂O₅, and K₂S₂O₈ before being subjected to the Hummers' method.²⁰ Without this pretreatment, only oxidation at the periphery occurs, leaving a graphite core. Thus, the modified Hummers' method is widely employed to make graphene oxide

to ensure the formations of single-layer GO. Also, single-layer graphene oxide can be attained by the Hummers' method followed by the use of ultrasound to cleave the few-layer graphitic oxide into graphene oxide.²⁵ An alternative route claimed to be a more environmentally friendly version of the "Hummers Method", uses a 9:1 mixture of H₂SO₄:H₃PO₄ that is combined with graphite flakes and KMnO₄, heated and stirred for 12 hours, poured over ice and H₂O₂, and then worked up by being sifted through a sieve.²⁶

Graphene oxide contains oxygen functionalization including epoxide, hydroxide, and carboxyl groups, which can then be reduced or removed to make reduced graphene oxide (rGO). This reduction process often removes the majority of the oxygen groups but does not typically remove them all.

Reduction of Graphene Oxide

Thermal Reduction

One method to reduce graphene oxide is to heat it to high temperatures to break the carbon-oxygen bonds to remove these functionalities. A comparison of thermally reducing graphene oxide heated at 600 °C and at 1200 °C in a furnace shows that the latter demonstrates approximately double the current increase per applied voltage, signifying the oxide was more fully reduced at the higher temperature due to the higher conductance.²⁷

Graphene oxide can also be reduced thermally by microwave irradiation in N,N-dimethylacetamide and water, where the reduced graphene oxide can be achieved in a matter of minutes at lower temperatures using an 800 W microwave source.²⁸ Microwaves excite the molecules, allowing the carbon-oxygen bonds to break at lower temperatures

Chemical Reduction

Chemical reduction is a widely used method of making reduced graphene oxide. By reducing exfoliated graphene oxide with hydrazine hydrate ($\text{N}_2\text{H}_4 \cdot \text{H}_2\text{O}$), it is claimed that rGO is formed with a graphitic form that is comparable to pristine graphite.²⁹ In another study, it was found that when the ratio of hydrazine to GO in solution is 7:10, it provides an optimal ratio for the generation of stable dispersions of very conductive graphene sheets.³⁰ This is believed to be a scalable process that does not require surfactants or polymeric stabilizers.

Sulfur compounds, such as NaHSO_3 , SOCl_2 , SO_2 , $\text{Na}_2\text{S}_2\text{O}_3$, and Na_2S , have also been found to be a good reductant of GO, and the first two are comparable to hydrazine hydrate in the reduction of GO yet do not release vapors as toxic as hydrazine.³¹ This makes for a less hazardous and environmentally friendly synthesis technique.

Electrochemical Reduction

When reducing graphene by electrochemical means, an electrode serves as the reductant to supply electrons to the oxidized form of a chemical species to obtain the reduced form. Electrophoretic deposition (EPD), a form of electrochemical reduction, produces high-quality reduced graphene oxide at low cost and rapid speed with the easy ability to tailor the shape.³² Electrophoresis is the movement of particles in solution due to an applied electric field. This field attracts the graphene oxide to the cathode, where it is reduced. High-quality electrochemically reduced graphene can also be produced by depositing graphene oxide on an electrode, inserting it into a phosphate buffer solution, and cycling the voltage between 0V and -1.5V multiple times (100 times).³³

For various electrophoretically (electrophoresis is the migration of ions in solution) deposited graphitic composites such as graphene- MoS_2 ³⁴ and MWCNT- MnO_2 ³⁵, the controlled

co deposition of the materials is crucial for the best capacitive performance. This co deposition requires a very homogeneous dispersion of these components to make uniform composite structures.

Reduced graphene oxide (rGO) and Ni(OH)_2 structures with high specific capacitance can be electrochemically synthesized from a graphene oxide (GO) and $\text{Ni(NO}_3)_2$ suspension.³⁶ This produces 5-10 nm Ni(OH)_2 nanoclusters that are anchored on RGO. They have a high specific capacitance of $1404 \text{ F}\cdot\text{g}^{-1}$ at $2 \text{ A}\cdot\text{g}^{-1}$, high stability in electrochemical cycling, and high charge-discharge rate capability.

Electrophoretic deposition has also been used to generate Au nanoparticles decorated on graphene film for a counter electrode for a CdS quantum dot-sensitized solar cell.³⁷ It was found that this structure showed higher activity in the solar cells than with traditional Pt or Au counter electrodes, which they believe is due to the high electro catalytic activity of the gold nanoparticles and the conductivity of the reduced graphene network.

It has also been shown that electrophoretically deposited graphene has a lower turn on voltage and threshold voltage for electric field emission than a graphene powder coating due to the uniform thickness and many perpendicular edges to the bulk film.³⁸

Laser or Photo-Reduction

Using a laser to photo-reduce graphene oxide has proven a simple and economical method to create high-quality graphene with the ability to incorporate patterns of graphene separated by graphene oxide to tailor electronics.³⁹ This work by Kaner's group at UCLA uses a Light Scribe DVD burner laser to etch supercapacitor patterns by reducing graphene oxide into conductive, charge storing reduced graphene oxide.

Extreme UV photolithography using 46.9 nm light can reduce patterns in GO with sub-micrometer resolution.⁴⁰ These patterns can go down to a width of 250 nm with a sacrifice in edge resolution. Achieving the controlled patterning of graphene on the nanometer scale is a key requirement for mass-production of graphene nano-devices.

Graphene can also be synthesized from graphene oxide by using UV-irradiation on TiO₂ nanoparticle suspensions in solution.⁴¹ This mild UV treatment helps to increase the conductivity of the reduced graphene oxide, and the TiO₂ nanoparticles prevent the collapse of RGO upon reduction. In another study without semiconducting nanoparticles, it is believed that UV light photo ionizes the solvent, which allows solvated electrons to reduce the suspended GO.⁴²

Graphene from Silicon Carbide

At elevated temperatures, the epitaxial growth of graphene occurs at the surface of silicon carbide. One group found that the growth of epitaxial graphene occurs at 1275 °C at a pressure of 10⁻¹⁰ mbar.⁴³ The temperatures and pressures required for growth vary, but a high temperature and low pressure in this vicinity are required without further experimental modification.

Certain techniques can reduce the temperature required for the epitaxial growth of graphene from SiC. It has been demonstrated that graphene can be synthesized on the surface of silicon carbide micro- and nano-particles by heating SiC to 800 °C under Cl₂ gas, which serves to etch SiC(s) into SiCl₄(g) and C(s), with the carbon in the form of wrapped graphene (WG) that can be exposed by an electrochemical erosion technique (ECE).⁴⁴ Also, millimeter sized graphene films were synthesized at 750 °C by applying a nickel coating on a silicon carbide surface, where the graphene was said to have been continuous over the Ni.⁴⁴

Chemical Vapor Deposition

Chemical vapor deposition (CVD) has been shown to generate graphene on surfaces from carbonaceous, gaseous precursors by strict regulation of temperature and pressure. This process is one of the few processes to make large sheets of graphene, although many discontinuities exist in the film.

It has been demonstrated that graphene growth on Cu substrates is not a precipitate process but rather a catalytic process and is self-limiting at low pressure²¹ (i.e. mostly just a single layer will form and remain regardless of carbon gas exposure time). It has been demonstrated that on a copper surface, graphene can be grown in under three minutes in a vacuum from CH₄ and H₂ at temperatures over 1000 °C.⁴⁵ Graphene can also be grown on arbitrary surfaces, but at higher temperatures due to the lack of catalytic effect from copper.

When graphene is grown between two adjacent pieces of copper foil, higher uniformity is achieved due to the smooth surface provided by a high vapor pressure of copper atoms between the faces that continually redeposit and fill rough spots that would generally accrue on the foil.⁴⁶ These rough spots generally lead to discontinuities in the graphene film. It was believed and demonstrated that films of Cu (<111> facets) have more ability than foils of Cu (<110> facets) to hold hydrogen when annealed with the gas; this serves to generate more uniform carbon deposition into graphene sheets.⁴⁷ Hot filament thermal CVD has also been shown to generate large area, monolayer films on Cu.⁴⁸ A copper-nickel alloy film allows carbon to dissolve into the nickel and upon cooling, formation of multiple layered graphene surface precipitate can be formed of controlled thickness.⁴⁹

A common transfer mechanism includes using a polymer such as PMMA to transfer graphene to another support from copper, but this leaves polymeric residue that p-dopes the

graphene; this can be somewhat counteracted by a treatment with a solvent that is amine-based that n-dopes the graphene.⁵⁰ Transferred graphene made by CVD has been shown to demonstrate electrical qualities similar to exfoliated graphene on a substrate of SiO₂ after using IPA instead of water as the transfer medium and a 300°C anneal under ultra-high vacuum.⁴⁵ These are examples of the importance of the transfer mechanism when transferring graphene from the deposition substrate to a support substrate.

Roll to Roll Chemical Vapor Deposition

Graphene can be grown on copper foils that run from roll to roll through CVD chambers. High optical and electrical characteristics were attained from plasma-assisted CVD of graphene during a 5-10 mm·s⁻¹ roll to roll process.^{22a} Hot filament thermal CVD (HFTCVD) has also shown promise for the high-throughput synthesis of single-layer graphene.⁴⁸ This group also believes that this method can be used to incorporate other atoms such as H, N and B into the graphene lattice for doping. Another group has synthesized a 23 cm wide, 100 m long roll of relatively high-quality graphene (minus many discontinuities where an oxide layer formed on the copper and cracks where the copper foil deformed) by a CVD roll to roll process^{22b} shown in Figure 2.1:

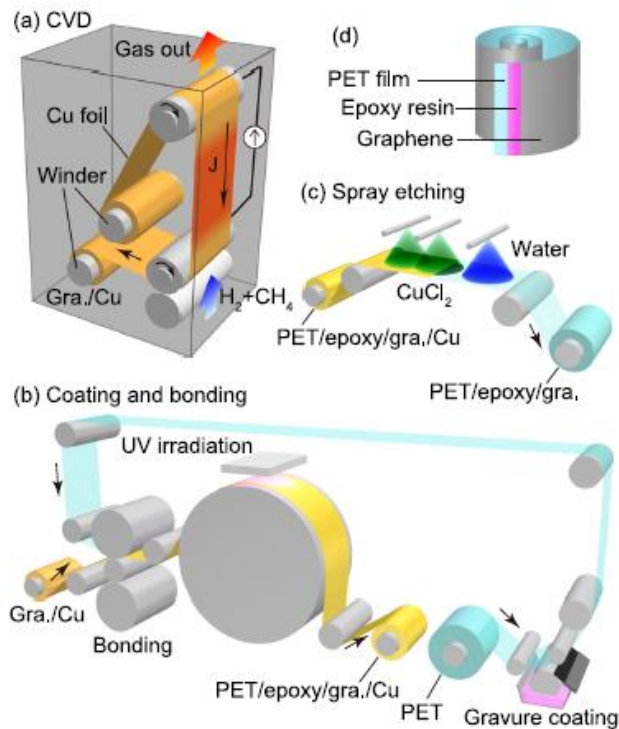


Figure 2.1. a) Roll-to-roll continuous CVD with resistance heating of a Cu foil to approximately 1000 °C for the growth of graphene. b) Epoxy coated and cured to bind PET to Cu/graphene. c) Cu removal by CuCl_2 spray etching. d) graphene/epoxy/PET.^{22b}

They are able to make large rolls of graphene this way, but the mentioned discontinuities are substantial and greatly degrade the properties of the graphene. The roll to roll CVD method seems to be the closest technique to the mass production of large sheets of graphene, but it has a long way to go in regards to making these sheets of high quality.

Graphane to Graphane

Graphane is the fully hydrogenated form of graphene that serves as an insulator. The partially hydrogenated form of graphene is called graphane and is semiconducting. Varying degrees of hydrogenation can tailor the band gap in graphane.

An acidic solution (H_2SO_4) has been shown to serve as a typical source of protons for the hydrogenation of graphene into graphane (or graphane) by merely attaching graphene to an

electrode in solution and applying a suitably negative potential.⁵¹ Graphane-like structures have also been synthesized by plasma-assisted CVD at 600°C from 5% CH₄ in H₂.⁵² Also, it has been calculated that the band gap decreases as the width of graphane nanoribbons increases.⁵³ These calculations have shown that the thin-ribbon structures have a wide band gap of around 3.83 eV, which is promising for electronics applications.

Exfoliation of Graphite

The exfoliation of graphite is a method to cleave few-layer or individual layers of graphene. There are many different solution methods for exfoliating graphite that can use organic solvents, water-surfactant systems, ionic liquids, etc., that help to dissociate graphite into single or few-layer graphene.⁵⁴

Three exfoliation techniques were studied by Xia et al., where they found: electrochemical oxidation to be a fast exfoliation technique that disrupts large quantities of graphite yet makes defective graphene, chemical oxidation is effective but detrimental to the graphene structure as well, and sonication in organic solvents gives the best quality graphene but is a very slow technique, only acting on the few layers at the surface.⁵⁵ This serves to demonstrate that there is a tradeoff in exfoliation techniques between speed of production and quality of the exfoliated graphene.

Applications of Graphene

There are many potential applications of graphene that have been proposed. Graphene has applications in photo catalysis, where it often serves as a conductive support or transparent conducting layer (TCL). Being a TCL, graphene has the ability to replace transparent conducting oxides, like indium tin oxide, which currently serves as an expensive TCL in many touchscreens,

LCDs, organic LEDs, solar cells, etc. If graphene can be mass-produced at low cost, it will inherently make these devices much more economical to produce.

Another major application under investigation is the use of graphene in thin, flexible electronics. Indium tin oxide, being rare and expensive as mentioned, is also brittle and does not afford the flexibility in electronics as would graphene.⁵⁶ Graphene is so strong and flexible that this would allow electronics to be folded (with no hinges) or rolled up for storage.

There are also applications of graphene in fuel cell catalyst structures, where graphene serves as a conductive, corrosion resistant support for catalyst moieties. Graphene is one of the few materials that can hold up in the harsh acidic environment due to protons migrating to the cathode in hydrogen fuel cells.

Also, by graphene having such incredible properties, it allows for some interesting composite materials. By incorporating graphene's mechanical strength, electrical and thermal conductivity, and transparency, composites can achieve properties previously unattained. This could provide composites that serve multiple purposes, like dissipate heat or conduct electricity on top of being incredibly strong.

Sterile and contaminant-free water is paramount to civilization, so another important application of graphene is for water filtration and purification. Graphene can be used to filter out salt, bacteria, or other detrimental components from contaminated water sources. This would require much less energy than used by desalinization plants or reverse osmosis for purifying water. Graphene filters could easily be implemented in third world countries or for people on the go like the military or for outdoor adventures.

Graphene also has widespread applications in medicine. One of these is drug delivery, where antibodies or other drug molecules can be attached to graphene to enter directly into certain

parts of the body. Graphene can also be used for biomedical imaging, due to its ability to absorb and emit certain parts of the electromagnetic spectrum. Graphene can also be used for photothermal therapy and for the reattachment of neurons.

There are also some more far-reaching applications such as graphene used in a space elevator to hoist payloads to space and smart space suits. The space elevator could drastically reduce the amount of energy (and money) consumed to send rockets to space. Also, the smart space suits would better inform astronauts of their bodily conditions to inform them of potential health hazards that may occur.

These are just some of the potential applications people foresee, and there are undoubtedly many more on the horizon. Graphene has so many promising characteristics that could revolutionize the world if flaws in its synthesis and application could be mastered.

Photo catalysis: Semiconducting Nanomaterials

Graphene enhances the effects of semiconducting nanomaterials, and for this discussion, one of the most common semiconducting materials, Titania or TiO_2 will be the main focus. TiO_2 nanoparticles on graphene oxide have shown enhanced catalytic activity relative to the particles alone due to the high surface area for adsorption and due to graphene being a good electron conductor.⁵⁷

The hydrothermal combination of graphene with TiO_2 nanoparticles and nanowires shows significantly higher photo catalytic properties than the nanoparticles and nanowires alone due to more separation of electron-hole pairs and high conductance for transport.⁵⁸ Similar results were demonstrated with Rhoda mine B photodegradation using TiO_2 and graphene nanocomposites.⁵⁹

The effects of improving interfacial contact between graphene and TiO_2 has been studied by optimizing the ratio of the two components.⁶⁰ It has been further demonstrated that forming a

shell of reduced graphene oxide around TiO₂ nanoparticles increases the contact area between the two, inhibiting more electron-hole recombination, and providing higher photo catalytic and photoelectro-chemical efficiencies than TiO₂ nanoparticles simply deposited on reduced graphene oxide flakes.⁶¹ Sheets of alternating TiO₂ and graphene also serve to prevent charge recombination, leading to efficient photocurrent conversion.⁶²

It is believed that too high of a concentration of graphene in TiO₂-graphene composites is inhibitive of photo catalysis, affording less light the ability to absorb into the TiO₂ nanoparticles.⁶³ Adding graphene to TiO₂ nanoparticles has proved to enhance the catalytic effect in both alcohol conversion to aldehydes⁶⁰ and for hydrogen evolution.⁶⁴

It has also been demonstrated that graphene-TiO₂-Fe₃O₄ composites have enhanced durability and are recollectible, which gives promise to their use in wastewater treatment.⁶⁵ The iron oxide in this material makes it possible to be harvested magnetically.

Silicon nanowires and nanoholes with a hole transport layer of poly(3-hexylthiophene) and an overlaying transparent graphene electrode have achieved solar conversion efficiencies of 9.94% and 10.34% respectively.⁶⁶ Graphene enhanced the efficiencies of these structures by being a transparent conducting layer to facilitate electron transport.

Only a few semiconductor material composites with graphene were mentioned herein, but an intimate contact of graphene and other semiconductors provide many of the same graphene-based benefits, namely the prevention of electron-hole recombination and charge transport.

Photovoltaics

Being transparent and conductive with the ability to incorporate dopants, graphene has useful applications in solar cells. Photocurrent was found to be most substantial at p-n junctions at voltages between the Dirac points of the positively and negatively-doped partitions of graphene.⁶⁷

Doped mosaic graphene platelets have shown to have relatively high carrier mobility at room temperature with intrinsic graphene mobility having $5000 \text{ cm}^2\text{V}^{-1}\text{s}^{-1}$ and nitrogen-doped graphene mobility of $2500 \text{ cm}^2\text{V}^{-1}\text{s}^{-1}$; and with a 632.8 nm, 900 μW laser focused to a 1 μm spot positioned at the neutral points between the p-n junction, it generates a 125 nA current.⁶⁸ Also, epitaxial graphene with titanium and palladium junctions on SiC shows increased photocurrent when the laser is moved near the graphene-metal interfaces.⁶⁹ This shows that doped graphene (opposed to the zero-band gap, pristine graphene) can generate a photocurrent if excited near the p-n junction.

It has been shown that graphene attached to dichalcogenides monolayers of MoS_2 , MoSe_2 , and WS_2 can achieve 5-10% absorption of incident light.⁷⁰ Graphene paint that features these light absorbing and electricity producing dichalcogenides provides a new avenue to produce solar paint for energy applications.⁷¹ This paint could then be applied to the exterior of buildings, portable electronics, camping gear, or any surface that will be exposed to the sun to harvest solar energy.

Dye-Sensitized Solar Cells

Graphene has also been shown to enhance the efficiencies in dye-sensitized solar cells. Gel-coated composites of reduced graphene oxide and single-walled carbon nanotubes greatly increase the conductivity in the counter electrode and have outperformed Pt, reduced graphene oxide, and SWCNTs alone.⁷² Nitrogen doped graphene (NDG) has also shown enhanced electro catalytic activity when serving as a counter electrode in DSSCs by having a low charge transfer resistance of $0.9 \Omega/\text{cm}^2$, which has been attributed to the nitrogen defects in the structure as well as the exposure of the edge plane.⁷³

A novel route to replacing platinum in the cathode of dye-sensitized solar cells (DSSC) has been achieved through a non-corrosive, cobalt mediator interacting with graphene nanoplatelets attached to silver nanowires.⁷⁴ This same method has proven to yield transparent conductive oxide

(TCO) and platinum-free counter electrodes for DSSC applications with 86% of the efficiency of their Pt-TCO counterpart reference material.⁷⁵ Pt-TCO efficiency when used for the counter electrode in DSSCs is surpassed by metal sulfide (here, NiS and CoS) particles loaded on the extremely high-area surface of graphene.⁷⁶

It has been found that using plasma-oxygenated multilayer graphene as a recombination barrier layer (RBL) in dye-sensitized solar cells can improve the efficiency by up to 19% with respect DSSCs that do not utilize an RBL⁷⁷. 3D graphene networks grown by CVD on foam nickel rods reduce inter-sheet resistance and allow facile carrier transport when supporting P25 nanoparticles, proving to be 32.7% more efficient than the standard P25 photo anode alone in DSSC applications⁷⁸ (P25 is a mixture of typically 70:30 or 80:20 anatase and rutile titania⁷⁹). Sulfur-doped nanoporous carbons have 2.2 times higher photocurrent generated by the degradation of methylene blue than did the commercial TiO₂ photo catalyst.⁸⁰

Water-Splitting

Graphene can also be used in conjunction with other materials to augment water dissociation. Fe₂O₃/graphene/BiV_{1-x}Mo_xO₄ heterojunctions yield a current of 1.97mA/cm², which is the monitored resulting current from oxygen evolution at the anode and hydrogen evolution at the cathode.⁸¹ The photocurrent of these structures is enhanced by the conductive layer of graphene between the different semiconductor layers that facilitates faster charge transfer, preventing the recombination of electron-hole pairs. Cu-graphene co catalysts immobilized on TiO₂ have proven to compare to Pt-TiO₂ photo catalyst systems for hydrogen evolution.⁸² This reduces the use of the rare and expensive transition metal, platinum.

Electronics

High Conductivity

Graphene has high electrical conductivity, achieving electron mobility of over 15,000 $\text{cm}^2 \cdot \text{V}^{-1} \cdot \text{s}^{-1}$, even in high concentrations of electrons and holes, leading to the ballistic transport of electrons.⁸³ Grain boundary discontinuities formed during the synthesis of graphene severely limit the conductivity of the material. It has been demonstrated that incorporating silver nanowires with graphene can greatly improve the conductivity and make the resistivity approximately that of the calculated value for ideal graphene by bridging the discontinuities.⁸⁴ Besides silver nanowires, other one-dimensional, conductive nanomaterials such as carbon nanotubes can also be used to join discontinuities in graphene. This high conductivity in graphene leads to less power-loss due to resistive heat generation, making for highly energy-efficient electronics.

Flexible Electronics

Being flexible, conducting, and transparent, graphene allows for the generation of flexible electronics. Graphene field-effect transistors generated by CVD have shown power-gain frequencies and current-gain frequencies of 3.7 GHz and 10.7 GHz, respectively, with 1.75% limits of strain.⁸⁵ This is the only device where, when strain levels are over 0.5 %, it achieves gigahertz-frequency power gain. This shows that graphene is a suitable material for flexible electronics with high frequency transistor switching. Graphene can also be utilized in many other electrical components to allow electronic devices the freedom to flex.

Field Effect Transistors

With the high electrical mobility in graphene, it allows for fast-switching transistors. It has been demonstrated that lasers can be used to induce a field-effect in graphene transistors without

using chemical doping, local gates, or plasmonic structures⁸⁶. Fluorinated graphene synthesized by exposing highly ordered pyrolytic graphite (HOPG) to fluorine gas for 36-48 hours at 600°C possesses a band gap of approximately 3.5eV.⁸⁷ Plasmonic resonance in graphene is highly affected by an external, perpendicular magnetic field when doping concentrations are low.⁸⁸ This allows transistors to be tuned by magnetism.

Lithium Ion Batteries

Due to graphene's extremely high surface area, extensive investigation has gone into its use as electrode materials in lithium ion batteries. It has been demonstrated that pyridinic nitrogen intercalation in the graphene structure from liquid precursors (hexane and acetonitrile) to CVD serves to make double the charge-discharge capacity of pure graphene.⁸⁹ It has also been shown that nitrogen-doped graphene nanosheets (N-GNSs) have proved better than graphene nanosheets (GNSs) in Lithium-Oxygen batteries due to the high efficiency toward the oxygen reduction reaction (ORR) from more nucleation sites resulting from the nitrogen doping functional groups and defects.⁹⁰ Graphene-PET current collectors show promise in Lithium-Sulfur batteries due to their low weight, low cost, low metal use, and chemical stability.⁹¹

Supercapacitors

Graphene's extremely high surface area of 2630 m²·g⁻¹ makes it an ideal candidate for supercapacitor applications, with aqueous and organic electrolytes achieving 135 and 99 F·g⁻¹, respectively.⁹² Nitrogen-doping serves to increase the quantum capacitance in single-layer graphene by increasing the charge carrier density.⁷¹ Fe₃O₄ reduced on the surface of rGO shows increased super capacitance to either material alone.⁹³

A unique hybrid structure of CVD-grown carbon nanotubes on graphene using a cobalt catalyst leads to an extremely high surface area, and the nanotubes serve to hold the graphene

sheets apart for improved ionic diffusion and facilitate the electrochemical double layer buildup that yields a specific capacitance of 385 Fg^{-1} at 10 mVs^{-1} in 6 M KOH .⁹⁴ The structure can be seen in Figure 2.2:

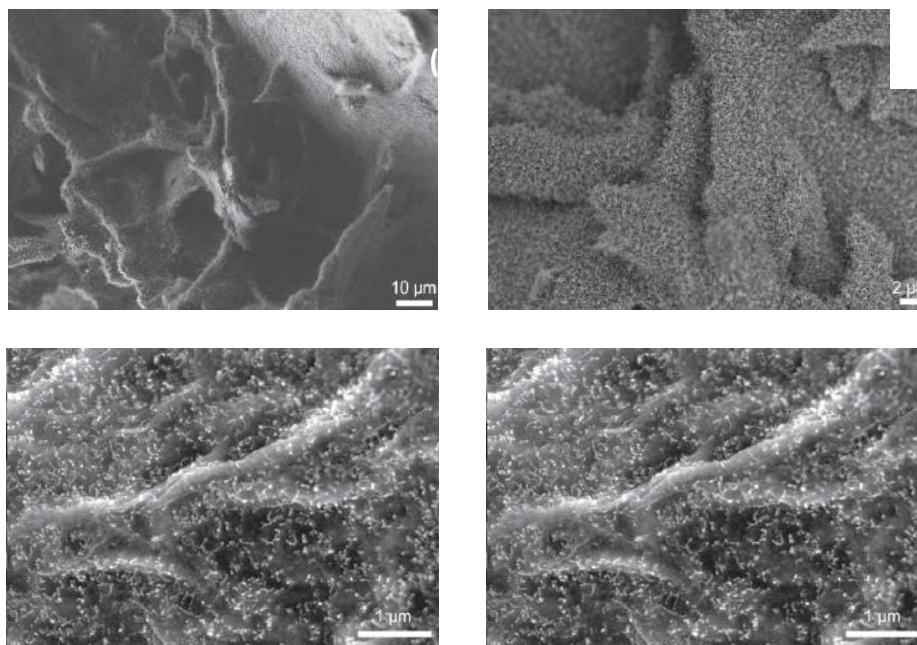


Figure 2.2: (a, b, c, d) SEM images of CNTs grown on graphene for high electrochemical capacitance.⁹⁴

The combination of reduced graphene oxide and cellulose generate high-surface area 3D structures due to the coagulation effect of glucose and also show promise for supercapacitor applications.⁹⁵

Light-Emitting Diodes

Graphene can also replace indium tin oxide as the TCL in LEDs such as being deposited via chemical vapor deposition on light-emitting nanorods of GaN.⁹⁶ This addition of CVD

graphene to fill the gaps between the nanorods showed a 32% enhancement over planar GaN-graphene diodes.

A patterned, transparent conducting layer of HNO₃-doped graphene coated with chromium and gold features the chromium layer penetrating the graphene and lowering the contact resistance to the p-GaN, and the graphene serves to spread the charge uniformly over the entire emitter surface⁹⁷ as shown in Figure 2.3:

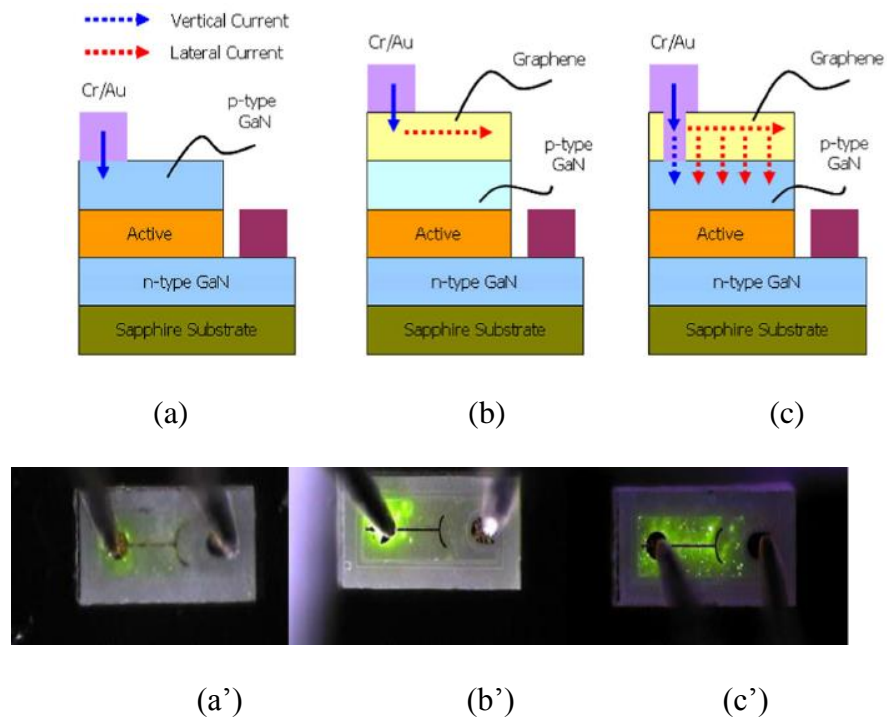


Figure 2.3: (a, a') LEDs without a TCL of graphene, (b, b') with a graphene TCL (non-doped) and (c, c') with a graphene TCL (doped).⁹⁷

For use in LEDs, the synthesis of zinc oxide quantum dots covered in a single-layer of graphene generates two extra bands of blue light due to the high curvature of graphene, developing a 250 meV band gap.⁹⁸ These structures were incorporated into multi-layer LEDs with other emissive structures to combine the different wavelengths emitted into white light.

Biosensors

Graphene is a good material for biosensors and other types of sensors due to its high surface area and conductance. A novel biosensor based on glucose oxidase (GOD)/Pt/functionalized graphene sheets/ chitosan has been developed that has a detection limit of $0.6 \mu\text{M}$ of glucose.⁹⁹ Similarly, another novel biosensor based on horseradish peroxidase (HRP)/Au/ graphene/chitosan has been designed to have a range of $5 \mu\text{M}$ to 5.13 mM and having a detection limit of $1.7 \mu\text{M}$ for H_2O_2 .¹⁰⁰ A very high sensitivity of approximately 2 ng/ml or 13 pM was achieved for detecting specific proteins using a field-effect transistor-based sensors utilizing vertically aligned graphene sheets that host gold nanoparticle-antibody conjugates¹⁰¹ as shown in Figure 2.4:

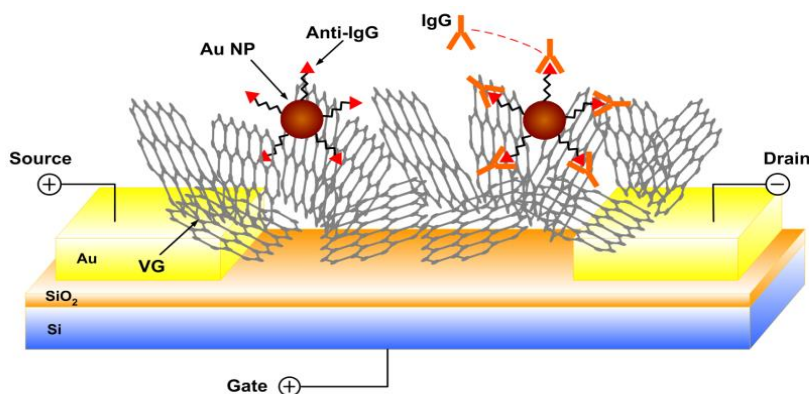


Figure 2.4: Graphene vertically grown between the drain and source of a field effect transistor. Protein-sensing antibodies are attached to graphene by gold nanoparticles.¹⁰¹

Proton Exchange Membrane Fuel Cells

Graphene has shown to be a good candidate for incorporation into fuel cell catalyst structures. Platinum nanowires grown on sulfur-doped graphene prove to have excellent catalytic activity toward hydrogen and methanol fuel cells¹⁰² and are shown in Figure 2.5:

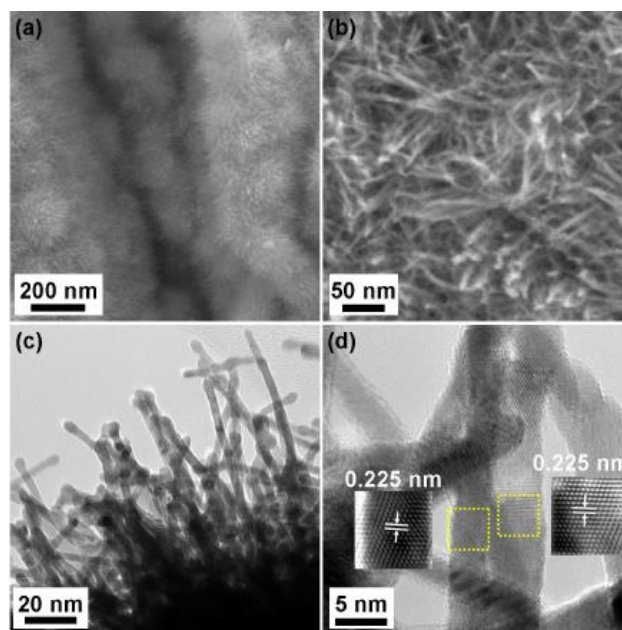


Figure 2.5: (a,b) SEM, (c) TEM, and (d) high resolution TEM imaging of 88% Pt nanowires on sulfur-doped graphene.

Another attempt to generate these same nanowires by the formic acid method reduced them on graphene oxide, making platinum nanowires on reduced graphene oxide.¹⁰³ For both of these structures featuring platinum nanowires, graphene serves as a highly durable support that holds the nanowires separate to prevent the overlap of their catalytically active surface area. The graphitic structure of graphene is highly acid-resistant, a key characteristic in the harsh, acidic environment at the cathode in a hydrogen fuel cell. There have also been several attempts to make non-noble metal catalysts with graphene, but none of these have shown as high of catalytic activity as platinum.¹⁰⁴

Composites

Polymer Composites

Graphene has many applications in its incorporation in polymer composites. When combining graphene with natural rubber into nanocomposites, it has been demonstrated that there are significant changes composite properties based on whether a solution-based method or ball-

milling method was used for processing.¹⁰⁵ By adding epoxy chains into graphene oxide and polymer composites, it serves to increase the mechanical strength by tailoring the polymer composite interfaces.¹⁰⁶ It has been demonstrated that the addition of thermally reduced graphene oxide (TRGO) into MWCNT/epoxy composites hinders the agglomeration of MWCNTs by trapping them between the sheets of TRGO.¹⁰⁷

Polyimide (PI) composites featuring graphene nanosheets functionalized by aminophenyl show a 610% increase in Young's modulus compared to PI alone.¹⁰⁸ Similarly, polyurethane (PU) nanocomposites show a 9 and 21 time increase in strength and tensile modulus when supplemented with 3 % wt reduced graphene.¹⁰⁹

Graphene/MWCNT aerogels filled with poly(dimethylsiloxane) (PDMS) achieves a conductivity of 2.8 S cm^{-1} using a mere 1.3 wt % graphene/MWCNTs, and this conductivity remains constant after stretching the material by 20% for 100 times and bending the material 5000 times.¹¹⁰ A simple dispersion method of dissolving graphene oxide in dimethyl phthalate serves to nearly fully reduce the oxide at 250°C and then allow the melt compounding with any thermoplastic polymer.¹¹¹

Structural Composites

Graphene can also be used to generate lightweight, incredibly strong, easy to assemble structures. If mass produced, graphene can either be directly used to cast structural components or be a reinforcing additive. One example are the proposed, 30 km tall carbon structures with a carbon nanotube and graphene mesh.¹¹² This structure features carbon nanotubes wrapped in a graphene sheet that are then assembled in a graphene ribbon wrap. These structures are claimed to be assembled from the base for “science and tourism.” The article claims the structures should be able to achieve a height of 30 km, although this extreme height would undoubtedly result in buckling

of the structure's legs upon loading. Also, it is doubtful whether the flexible carbon structures would bear a significant load in compression, even for a shorter structure.

Other Composites

Graphene, when combined with copper and nickel, serves to increase the tensile strength up to 1.5 GPa and 4 GPa, respectively.¹¹³ These strengths vary between 32-51% of the theoretical value based on the dislocation propagating across the graphene-metal interface. Adding graphene to copper makes the material stronger, and thus less copper can be used for electrical applications, as copper is often used in excess due to its low tensile strength.

Also, graphene can be rolled into graphic sports equipment such as golf clubs or tennis racquets like the HEAD Graphene.¹¹⁴ For this tennis racquet, the graphene flakes are rolled into the graphite. This technology features strong and light graphene midsection that allows the weight redistribution.

Membranes

Membranes are one of the most important structures in biology and in many other applications. Sheets of paper-like graphene oxide stacks can be generated by a simple directed flow assembly method that makes membranes that can be used for selective permeability, ionic conductors, supercapacitor materials, and molecular storage among other uses²⁵, as shown in Figure 2.6:

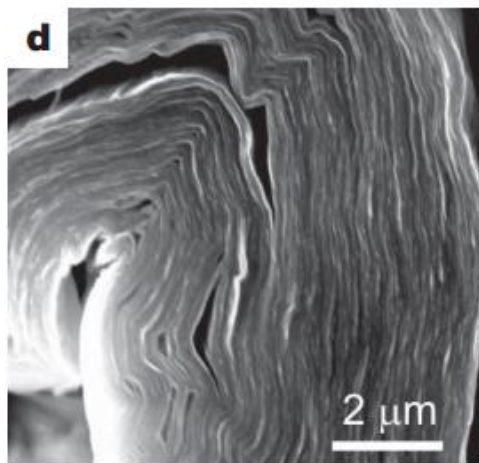


Figure 2.6: Profile view of a buckled strip of GO paper.²⁵

Water Filtration and Purification

Generating clean water is going to be one of the biggest challenges for the coming generations, and the use of graphene could be a low energy purification solution to meet this demand. The incorporation of nanoparticles, specifically TiO_2 , into stacks of graphene oxide sheets makes micro-channels that show promise for filtration applications.¹¹⁵ Another application of water filtration is in the use of a “graphene drinking straw,” which proposes a layer of graphene around a porous layer that surrounds a sponge that holds the moisture to be consumed with the straw shaft.¹¹⁶ This graphene layer around the drinking straw prevents salt and impurities from entering, providing potable water in third world countries, for military applications, camping, boating, etc.

Polydopamine-functionalized graphene serves as a reusable method for water purification in which contaminant molecules adsorb to graphene, and the contaminants can then be removed by varying the pH to remove heavy metals and by using alcohols to remove dyes and aromatic compounds.¹¹⁷ Reduced graphene oxide functionalized with poly(acrylamide) has also shown to adsorb and remove dyes and heavy metals from water systems, achieving 1000 and 1530 mg/g of lead and methylene blue, respectively.¹¹⁸ Spongy graphene can adsorb up to 86 times its own

weight of petroleum and fats and also toxic solvents and can be regenerated over ten times by heat treatment and releases over 99 percent per of the materials adsorbed each time.¹¹⁹

Medicine

Drug Delivery

The inert nature of graphene makes it ideal to enter into biological systems for drug delivery. Pegylated nano-graphene oxide are soluble in buffers and serum without flocculation and a basic physisorption of an antibody such as doxorubicin, a cancer cell killing drug, can be used for cancer treatment.¹²⁰ Chitosan-functionalized graphene oxide has improved solubility for GO in low-pH, aqueous solutions and show promise for the controlled release of Ibuprofen and 5-fluorouracil.¹²¹

Biomedical Imaging

Graphene oxide is photo luminescent in the visible and infrared regions and can be used to image cells in the near-infrared region of the electromagnetic spectrum.¹²⁰ Graphene quantum dots have shown to be superior to traditional quantum dots due to their high-level of inertness.¹²² These structures are single-layer disks of graphene that are typically 2-25 nm in diameter.

Photo-thermal Therapy

Nano graphene sheets show tumor passive targeting that is highly efficient and a low retention in reticuloendothelial systems, while the strong optical absorbance of near-infrared lasers makes very efficient tumor ablation.¹²³ This shows that graphene is good at targeting specific tissues in the body and its optical properties make it ideal for absorption of energy to destroy tumors in the body. Another targeting peptide of Arg-Gly-Asp allows selective uptake in U87MG cancer cells and efficient photo ablation of these cancerous cells.¹²⁴

Neuron Attachment

It is believed that graphene can be used to attach neurons to the brain to allow those with spinal cord injuries to regain bodily function.¹²⁵ This could open avenues for those with disabilities to regain the motion of limbs to return to a life of mobility.

Graphene in Space

Space Elevator

Creating a space elevator was first hypothesized for carbon nanotubes, as they were the only material strong and light-enough to attach earth to a mass in space that is held taught by centrifugal force. The same device is now proposed for graphene as shown in Figure 2.7:

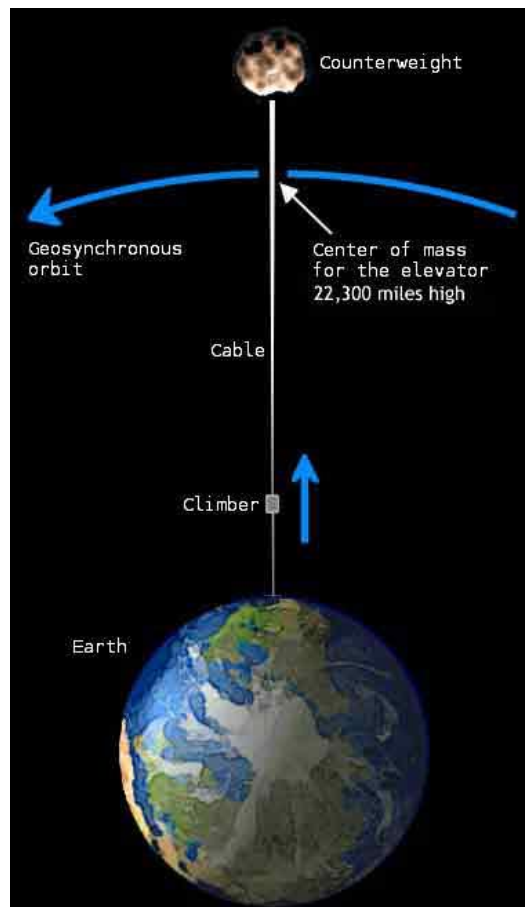


Figure 7: Schematic of the mechanism of a space elevator.¹²⁶

This could reduce the price of putting a kilogram into orbit from \$2500 to \$200, requiring much less energy to hoist the mass slowly with an elevator (possibly electrically through the graphene) than with a rocket.¹²⁶

Space Suits

Being ultrathin, transparent, and conductive, graphene is an ideal conductor to implement in smart clothing, including space suits. This would allow computers and electronics to be seamlessly integrated into clothing and could also make smart glass or mirrors with displays that could be used inside the astronauts' visors.¹²⁷ Graphene could also be used to reinforce space visors due to its strength and transparency.

Future Developments

There are many synthesis routes for graphene that have not yet been imagined or explored. In time, the current and future techniques for generating high-quality graphene will be further explored in attempts of innovation and improvement.

Much research is underway to implement smaller integrated circuits and components in electronics. With the ability for conducting graphene paths to be reduced from graphene oxide, it makes an opportunity for nanoscale circuits if lithographic techniques can be honed to reduce a smaller electrical path. Graphene is also being heavily explored for energy generation to be used in solar, fuel cell, and other applications.

Conclusions

There are many challenges to overcome in the synthesis and application of graphene. For graphene to be a household name, kinks in mass production must be ironed-out. Even if a material has the most amazing properties in the world (and graphene pretty much does), it will never serve

much use unless it can be synthesized in high quality in high yield. Thus, synthesis is a major obstacle to humanity fully benefiting from graphene.

One solution that could help make quality graphene could be to make “edge grown graphene” by combining electrochemical methods with CVD. This would require the carbon precursor gas being heated to sub-deposition temperatures and allowing the electricity to do the rest. It would be ideal to apply a suitably negative potential to just the graphene to allow carbon ions to reduce right on the edge of the graphene. However, unless graphene is on copper, it forms multiple layers. By the graphene being on a conductor, this makes it difficult to apply the potential to just the graphene and not the copper as well (with the current going through the copper, there would likely be random deposition of carbon, preventing purely edge growth).

Another method would be to apply a suitably negative potential to a very narrow strip of the copper foil during the roll to roll CVD process. Two adjacent, linear conductive probes could be designed similar to atomic force microscopy (AFM) tips that would slide along the bottom of the foil. The electric current could supply the electrons for the reduction of graphene by the electrons flowing between the immediately adjacent electrodes. This could help make the graphene grow from a line source for uniform growth.

Yet another CVD possibility would be to have two electric fields facing each other to force ions toward the center of a duct that leads to a narrow line on the foil. A suitable duct length would need to be determined to allow the fields to cancel the parallel motion and align the gas to flow perpendicular to the foil. It would be interesting if this method could make nearly a single-file path of carbon ions approach the surface. The point of this is to have the graphene grow uniformly in one direction to avoid grain boundaries.

For applications, the most immediate one that seems feasible is the incorporation of reduced graphene oxide in composite materials. They are already being used in some sporting goods, but their use could be one of the first applications to go mainstream in anything from airplane and car frames to tennis shoes and rain jackets. Graphene has shown some promise in transparent conducting layers and as a high-surface area electrode material, but discontinuities in the carbon lattice, and thus compromised performance, make its use questionable. Use in medicine is also likely a long ways off due to strict regulations, requiring the testing of graphene's biocompatibility.

It seems we have only seen the beginning of the applications of graphene due to it not being a common material that is readily available. Once sheets of pristine graphene are available to the public at low-cost, there is no way to predict the multitude of uses that will be dreamed and achieved. By graphene only being available on a small, laboratory scale, less minds ponder the material's uses, and thus less applications can be invented. Graphene shows promise for small-scale research applications, but again, inadequate synthesis techniques make its use not feasible outside of the lab in most applications. In the end, only time will tell if we as humans can master the art of the synthesis and application of graphene. If this daunting feat can be accomplished, we as a people will make a quantum leap in technological advancement, bringing the full benefits of graphene to fruition.

CHAPTER 3
ADVANCED NANOMATERIALS FOR ENERGY STORAGE AND CONVERSION IN
LITHIUM ION BATTERY (LIB) CATHODES AND LITHIUM IRON PHOSPHATE
SYNTHESIS AND CHARACTERIZATION

Introduction

As the world population continues to grow, pollution is becoming an increasing concern. Pollution contributes to global warming, changing the thermal equilibrium of our planet. The EPA has demonstrated a 274.5 Tg increase in CO₂ from 1990 to 2012 (5.4%), and fossil fuel combustion has been the primary cause of a 40% increase in global atmospheric CO₂ emissions since the industrial revolution. Further, the US alone accounted for approximately 17% of the global 32,579 Tg of CO₂ emissions in 2011, and the breakdown of greenhouse gases is shown in Figure 3.1.¹²⁸

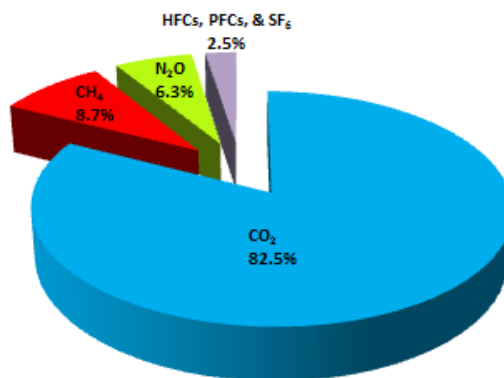


Figure 3.1. Greenhouse Gas Emissions Based on Tg CO₂ Equivalent (2012).¹²⁸

This pollution-based climate change has led government and private sectors to look for alternative energy solutions to reduce carbon emissions and provide sustainable energy. Some of these efforts have come from grid-based power such as stationary fuel cells, solar cells, wind turbines, hydropower, geothermal energy, biomass, etc. Another great concern is the reduction of pollution in the transportation sector. As of 2012, the EPA states that the transportation sector generates nearly equivalent amounts of greenhouse gasses as electrical generation, producing 28% and 32% of the total emissions, respectively¹²⁹. One method to counteract these emissions is the use of rechargeable batteries in lieu of oil in transportation.

With technological advances in electronic devices, power consumption has become an ever increasing demand. Further, with portable electronics seeing these similar advancements in operating power and function, portable energy storage from high-energy density batteries continues to be an increasingly popular topic of interest. Having higher energy-density than supercapacitors and other energy storage devices, society looks to portable batteries to meet the majority of their portable electronic needs. These batteries consist of electrochemical cells that are arranged in series and parallel to increase voltage and current, respectively.

Batteries are used in many consumer electronics. Two of the most popular of these are cellular phones and portable personal computers. In a global economy fueled by an increasing dependence on portable communication at the individual level, batteries require longer-lasting lives, while being lighter through higher energy density. Also, as microchips become increasingly smaller, computing power continues to increase, demanding more power from these devices and drastically shortening their lives. Power tools also demand large amounts of energy delivered at high power rates.. There is also much interest in batteries due to many fully electric and electric hybrid cars on the market. Tesla is in the process of building the “Gigafactory” to supply their own

demand for batteries in their electric vehicles. These and many more applications of batteries affect many humans on a daily basis and are of great interest to consumers.

There has been an ongoing search for batteries with the highest energy and power density. Figure 2 shows the relationship between energy and power density for some of the most common charge storage devices. From this, it can be seen that for electric vehicles (EVs) and hybrid electric vehicles (HEVs), lithium ion batteries are the only presently available charge storage devices that meet their required energy density, but their power density must be raised significantly¹³⁰.

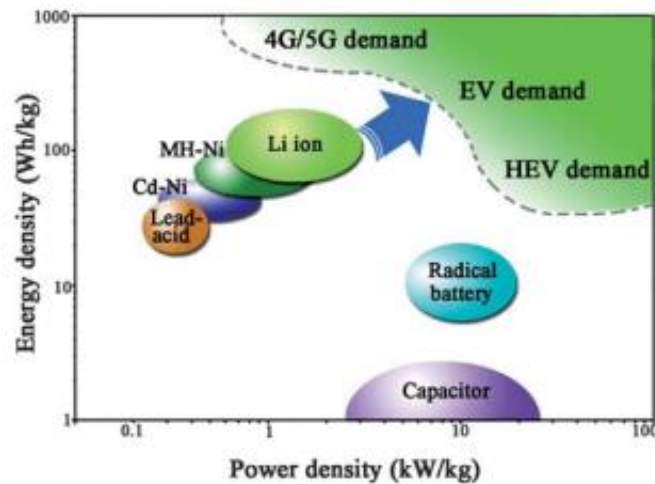


Figure 3.2. Energy density v. power density for some of the most common charge storage devices¹³⁰.

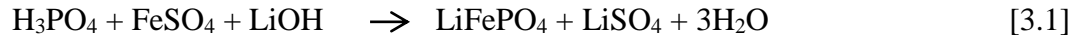
Lithium Iron Phosphate (LFP)

Since the discovery of the spinel compound lithium iron phosphate (LFP) as a lithium intercalation material by Padhi¹³¹ in 1997 at the University of Texas under John B. Goodenough, this material has been one of the most widely studied polyanionic compounds, and has been recognized to have great cycle ability with an open-circuit voltage of 3.45 V, reversible specific capacity of 170 mAh g⁻¹, low cost due to the enormous abundance of iron in earth's crust, environmentally benignity, and high degree of safety for operation in LIBs. Solid-state synthesis

is one of the most widely-used techniques to generate commercial LFP (solid precursors are mixed thoroughly and calcined at high temperature to form products via the supplied external energy), but at the energy intensive high processing temperatures (~600-900 °C), polydispersed grain growth occurs¹³². When heated to temperatures above 500 °C, Li_xFePO_4 starts to transform from olivine into mixtures containing other structures with different ratios of Li to Fe to PO_4 ¹³³.

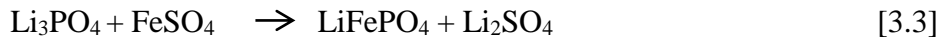
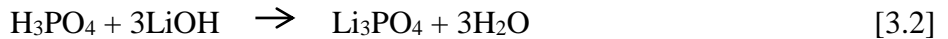
Hydrothermal Synthesis of LFP

The first hydrothermal synthesis of LFP was by Whittingham et al., according to the following scheme¹³⁴:



The resulting particles possessed a small amount of Fe^{3+} compounds and disordered Li/Fe, causing it to have low electrochemical capacity. They determined that these issues could be resolved through higher temperature synthesis (over 175 °C) or by a post-treatment calcination process under inert atmosphere at 700 °C¹³⁵. Hydrothermal synthesis has even been used to make LFP microstructure morphologies grown from the cyanobacteria biotemplate, *Spirulina*¹³⁶.

In another study¹³⁷, the mechanism was proposed to be:



Here, they propose that when the latter reaction is near completion, it is difficult to attain the full conversion of Li_3PO_4 to LiFePO_4 since the Li^+ ions are in far greater excess than Fe^{2+} ions. Upon adding an organic acid, pure phase LiFePO_4 is produced as the solution changes from pH 6.7 to pH 4.6. Further, the latter reaction conducts as a dissolution-precipitation mechanism, which is catalyzed by an acidic environment, where protons expedite the process of dissolution.¹³⁷

Organic acids also provide a chelating effect that may push the reaction toward the LiFePO₄ product. One example they provide is that citric acid may chelate the Fe²⁺ ion and form [C₆H₈O₇Fe²⁺], which can then combine with [Li⁺PO₄³⁻], making the ion pair complex, [C₆H₈O₇Fe²⁺ ... Li⁺PO₄³⁻] via coulombic attraction, to then crystallize through condensation to yield a single phase LiFePO₄. The organic acids play a two-fold purpose with the acidity affecting the reaction rate, and the chelation effect adjust the reaction balance to form pure product. To verify this theory, they ran a similar experiment without an organic acid, where they adjusted the pH to the same conditions (pH 4.5) using LiOH and H₃PO₄, and they found the product to not contain Li₃PO₄, but rather Fe₃(PO₄)₂, consistent with a previous report by Kanamura¹³⁸ et al. It was found that the incorporation of l-ascorbic acid completely converted Li₃PO₄ to LiFePO₄, where citric acid was slightly less effective, leaving 0.33 wt. % Li₃PO₄; the citric acid was not sufficient to make a complete conversion.¹³⁷

This is comparable to an earlier proposed mechanism¹³⁹, where a [PO³⁻Fe²⁺ ... F⁻ ... S⁺] complex is formed, and LiOOCCH₃ plays a vital role with the large radius of CH₃COO⁻ able to bring lithium into contact with this complex, yielding [Li⁺PO³⁻Fe²⁺ ... F⁻ ... S⁺], a precursor used to grow mesoporous Li₃Fe₂(PO₄)₃. Here, they propose the mechanism to be:

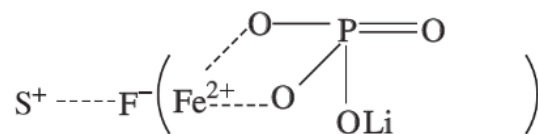
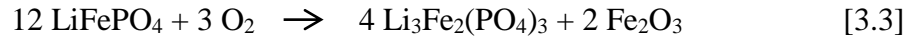


Figure 3.3. Mechanism proposed for templating by the structure-directing self-assembly process for lithium iron phosphate (S⁺ represents cetyltrimethylammonium chloride (CTMACI), the cationic surfactant).^{139a}

In a similar hydrothermal reaction by Sato et al.¹⁴⁰, it followed the scheme:



Here, since Fe^{2+} is easily oxidized in an aqueous environment, only a small amount of FePO_4 (35 mol %) was formed compared to LiFePO_4 (65 mol %). Next, the sample was calcined in air at high-temperature according to the reaction:



This yielded as sample that is about 60 wt. % $\text{Li}_3\text{Fe}_2(\text{PO}_4)_3$, 30 wt. % FePO_4 , and 10 wt. % Fe_2O_3 ¹⁴⁰.

As the pH increases in hydrothermal reactions, particle size decreases, but at pH of 10 and above, the impurities Li_3PO_4 and $\text{Fe}_2(\text{PO}_4)\text{OH}$ are formed¹⁴¹. At high pH, the solubility of Li_3PO_4 is low, causing it to precipitate out as an impurity¹⁴². Also, at low pH, $\text{Fe}_5\text{H}_2(\text{PO}_4)_4 \cdot 4\text{H}_2\text{O}$ is formed, and at high pH, $\text{Fe}_3(\text{PO}_4)_2$. The particle size also decreases with increasing concentration of starting reactants in the precursor solution¹⁴². Dokko et al. did studies of hydrothermal synthesis of LFP at different solution pH and Li^+ precursor concentration. For convention, they named the samples L1, L2, and L3, meaning a 1, 2, or 3:1:1 ratio of Li precursor to iron and phosphate and put a dash with a number after this term to designate pH. They found that at L1-7.4, pure phase LFP was formed, but large particles caused low conductivity and a specific capacity of only 20 mAh·g⁻¹. At L2, pure phase LFP was formed between $4.4 \leq \text{pH} \leq 7.2$, whereas at L3, pure phase LFP was formed between $3.4 \leq \text{pH} \leq 5.1$. Also, higher acidity made more rod-like structures, attributed to having a larger XRD signal for the (200) plane as was found for L2-3.5, whereas the less-acidic synthesis, L2-6.5 had a larger signal for the (020) plane, but at too high a pH, at L2-7.2, the XRD pattern is similar to commercial LFP, where no plane is of preference, and the particles are randomly shaped. They also noted that the crystal formation is governed by mass transfer, and under basic conditions, the kinetic factor is negligible and the crystals are unstable in the diffusion field and form random shapes.¹³⁸

Solvothermal and Hydrothermal Syntheses and Suppression of LFP Growth in the <010>

Solvothermal synthesis may be a more viable alternative to hydrothermal synthesis due to hydrothermal synthesis leading to the formation of FeOH in the precursor solution; this compound can produce Fe³⁺ contaminants in the final product, which cause metal ions in the electrodes to leach into the electrolyte as their reaction products.¹⁴³

Since lithium diffuses in the [010] direction in lithium iron phosphate, there has been much focus on limiting the growth in this direction to shorten the lithium diffusion channels as well as increase the surface area for diffusion. Certain solvents are known to chelate and cap certain crystal faces and serve as growth-direction agents. One such solvent is ethylene glycol (EG), which is known to form long chains through hydrogen bonding, serving to trap cations in the reaction mixture and assist LFP nucleation and growth. This chelating ability allows the EG to not only serve as a solvent, but also as a soft-template to grow LFP nanoplates and assemble them into elliptical microstructures.¹³²

Several of these approaches include hydrothermal techniques to preferentially grow LFP precursor salts into nanoplatelets. One method performs this technique in an inert atmosphere at 170 °C with ascorbic acid as a reductant to further prevent Fe(II) from oxidation. The concentration of starting materials has also been found to affect the particle growth. In this work, they monitored the growth effects on morphology, crystal configuration, and electrochemical performance varying the pH from 2.5 to 9.5. For this, they used FeSO₄·7H₂O for the iron source, LiOH·H₂O and Li₂SO₄ for the lithium sources, and (NH₄)₂HPO₄ and H₃PO₄ as the phosphate sources. The lithium and phosphate sources were dissolved in water, and then the aqueous iron source was added subsequently. FeSO₄ concentration was held at 1.0 mol dm⁻³, and the Li:Fe:P molar ratio was held to be x:1:1 with 1 ≤ x ≤ 3. They found that at an acidic precursor solution with pH of ~ 3.5, needle-

like particles were formed. In a weakly acidic solution with $4 < \text{pH} < 6.5$, plate-like crystals were formed, and at pH above 7.2, the crystals became randomly shaped. The plate-like crystals were found to have the highest specific capacity of $163 \text{ mAh}\cdot\text{g}^{-1}$.¹⁴⁴

Some approaches for directional growth use salts that are iron, phosphate, and lithium-based with ionic liquids¹⁴⁵ or ethylene glycol¹⁴⁶ as face capping agents for enhanced two-dimensional growth. The ethylene glycol capping agent often makes free-standing nanoplatelets. Another approach finds diethylene glycol (-1.5 eV {010} binding energy) to be a more effective capping agent to prevent growth in this direction over ethylene glycol (-1.0 eV {010} binding energy)¹⁴⁷. Here, it is believed that through diethylene glycol's (DEG) stronger affinity for the {010}, it suppresses growth in the $\langle 010 \rangle$ and also forms a hydrogen bonding network between DEG molecules that further aid in blocking this crystal face (similar to EG). This approach makes flowerlike arrangements of connected LFP nanoplatelets that are easily broken up into individual nanoplatelets, but some battery research leaves the plates or sheets attached in micro-flower form for electrochemical evaluation¹⁴⁸.

Prior to the previously mentioned synthesis, nearly the exact same synthesis was employed in ethanol instead of DEG by Popovic et al. Here, urchinlike mesocrystal assemblies of nanoplatelets were formed similar to the DEG method, using $\text{FeCl}_2\cdot 4\text{H}_2\text{O}$, H_3PO_4 , and LiOH in ethanol. It was found that by changing the Fe^{2+} precursor to acetylacetonate instead of chloride, the mesocrystals no longer formed ($\sim 200 \text{ nm}$ rod-like structures formed instead). To further understand the influence of Cl^- , the Li precursor was switched from LiOH to LiCl , keeping the acetylacetonate iron source, and again, urchinlike mesocrystals of nanosheets are obtained. This demonstrates that the Cl^- anion serves as a growth-directing agent, as previously reported in literature.¹⁴⁹ To this end, tetrahedrons and cubes of single-crystal silver experience blunting of

corners and edges through a silver-dissolution process via twinned seeds mediated by chloride ions. Further, this same mechanism is believed to be responsible for the growth of silver nanowires. It is believed in this work that chloride ions may play a similar role with iron in the LFP nanosheets, causing a dissolution and reattachment of iron followed by lithium and phosphate, allowing the sheets to be selectively etched into thinner nanosheets.

Experimental Synthesis of LFP Nanosheets

Different LiFePO_4 morphologies were synthesized using a low-temperature, one-step solvothermal reaction adapted from G. Yu et al.¹⁵⁰ The precursor solution was prepared under argon, with an initial Ar purge of diethylene glycol (20 mL; 99 % Alfa Aesar) for 15 minutes to remove oxygen. Then, stoichiometric amounts (3 mmol) of $\text{FeCl}_2 \cdot 4\text{H}_2\text{O}$ (98 % Alfa Aesar) and LiCl (98.5 % Fischer Scientific), as well as l-ascorbic acid (5 wt. % with respect to the iron precursor; 99 % Alfa Aesar) were dissolved in the DEG at 70 °C under vigorous mechanical stirring for a half hour until the solution became neon green with no signs of solids (additional 15 minutes of Ar purging after adding the salts and organic acid-the solution turns dark yellow upon the oxidation of Fe^{2+} to Fe^{3+}). During this time, (3 mmol) LiH_2PO_4 (99 % CHEM –IMPEX INT’L INC.) was dissolved in deionized water (0.75 mL) by mechanical mixing and then purged by Ar for 5 minutes. This LiH_2PO_4 solution is then slowly injected into the first precursor solution via syringe and needle. Upon the addition of phosphate, the solution turns from neon green to light blue (darker blue at elevated pH). The solution undergoes vigorous mechanical stirring for 30 minutes before being quickly transferred to a glass insert in a Teflon® vessel that is capped and sealed inside a stainless steel autoclave (Parr instrument Company, 45 mL capacity) and placed in a 200 °C muffle furnace and left to react under autogeneous pressure for 24 hours. LFP particles precipitated to the bottom of the glass insert during the solvothermal process, and the reactor

cooled to room temperature in a water bath. The supernatant was removed and discarded, and the precipitate was washed with water and isopropanol until the solution was colorless. The LFP was finally suspended in isopropanol and dried in an oven at 60 °C overnight. To generate several different morphologies of LFP, the same procedure was repeated with the addition of aqueous 10M KOH (88 % J.T. Baker) to adjust the pH from the natural state ~1.7 pH to higher pH systems. KOH was chosen on account of the smaller, Na in NaOH being readily substituted for Li in LiFePO_4 ¹⁵¹.

Also, the Li content (total from LiCl and LiH_2PO_4) was varied by increasing the molar ratio of $\text{LiCl}:\text{FeCl}_2\cdot 4\text{H}_2\text{O}:\text{LiH}_2\text{PO}_4$ from 1:1:1 to 2:1:1. The effects of l-ascorbic acid content were studied at 0%, 2.5%, 5%, and 7.5% wt. in the standard system, as it was initially believed to play a significant role in the chelating effect.

Results

For convention, the structures will be referred to as Li2 (for the original system with one Li from LiCl and one from LiH_2PO_4) and Li3 upon doubling the amount of LiCl, followed by a dash and the pH (ie. the original system at 1.7 pH, with a 1:1:1 ratio of $\text{LiCl}:\text{FeCl}_2\cdot 4\text{H}_2\text{O}:\text{LiH}_2\text{PO}_4$, is named Li2-1.7). Figure 9 shows the SEM micrographs of the Li2-1.7 structures:

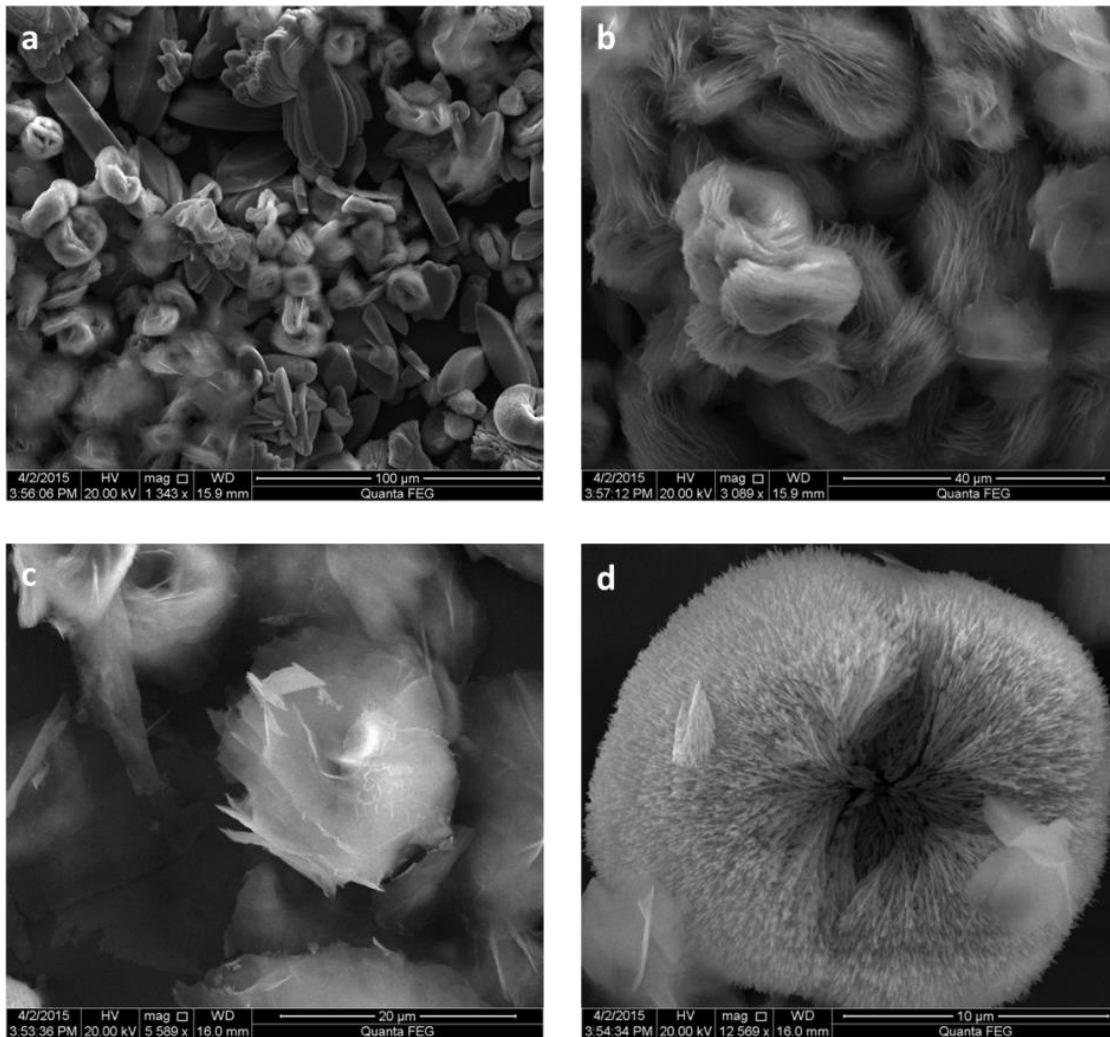


Figure 3.4. SEM images of the products of the Li₂-1.7 synthesis at different magnifications a) distribution of multiple particle types, b) tightly bound nanosheet “bird nest” microparticles c) loosely bound nanosheet “bird nest” microparticles, and d) a rod-like microparticles.

The structures synthesized by G. Yu et al. were more shaped like a fully extended/spaced “rolodex”, which were easily broken into individual nanosheets via mild ultrasonication in minutes. We attempted to break apart our Li₂-1.7 “bird nest” microparticles via ultrasonication, but it typically left a distribution of un-separated clusters, a few in-tact nanosheets, and many crumbled pieces of nanosheets as shown in Figure 4.5:

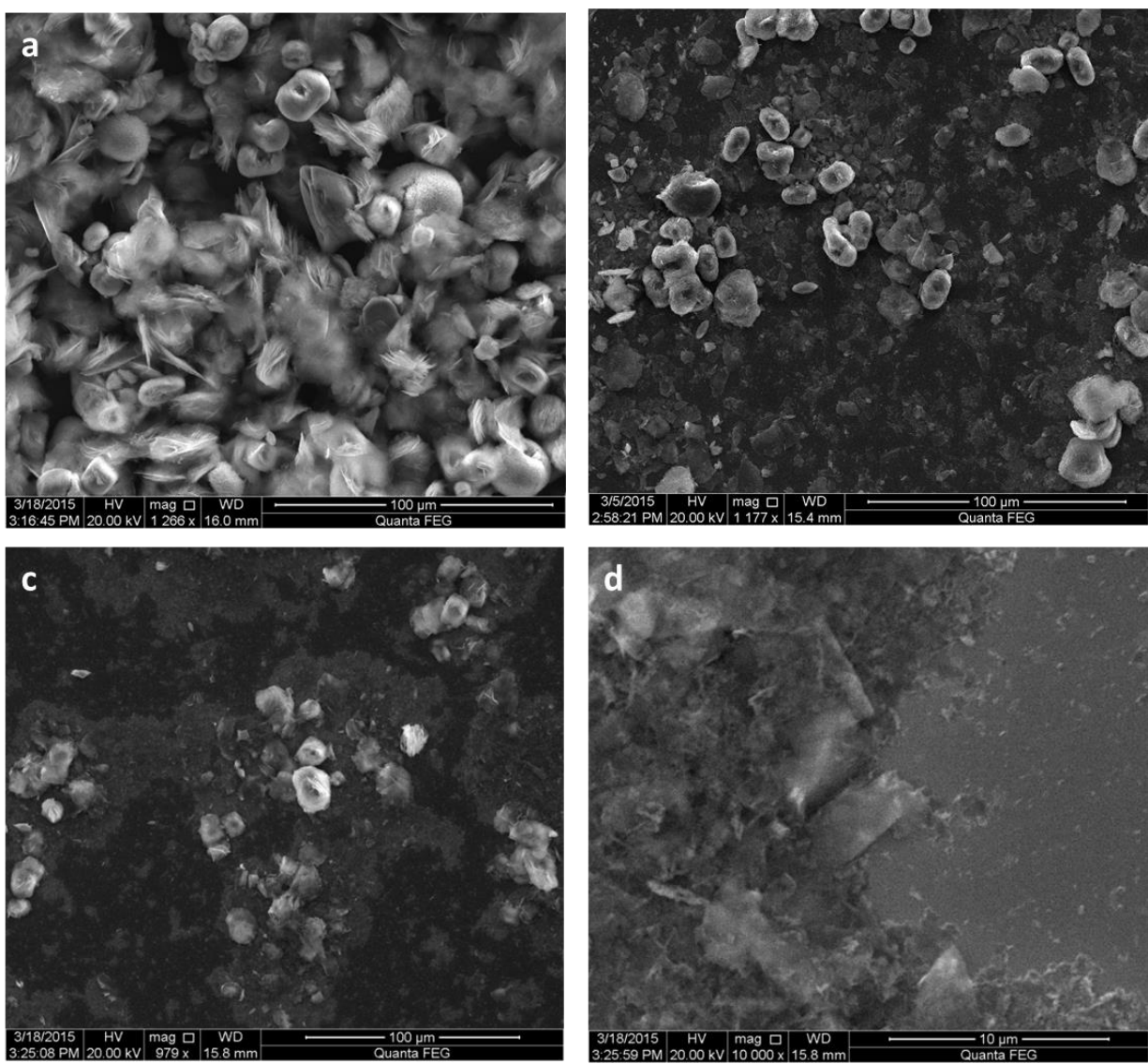


Figure 3.5. SEM images of Li₂-1.7 structures at different magnifications a) before sonication b) 25 minutes of bath sonication 200 W, c) and d) 30 minutes of probe sonication (30 % power, 200 W Sonic Ruptor).

Different times in both the bath and probe ultrasonicators proved to not break the nanosheets apart cleanly as demonstrated in the article procedure followed for this synthesis. Thus, we varied the ratios of LiCl:FeCl₂·4H₂O:LiH₂PO₄ from the molar ratio 1:1:1 to different ratios such as 1:1:1.1, 1.1:1:1.1, and 1.05:1:1.05 as suggested by the author to account for the hygroscopic nature of the LiCl and LiH₂PO₄ precursors, but none of these small LiH₂PO₄ and LiCl

variations appeared to have much of an effect on the morphology of the structures; we thus decided to vary the l-ascorbic acid content to see the effects on morphology in Figure 3.6:

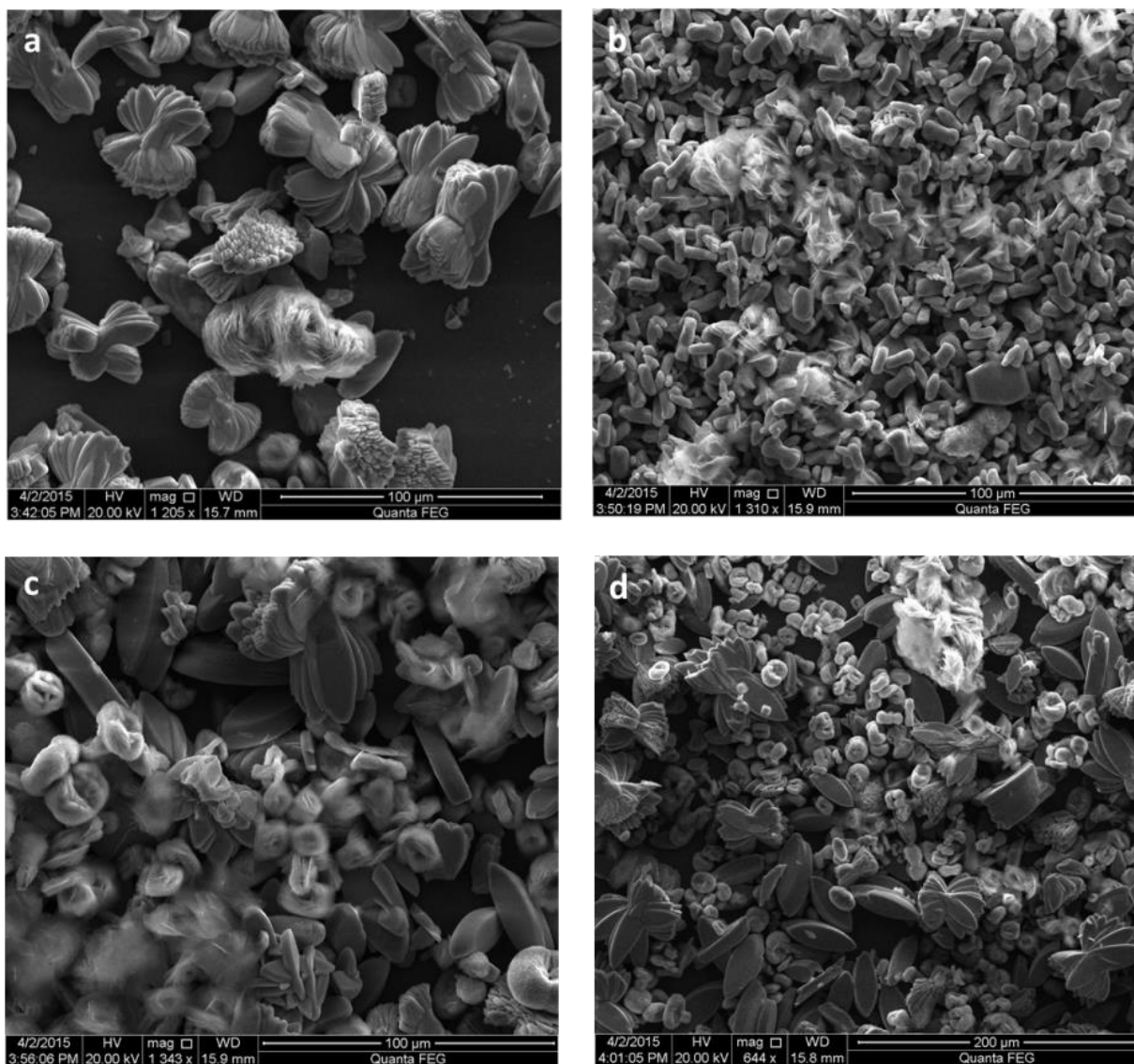


Figure 3.6. SEM images of synthesis with 1:1:1 $\text{FeCl}_2:\text{H}_2\text{PO}_4:\text{LiCl}$ with a) 0 wt. %, b) 2.5 wt. %, c) 5 wt. %, (Li2-1.7) and d) 7.5 wt. % (lower magnification) l-ascorbic acid with respect to the iron precursor.

At 0 wt. % l-ascorbic acid, nanosheet clusters did not form in much of a yield, and large, rotated micro-ovals formed. At 2.5 wt. %, very small clusters of loose nanosheets formed with impurity microparticles. And then at 5 wt. %, a higher yield of “bird nest” shaped nanosheet

clusters formed as were seen previously in the trials with 5 wt. % l-ascorbic acid when the molar ratios of LiH_2PO_4 and LiCl were standard or varied. And then at 7.5 wt. % l-ascorbic acid, “bird nest” structures as well as “double-headed cauliflower” shaped structures consisting of rod-shaped clusters. Figure 3.7 shows a more magnified image of the “double-headed cauliflower” shaped structure:

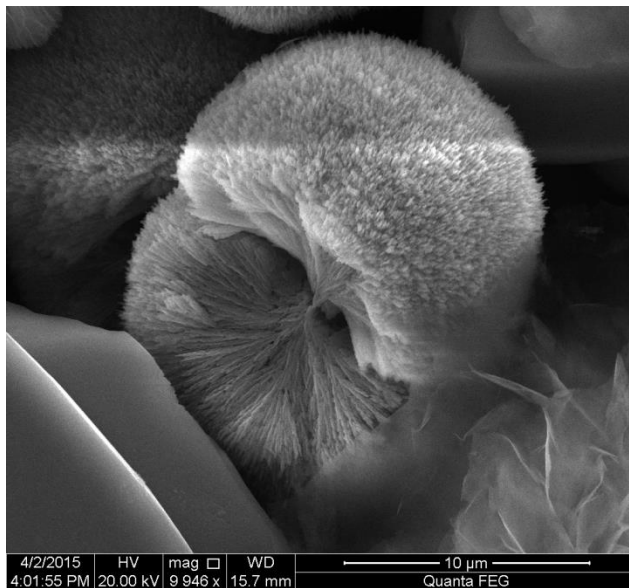


Figure 3.7. Close-up SEM image of the “double-headed cauliflower” shaped structure obtained using 7.5 wt. % l-ascorbic acid with all other conditions standard.

A few of these structures were observed in the 5 wt. % l-ascorbic acid sample, but the 7.5 wt. % l-ascorbic acid sample had a significantly larger proportion of these type structures. Due to only incremental pH changes, it seems that this must be a result of the chelating ability of l-ascorbic acid.

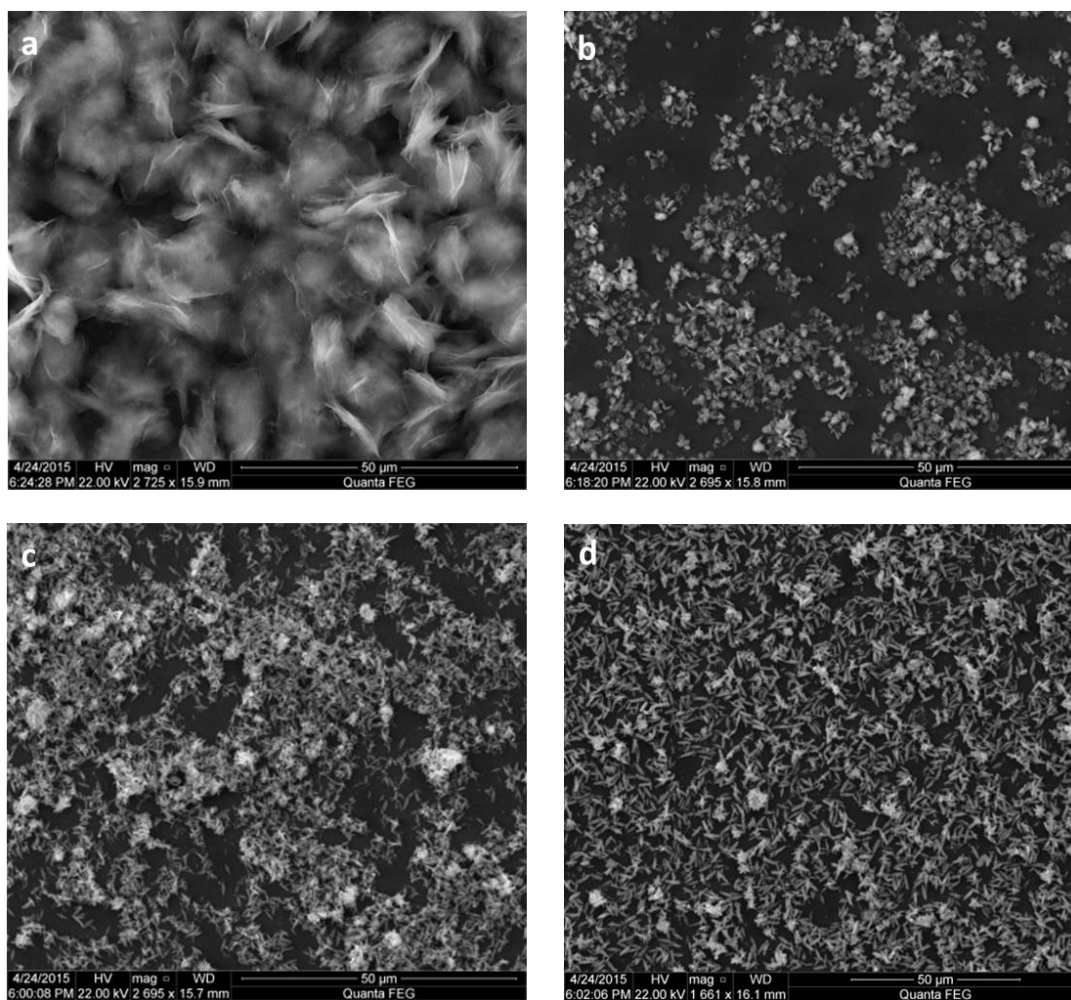


Figure 3.8. SEM images of synthesis with 1:1:1 $\text{FeCl}_2:\text{H}_2\text{PO}_4:\text{LiCl}$ with varied pH a) Li2-2.7 b) Li2-3.7, c) Li2-5.1, and d) Li2-5.9.

In these images, Li2-2.7 only features the white precipitate resulting from the synthesis (it had white, black (Figure 13), and a grey mixture, whereas the other three samples shown were fairly homogeneous products with high yield. The white phase of Li2-2.7 had fairly uniform individual nanosheets and small clusters of nanosheets that are approximately $15\ \mu\text{m}$ in the lateral dimension, Li2-3.7 formed small round platelets that are mostly on the order of $1\text{-}2\ \mu\text{m}$ in the lateral dimension, Li2-5.1 formed textured rod-shaped particles, and Li2-5.9 formed needle-like rods. Higher magnification images of the structures are shown in Figure 3.9.

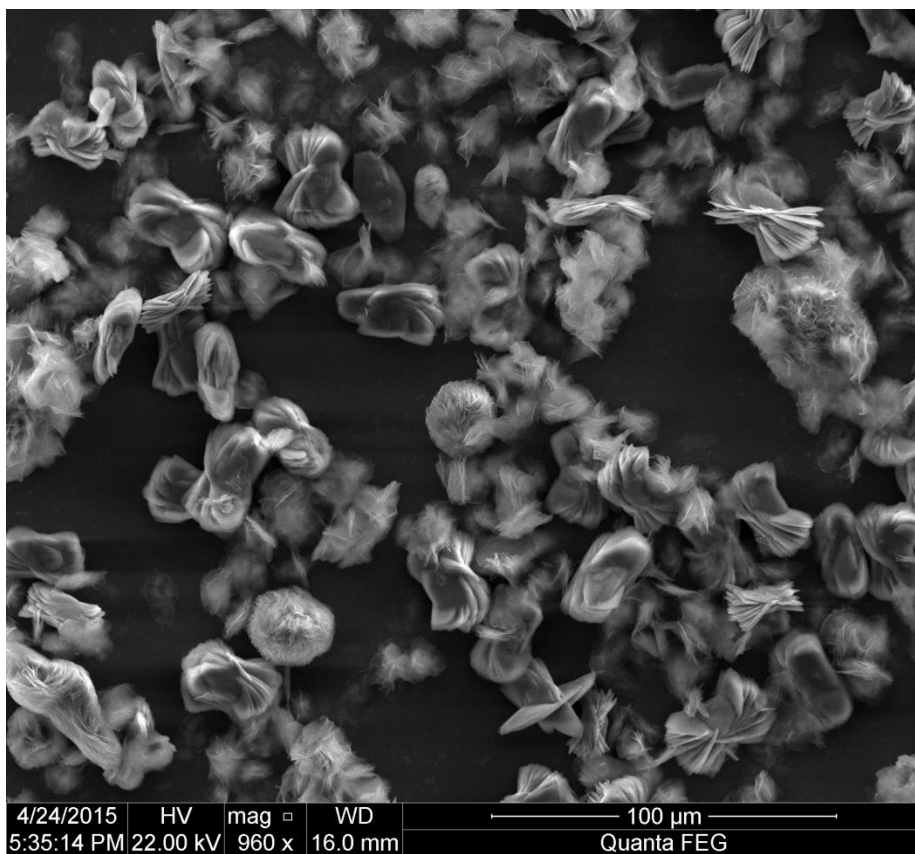


Figure 3.9. SEM images Li2-2.7 showing the distribution of the black precipitate.

This distribution features nanosheet cluster microspheres, loose or few nanosheet clusters, and the rotated oval shapes that were found previously in the Li2-1.7 sample.

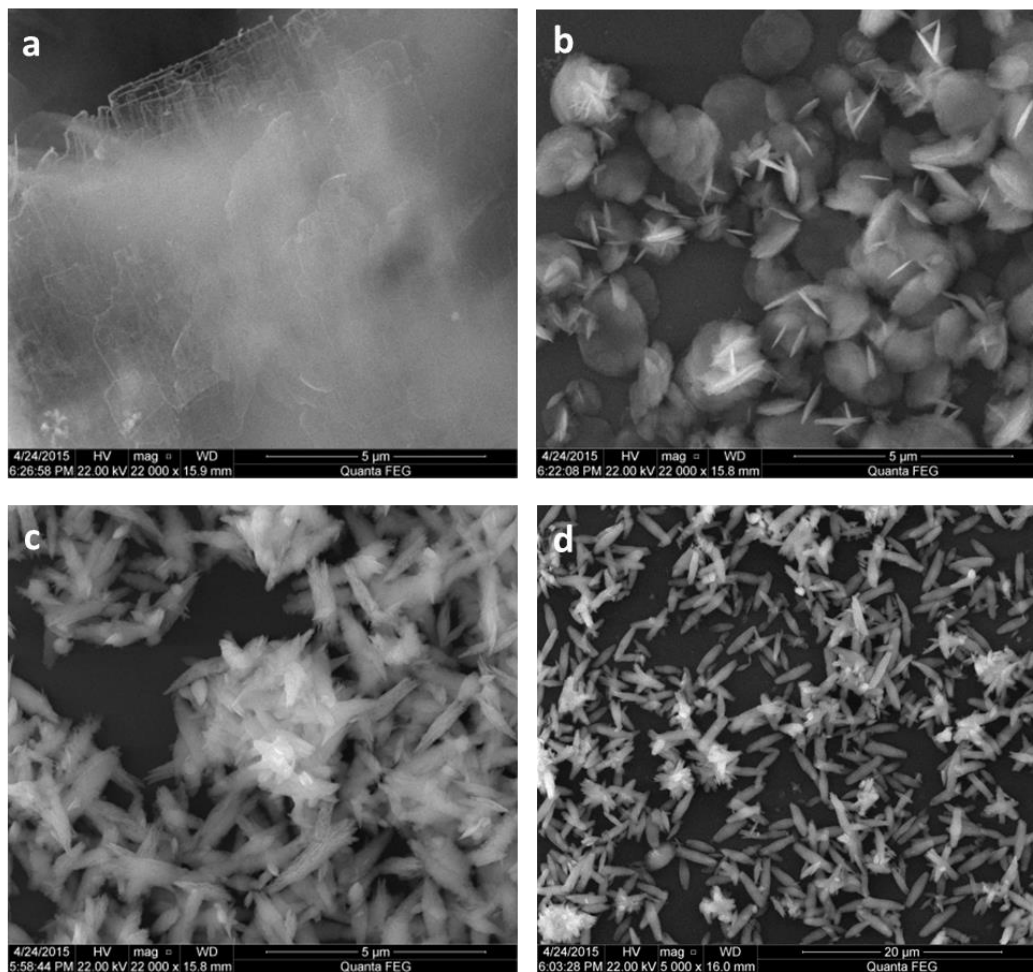


Figure 3.10. SEM images of pH-varied structures a) Li2-2.7, b) Li2-3.7, c) Li2-5.1, and d) Li2-5.9.

Terracing can be seen in the broad (15 μm) nanosheet in Figure 4.10a, demonstrating the edge effects of the growth of the material. Then, in Figure 4.10b (Li2-3.7), the material becomes much smaller in diameter ($\sim 1\text{-}3\ \mu\text{m}$). As the pH continues to increase to the Li2-5.1 and Li2-5.9 sample conditions, the $\{010\}$ facet becomes less dominant and the structures are formed in the shape of rods.

The TEM imaging for the Li2-2.7 structures is shown in Figure 4.11, and the Li2-3.7 structures are shown in Figure 3.11:

In order to observe the LFP nanosheets in higher magnification, gain insight into the sheet thickness and sheet-like nature, as well as observe the nanosheet edge characteristics, transmission electron microscopy (TEM) was employed in Figure 3.11:

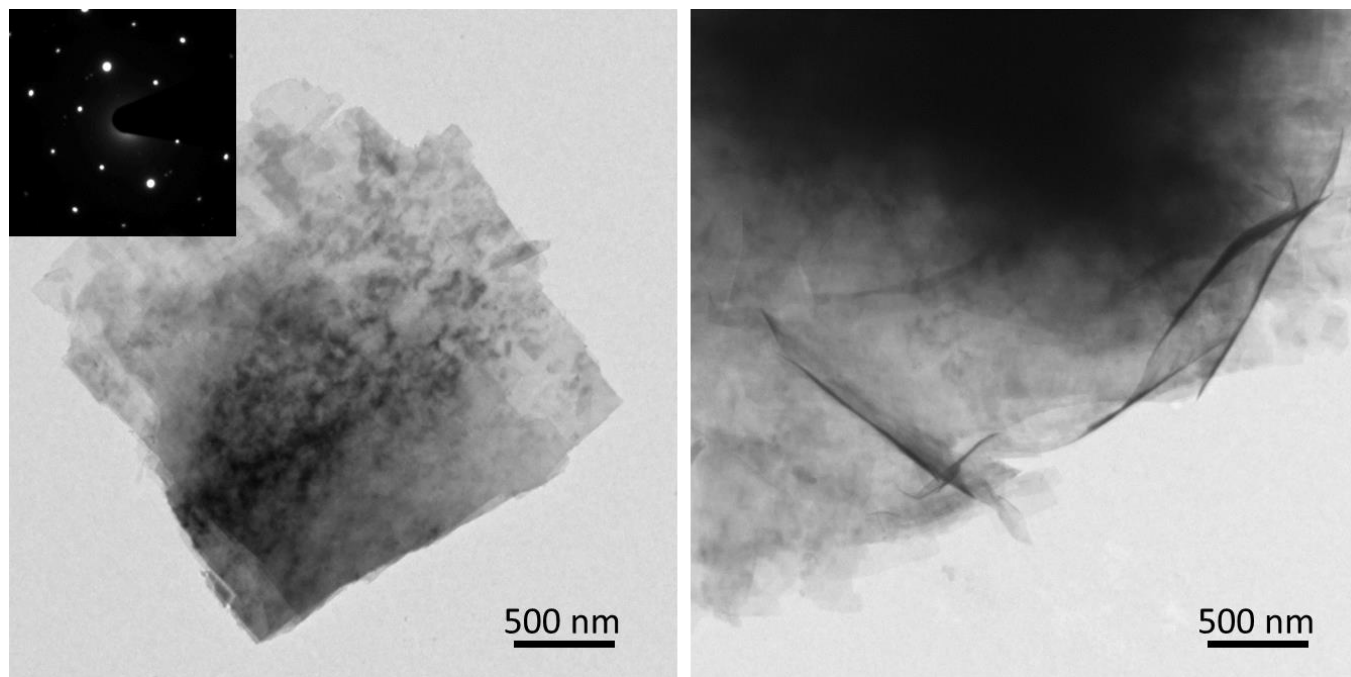


Figure 3.11. TEM images of the Li₂-2.7 sample.

Since this technique results in an image that is based on the thickness of the material, the morphology can be closely examined to see the density of the material at any given point of the image. The more transparent the sample at a given location, the smaller the thickness. Also, the wavy, wrinkled nature of the sheets can be observed, demonstrating the flexibility or ability for the sheets to bend; this is not as noticeable in the smaller aspect ratio platelets in Figure 3.12:

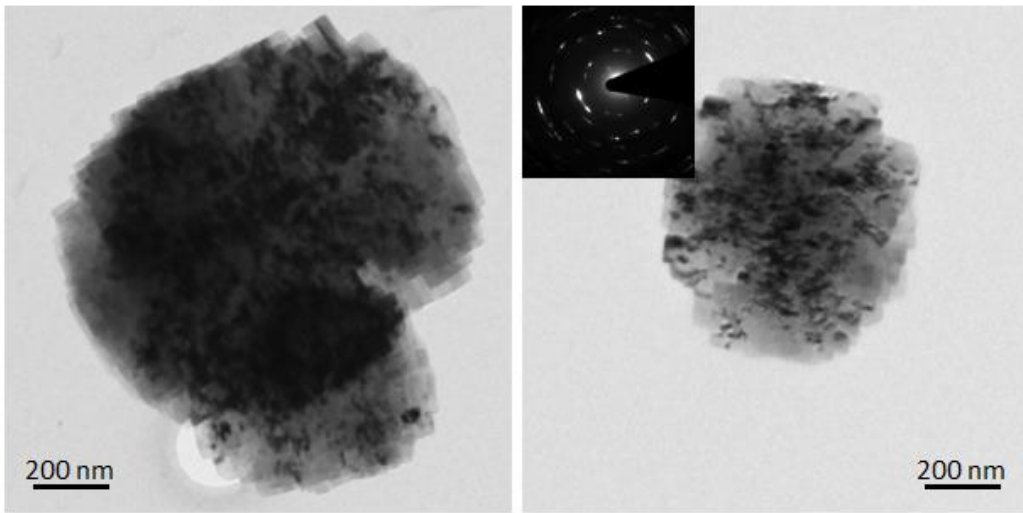


Figure 3.12. TEM images of the Li_{2-3.7} sample.

These samples do not allow as many electrons to be transmitted due to the thicker nature of these platelets. These low aspect-ratio. Rigid sheets also appear to potentially have more surface defects with all of the dark, thicker LFP growth.

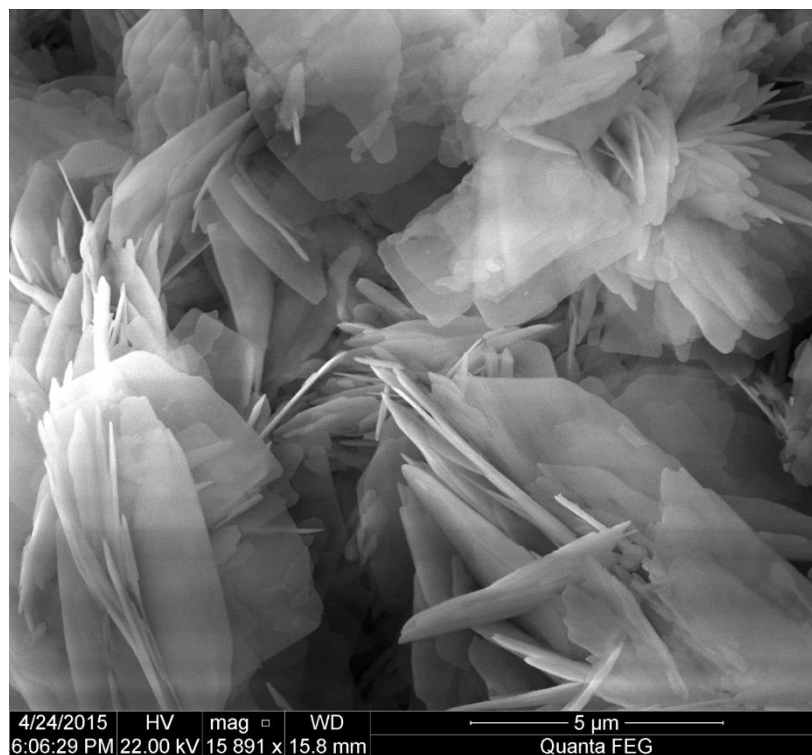


Figure 3.13. SEM image of the standard pH sample from doubling the LiCl content (Li3-1.5). This synthesis condition formed fairly uniform nanosheets, and their thin nature and flexibility can be observed in the TEM images of Figure 4.14:

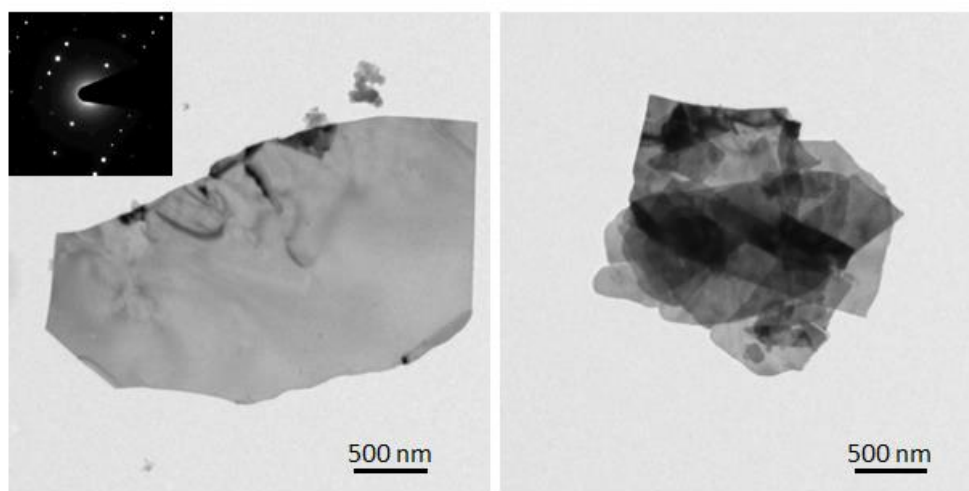


Figure 3.14. TEM images of the L3-1.5 sample.

These images show that the L3-1.5 sample appears to have the thinnest morphology due to the delicate wrinkles that symbolize flexibility in the thin sheets and high aspect ratio of the diameter to the thickness. To measure the thickness of the synthesized morphologies, atomic force microscopy was utilized to analyze the topographical elevation characteristics of the samples:

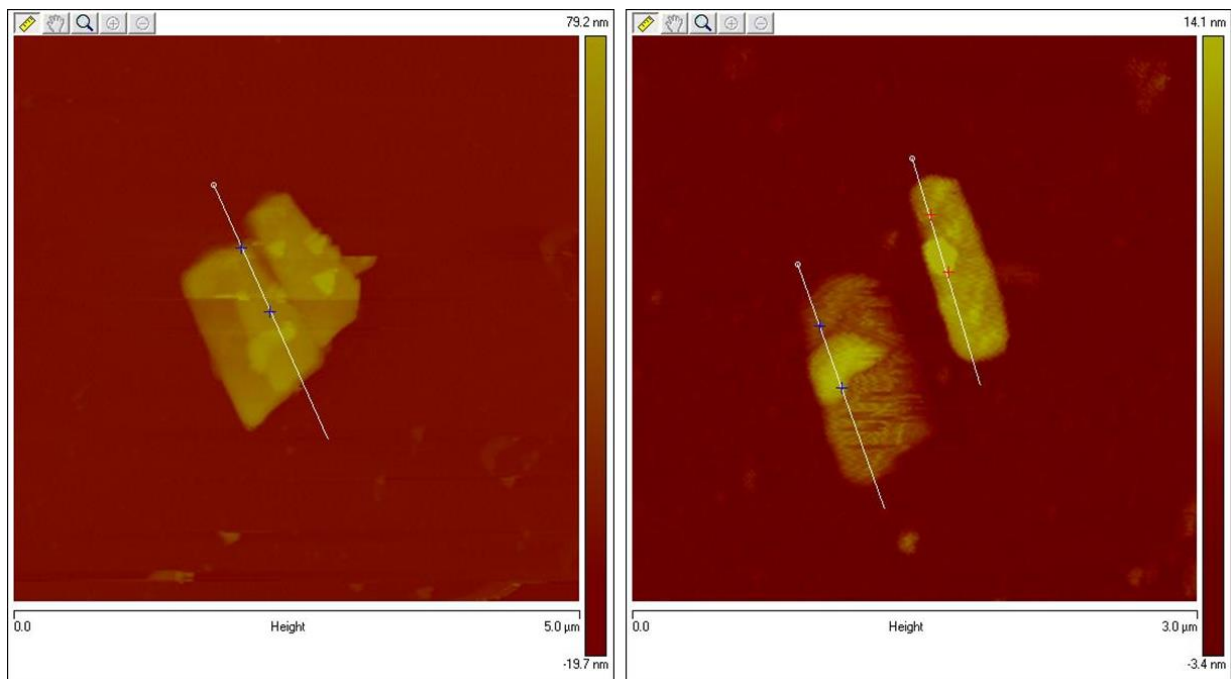


Figure 3.15. AFM images of LFP Li2-2.7 (left) and Li3-1.5 (right).

The LFP Li2-2.7 nanosheets are approximately 80 nm in thickness, while the LFP Li3-1.5 nanosheets are approximately 12 nm thick, the thinnest to date. By doubling the amount of LiCl added, and thus both Li^+ and Cl^- content, the pH decreased to pH 1.5 from the natural state of the system, 1.7 pH. These thinner nanosheets from the Li3-1.5 synthesis yield a much shorter diffusion path in the [010] direction, allowing the structures to potentially have a much higher power density. By systematically varying the pH of the Li3 system to match the pH of the Li2 system, the effects of doubling the LiCl content can be studied independently by holding pH constant. The structures obtained in the Li3 system are shown in the SEM images in Figure 3.16:

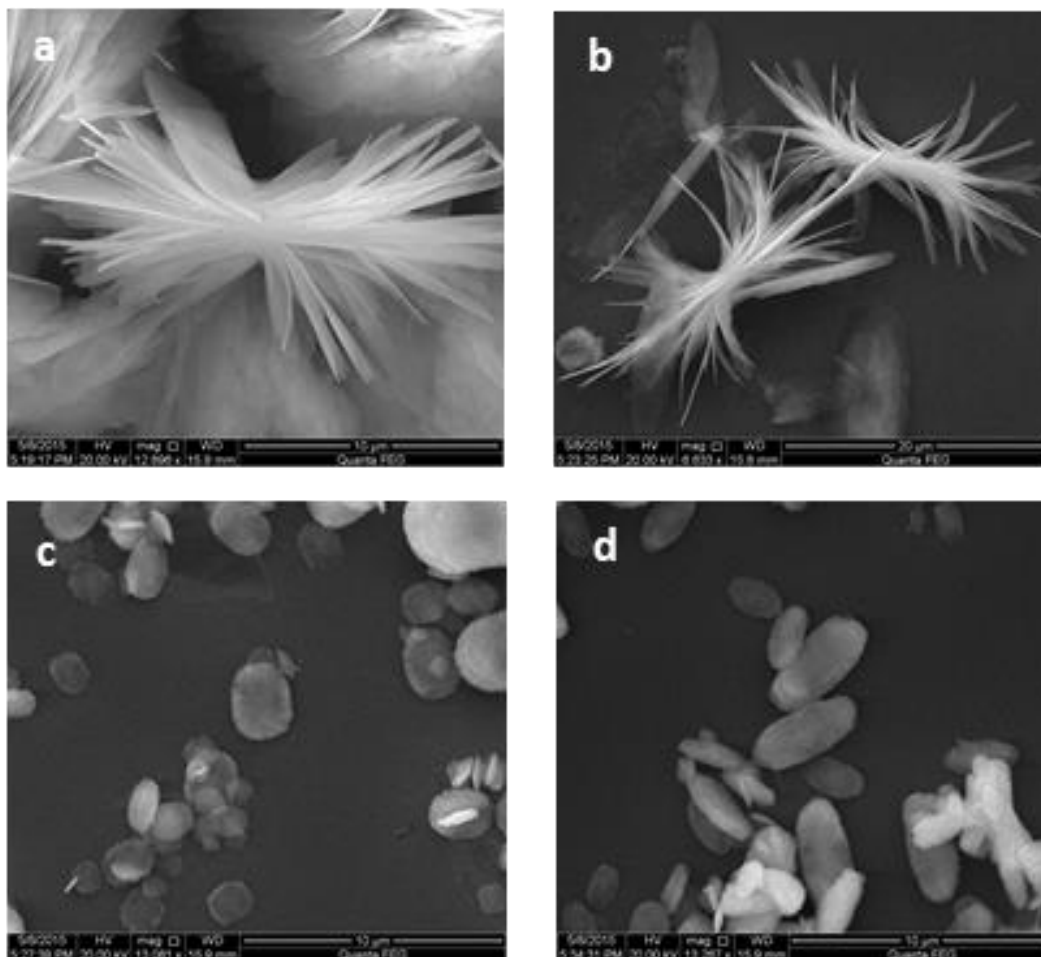


Figure 3.16. SEM images of pH-varied structures a) Li3-1.7, b) Li3-2.7, c) Li3-3.7, and d) Li3-5.1.

The structures at elevated pH changed drastically from the large, fairly loose nanosheets from Li3-1.5 (Figure before this one). The structures in a (pH 1.7) and b (pH 2.7) stem from a central point and flare out at the ends. Then, c (pH 3.7) makes ovals and d (pH 5.1) makes even more elongated ovals.

In order to check the material composition of the samples, XRD was performed for each of the different structures synthesized, shown in Figure 3.17:

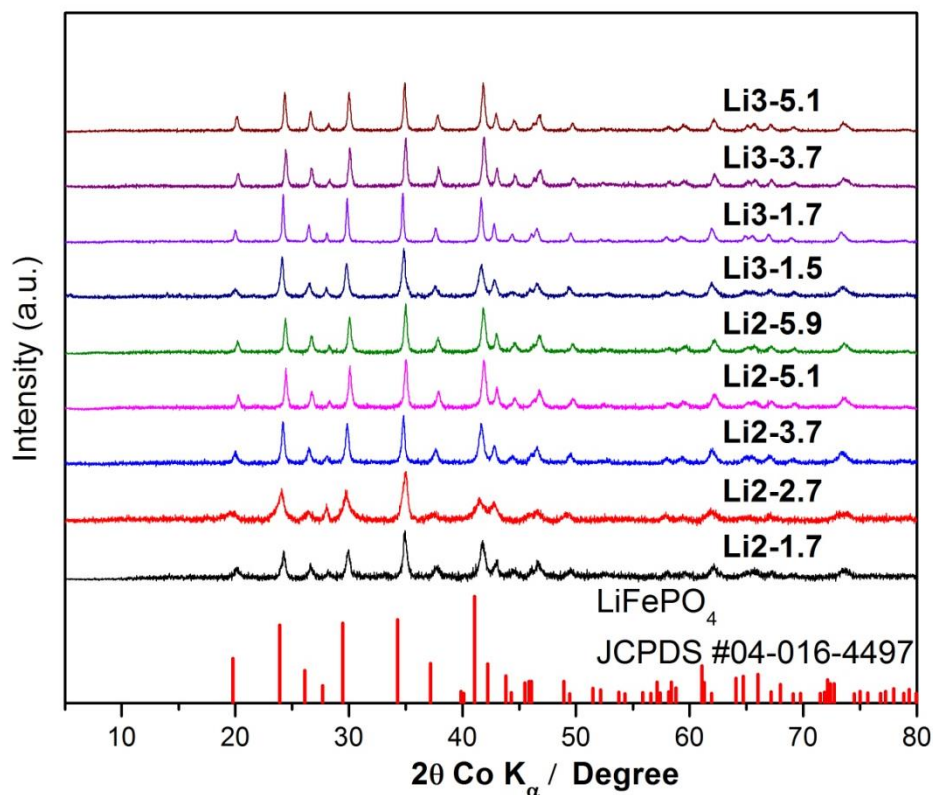


Figure 3.17. XRD patterns of the different LFP syntheses. The peaks correspond to the database signature pattern for LiFePO₄ (vertical red lines), JCPDS #04-016-4497.

XRD characterization for all of the compounds matches up to expected peaks for LiFePO₄, with no detected impurities. Peak broadening is observed for Li2-2.7, due to the nanosheet-like morphology. Intensity of peak at 26.7 2 theta (021) plane is less than the peak intensity at 28.4 2 theta (010) plane, indicating greater exposed facets of the (010) plane for the L2-2.7 sample.

From the XRD scan of the LFP-NSN, it can be observed from the alignment of the vertical bars that represent the Bragg positions with the sample that high-purity LFP has been synthesized with no noticeably distinguishable contaminant peaks for impurities such as the commonly reported Li₃PO₄, Li₃Fe₂(PO₄)₃, and conductive FeP¹³². Further, it has been observed that for a higher magnitude of the (020) peak over the (200), platelet or sheet-like structures are expected (needle shaped crystals are observed for the opposite case).^{132, 138} Since the XRD data shows the

(020) plane as the highest-intensity peak, there was no immediate need to distinguish the peak further by drop-casting the structures on a surface to allow for this plane to have predominant vertical exposure to the x-rays as shown in Figure 3.18:

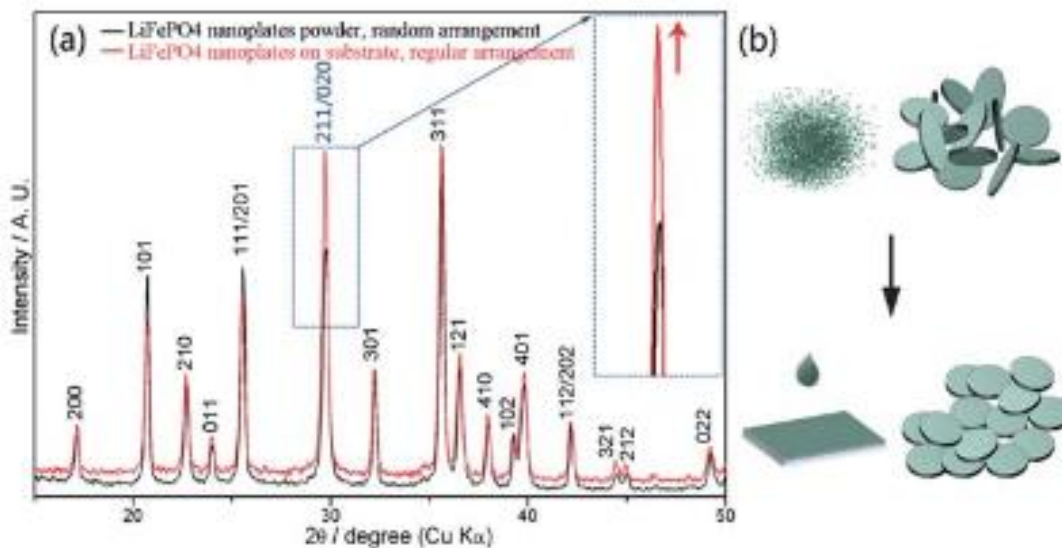


Figure 3.18. (a) XRD patterns of random and regular arrangement LFP and (b) schematic of regular and random arrangement.¹⁵²

Raman Characterization

Raman spectroscopy for the L2-2.7, L2-3.7, and L3-1.5 samples was performed on a Renishaw Raman with a 633 nm laser, 20x magnification, and an exposure time of 30s shown in Figure 3.19. One dominant band at approximately 948 cm^{-1} is evident in the spectroscopy, which is assigned to the ν_1 stretching mode of the PO_4^{3-} group of LiFePO_4 .¹⁵³ This is the characteristic stretching mode of the phosphate tetrahedron configuration, which is characteristic of pristine LFP.

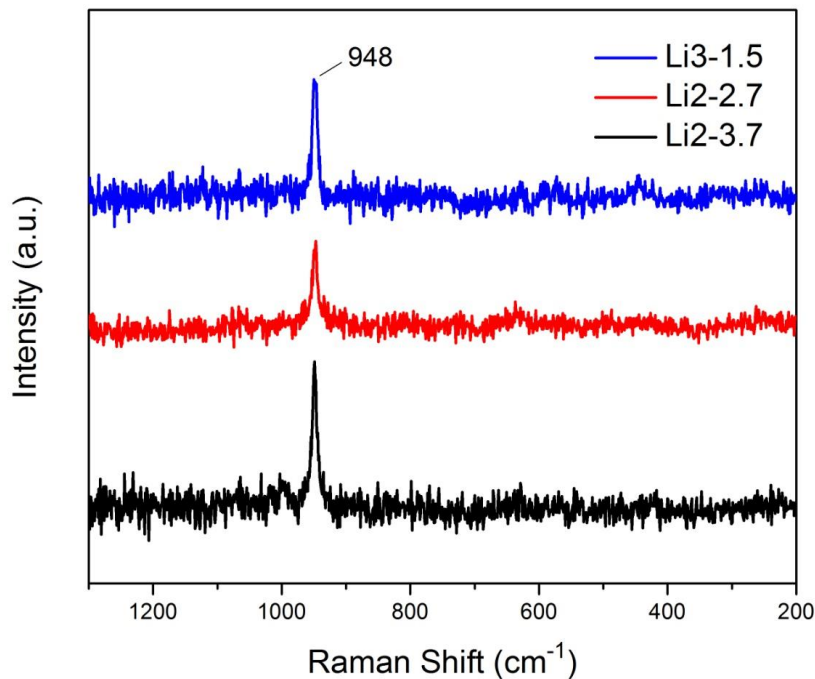


Figure 3.19: Raman spectroscopy signal for Li₃-1.5, Li₂-2.7, and Li₂-3.7.

Conclusions

Microwave irradiation could be a viable means to shorten reaction times, as well as being easy to employ to a process for scale-up and mass production of the $\langle 010 \rangle$ thickness and $\{010\}$ lateral dimension controlled LFP nanosheets for lithium ion battery cathodes. However, often, to synthesize delicate, thin or narrow morphologies of nanostructures, slow growth is often necessary. This is the first reporting of modulating $\langle 010 \rangle$ thickness in LFP platelike structures by pH in a solvothermal method. Also, this method is very simple to modulate the particle sizes by simply adding a known volume of standard, 10 M KOH solution. By increasing the Cl⁻ content, ultrathin, ~12 nm LFP nanosheets can be grown by a bottom-up approach, which could inevitably lead to extremely fast charge times for LIBs.

CHAPTER 4

LITHIUM IRON PHOSPHATE NANOSHEET ELECTROCHEMICAL EVALUATION IN LITHIUM ION BATTERY (LIB) COIN CELLS

The advent, commercialization, and mass production of a secondary (rechargeable) lithium ion batteries by Sony Corporation¹⁵⁴, starting in 1990, led to the reformation and drastic improvement of the portable electronics industry. These batteries include a network of electrochemical cells that typically contain a lithium-transition metal compound cathode (including aluminum current collector) that is separated from a graphite anode (including copper current collector) by a separator film (e.g. polypropylene) that passes a lithium salt-containing organic electrolyte (e.g. LiPF_6 dissolved in a mixture of dimethyl carbonate/ethylene carbonate). Here, upon charging the battery, a flow of electrons (externally in an electrical circuit) and lithium ions (through the electrolyte) to the anode under an applied bias to force lithium to intercalate in the graphite, and upon battery discharge, both electrons and ions flow in the opposite direction and intercalate in the lithium-transition metal compound at the cathode (Figure 4.1).

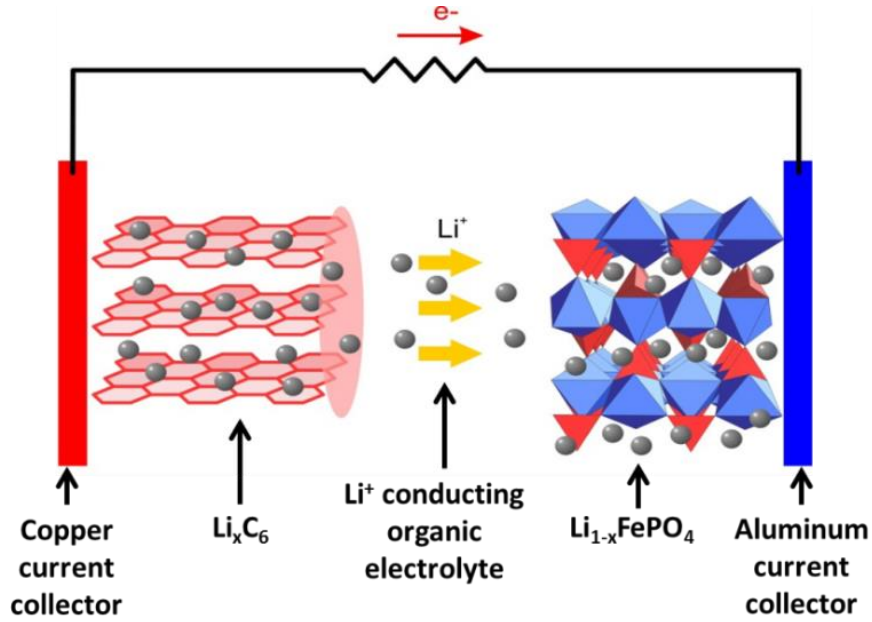
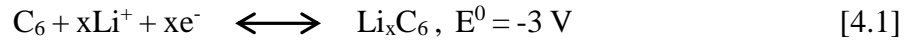


Figure 4.1. Schematic of LIB discharge mechanism showing lithium diffusion into LFP.¹⁵⁵

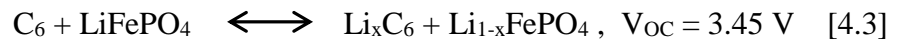
These intercalation processes are reversible for these secondary batteries, following the half-reaction scheme for the anode:



The half-reaction scheme for the cathode:



And the full cell reaction:



Here, the full-cell open circuit potential is equal to the cathode potential minus the anode potential, or absolute difference, 3.45 V. Due to these reversible reactions, the Li^+ ions “rock” back and forth between the anode and cathode, leading to these batteries being called “rocking-chair” batteries.

Further, on discharge, the battery’s ionic current ($I_i = I$) internal battery resistance R_b makes a reduction in the battery output voltage V_{dis} from the open-circuit voltage V_{OC} due to a

polarization $\eta = I_{dis}R_b$ and causes an increase in the voltage V_{ch} to reverse this reaction upon charge due to an overpotential, or increased bias to drive the reaction, $\eta = I_{ch}R_b$:

$$V_{dis} = V_{OC} - \eta(q, I_{dis}) \quad [4.4]$$

$$V_{ch} = V_{OC} - \eta(q, I_{ch}) \quad [4.5]$$

here, q is defined as the state of charge. At a fixed current I , the cell's percent efficiency to store energy is:

$$\frac{\int_0^{Q_{dis}} V_{dis}(q) dq}{\int_0^{Q_{ch}} V_{ch}(q) dq} \times 100 \% \quad [4.6]$$

where:

$$Q = \int_0^{\Delta t} I dt = \int_0^Q dq \quad [4.7]$$

where Q is the total charge the current $I = dq/dt$ transfers per unit weight ($Ah \text{ kg}^{-1}$) or per volume ($Ah \text{ L}^{-1}$) during charge or discharge. The cell capacity for a given current is represented as $Q(I)$, since Q is limited by the diffusion of ions through the electrolyte and electrode at increased currents, making a reversible loss of capacity. On the other hand, an irreversible loss of capacity can be caused by electrode decomposition, electrolyte-electrode chemical reactions, and changes in the electrode volume. On the first charge of a discharged electrode, electrolyte reacts with the electrode, forming an irreversible passivation layer known as the solid-electrolyte interphase (SEI), which is not associated with the fade in capacity associated with battery cycling. This capacity fade is represented by the Coulombic efficiency per cycle:

$$\frac{Q_{dis}}{Q_{ch}} \times 100 \% \quad [4.8]$$

Further, the lifetime of a battery is defined as the number of cycles a battery can withstand before experiencing a capacity fade of 80% of the initial reversible value. Aside from battery safety and cost, other key factors of importance are the energy density (specific or per mass and

volumetric or per volume), power output at a given current $P(q) = V(q)I_{\text{dis}}$, and the calendar life or shelf life of the battery. A fully charged cell's available energy E is measured based on the discharge current $I_{\text{dis}} = dq/dt$ multiplied by the time Δt it takes to fully discharge at this rate:

$$E = \int_0^{\Delta t} IV(t)dt = \int_0^Q V(q)dq \quad [4.9]$$

The gravimetric energy density (Wh kg^{-1}) and volumetric energy density (Wh L^{-1}) are dependent on the discharge current, I_{dis} , via $Q(I_{\text{dis}})$ and are particularly interesting in portable or transitory batteries for laptops, hand-held devices, and electric vehicles. Another term of importance is the “tap density”, which represents the packing density of electrochemically active electrode particles, measured as the volume ratio of active particles in a cylinder after “tapping” or packing the material.¹⁵⁶

Lithium Ion Diffusion Coefficient in LFP

The diffusion coefficient of LFP has been widely studied in literature. Using AC impedance spectroscopy, it has been found that the diffusion coefficient for lithium ions is 1.8×10^{-14} and $2.2 \times 10^{-16} \text{ cm}^2\text{s}^{-1}$ for LiFePO_4 and FePO_4 , respectively¹⁵⁷. Potentiostatic and galvanostatic titration techniques have shown that based on the phase ratio of $\text{LiFePO}_4/\text{FePO}_4$ or lithium content in Li_xFePO_4 and $\text{Li}_{1-x}\text{FePO}_4$ ($x < 0.02$) makes the lithium ion diffusion coefficient vary from 10^{-10} - $10^{-16} \text{ cm}^2 \text{ s}^{-1}$.¹⁵⁸

Conductivity

Lithium iron phosphate does not naturally have a high electrical conductivity, only featuring $10^{-10} \text{ S cm}^{-1}$.¹⁵⁹ One way to increase the conductivity is to introduce defects in LFP through doping. An example of this shows that $\text{LiFe}_{1-x}\text{Co}_x\text{PO}_4/\text{C}$ with $x = 0.010$ (out of $x = 0, 0.005, 0.010, \text{ and } 0.020$) achieves the best electrochemical properties, showing discharge capacities of 114.8 and $104.2 \text{ mAh}\cdot\text{g}^{-1}$ at 10 C and 20 C , respectively¹⁶⁰. Similar results were also

attained for the same 1 % Co doping in $\text{LiFe}_{0.99}\text{Co}_{0.01}\text{PO}_4/\text{C}$ nanoplates, where they achieved over $96.9 \text{ mAh}\cdot\text{g}^{-1}$ and good cycling specific capacity retention at 10 C ¹⁶¹. Another study that used $\text{LiFe}_{0.9}\text{M}_{0.1}\text{PO}_4/\text{C}$ (M = Mg, Co, Ni) demonstrated that those doped with Mg and Co had lower specific capacities than LFP, and the one doped with Ni had higher specific capacity than LFP when cycled at $\text{C}/10$.¹⁶²

Experimental

Preparation of LFP-NS/C

To add a carbon thin film, LFP-NS were dissolved in a water-ethanol mixture and 5 % wt. glucose (per LFP-NS) was added. The solution was stirred for two hours to ensure thorough mixing. Then, the solution was concentrated to dry in an oven at $80 \text{ }^\circ\text{C}$ overnight. The resulting precipitate was ground to a fine powder with a mortar and pestle and evenly distributed in the bottom of a ceramic boat. The boat was placed in a quartz tube furnace, purged with Ar for thirty minutes, ramped to $700 \text{ }^\circ\text{C}$ at $10 \text{ }^\circ\text{C}/\text{min}$, held there for 1 hour, and allowed to cool to room temperature before turning off the Ar. The resulting powder changed from white to black.

Surface Carbon Coating

Carbon coating techniques and different carbon precursors have been extensively studied for active materials in LIBs. It has proven difficult to determine the optimal carbon film coating content (% wt.) and thickness, where a high carbon content boosts conductivity but can make the coating layer thicker than 3-5 nm, making the tap density lower and more difficulty for Li^+ penetration¹⁶³. It has been found that polyaromatic carbon sources like naphthalenetetracarboxylicdianhydride can provide for a more graphitic coating with sp^2 nature, which can provide enhanced battery performance over higher loadings of amorphous carbon coatings¹⁶⁴. Another

interesting method to attempt to deposit uniform carbon films is to dissolve a carbon source, such as sucrose octaacetate (SOA) in liquid CO₂ (*l*-CO₂), and coat LFP particles through solution film entrainment by evaporating the *l*-CO₂ followed by calcination¹⁶⁵. This makes uniform 3.3 nm carbon coatings on LFP at 1.9 % wt. carbon content and forms carbon nanowires between particles, shown in Figure 4.2.

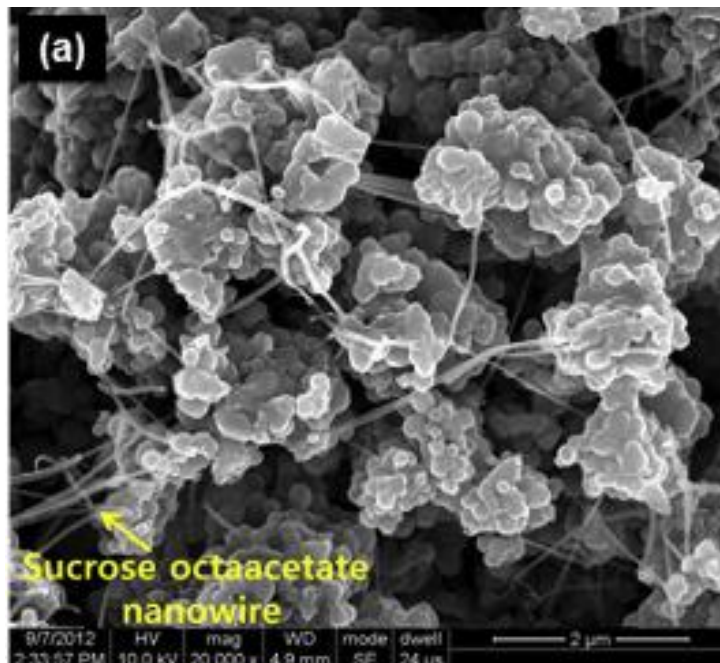


Figure 4.2. SEM image of *l*-CO₂-SOA carbon coating of LFP.¹⁶⁵

LFP is often protected from the electrolyte by an amorphous carbon layer to allow it to retain its specific capacity at high cycle numbers. LFP nanosheets have had carbon layers pyrolyzed on them using simple sugar carbon sources like glucose or polymers like polyethylene oxide in an inert atmosphere (Ar or N₂) with hydrogen gas between 550 and 700 °C^{147, 166}. Saravanan et al. discusses the chelating ability of D-gluconic acid lactone for Fe (as an in situ carbon source added during LFP synthesis) and how it forms a uniform, 5 nm carbon coating that allow their nanoplatelet micro-assemblies achieve 163 mAhg⁻¹.¹³²

for 8 hours at 250 °C to grow LFP particles on the reduced graphene oxide, collect the precipitate and mix it with citric acid, and anneal this at 600 °C for 3 hours under Ar/H₂, resulting in graphene decorated with LFP and carbon coated.¹⁶⁸ This intimate contact of LFP on graphene and subsequent carbon coating is reported to achieve 90 mAh·g⁻¹ at 10 C. Nitrogen-doped graphene-LFP composites have also shown promising electrochemical performance due to the heightened electrical conductivity attributed to the nitrogen doped graphene.¹⁶⁹

Other methods focus on wrapping graphene around LFP nanosheets to improve conductivity and capacity. One method binds graphene to carbon coated LFP through van der Waals interactions and increases the capacity above the theoretical capacity (170 mAh·g⁻¹) to 208 mAh·g⁻¹ which they attributed to the lithium ions in the electrolyte undergoing a reversible reduction-oxidation reaction with the graphene flakes, which have a specific capacity of ~ 2000 mAh·g⁻¹.¹⁷⁰ For this, they put graphene in dimethylformamide and add the carbon-coated LFP such that it is wrapped by graphene by the afore-mentioned van der Waals interactions. They also noted that this specific capacity enhancement effect is significant, only requiring a small amount of graphene (< 2 wt. %), and this low loading also serves to avoid the undesired voltage-polarization effect that affects cathodes with higher graphene loadings.

Battery Assembly

Figuring out the proper active material slurry composition can be one of the most difficult aspects of assembling lithium ion batteries. The ratio of solids in the slurry are often employed in an 80:10:10 ratio of active material:carbon particles:polymer binder. For the cathode LFP project, this ratio consists of LFP:Super C Carbon:polyvinylidene fluoride (PVDF). This ratio is fairly standard, but often, literature does not report the wt. ratio of binder to N-methyl-pyrrolidone (NMP), a widely used solvent to dissolve PVDF. Using 0.3 g of active material and thus 37.5 mg

of both Super P carbon and PVDF, a few different volumes of NMP were employed before reaching a suitable slurry consistency. After using 5 mL and then 3 mL of NMP to 37.5 mg PVDF with unsuccessful battery results, a method in a patent that employs 1.5 mL NMP to 37.5 mg PVDF¹⁷¹ was investigated. Initially, this ratio was unsuccessful as well when the PVDF was simply stirred into the NMP overnight (and other components added and stirred subsequent night). Then, upon using an ultrasonic bath to disperse the PVDF in NMP for 30 minutes before stirring overnight, adding the carbon and active material, stirring overnight again, spreading on aluminum foil and drying, relatively high specific capacity was maintained at increased cycle numbers for commercial LFP powder (Figure 4.4).

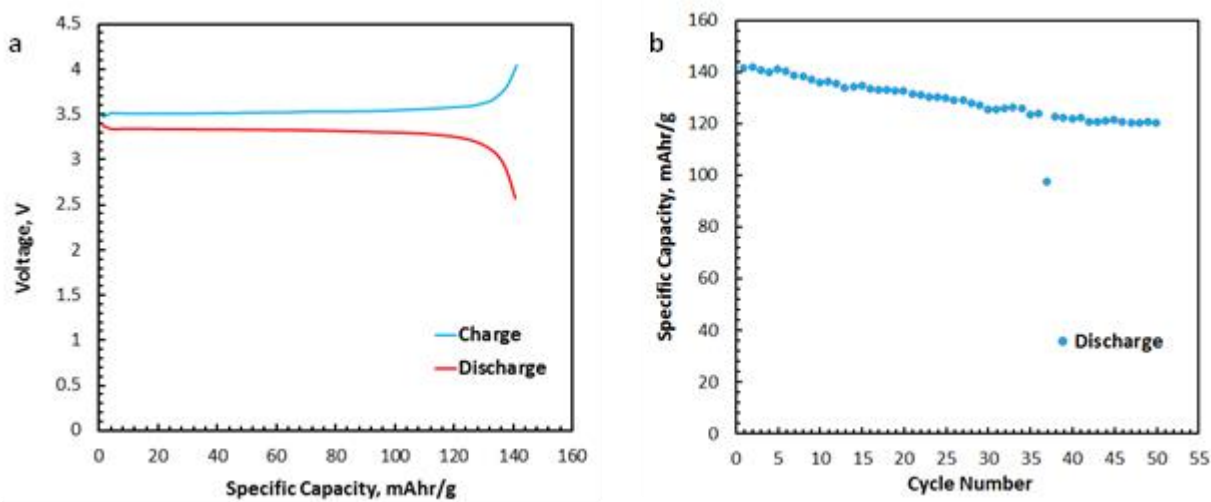


Figure 4.4. (a) Voltage v. Specific Capacity and (b) Specific Capacity v. Cycle Number for commercial lithium iron phosphate at C/5, 80:10:10 LFP:C:PVDF in 1.5 mL NMP.

When repeating the slurry ratio as reported in the procedure followed for our LFP nanosheet cluster synthesis, the batteries seemed to lack stability as shown in Figure 4.5 below.

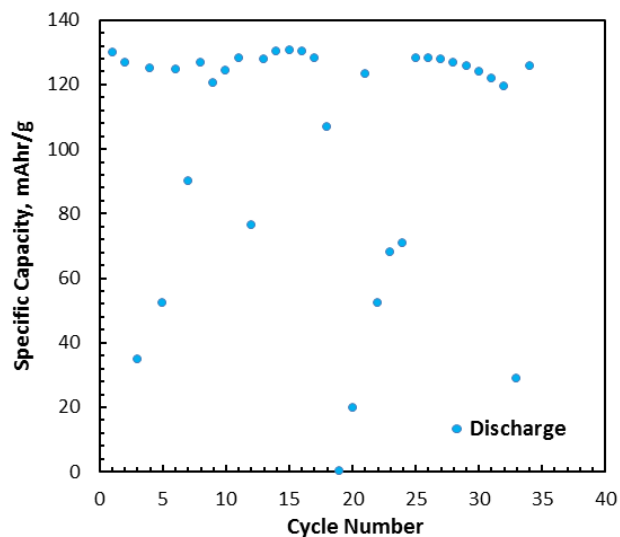


Figure 4.5. Specific Capacity v. Cycle Number for commercial lithium iron phosphate at C/5, 80:15:5 LFP:C:PVDF in 0.711 mL NMP (5 wt% PVDF to NMP).

Battery Preparation

A battery slurry was prepared by dissolving 37.5 mg of poly(vinylidene fluoride) (PVDF) in 1.5 mL N-methylpyrrolidone (NMP) via ultrasonication. After which, LFP-NS and Super C65 carbon were ground with mortar and pestle and dispersed into the stirring NMP-PVDF solution to make 80:10:10 LFP-NS:C:PVDF. The slurry was allowed to stir overnight and subsequently spread thinly on aluminum foil and dried in a vacuum oven at 70 °C overnight. The foil and slurry were then pressed at 10,000 psi to make sufficient contact with the foil. Disks of the active material were punched and weighed and assembled in a coin cell using a polypropylene separator film and lithium hexafluorophosphate (LiPF_6) as the electrolyte in 1:1:1 dimethyl carbonate:diethyl carbonate:ethylene carbonate. The batteries were then cycled on an Arbin Instruments Battery Test Station at various cycle rates to test the specific capacity or energy density at heightened C rates.

Results

15 wt. % carbon coatings were performed on LFP nanosheet structures synthesized at different precursor ratios, shown in the SEM images in Figure 4.6. The carbon coated structures in b) were closer to the argon inlet to the tube furnace than d) (both coated at the same time), and oxygen leaks in the system in stream oxidized b) to a greater extent, evidenced in the greater morphological change.

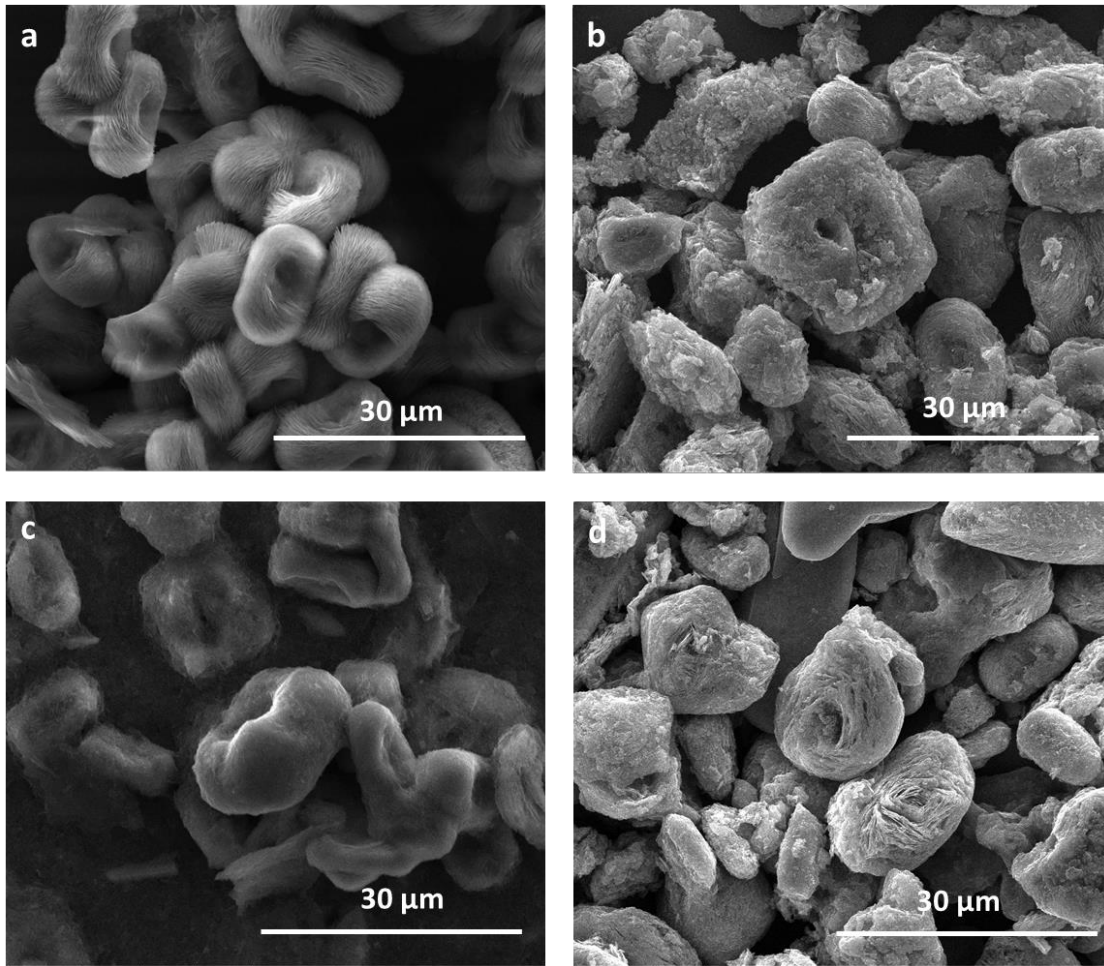


Figure 4.6. SEM images of LFP structures synthesized with a $\text{FeCl}_2:\text{LiH}_2\text{PO}_4:\text{LiCl}$ ratio of a) and b) 1:1.1:1 (b with 15 wt. % carbon coating from glucose) and c) and d) 1:1.1:1.1 (d with 15 wt. % carbon coating from glucose) with 5 % l-ascorbic acid (b and d ultrasonicated for 30 minutes in a bath sonicator before battery assembly).

Figure 4.7 shows battery data for carbon coated samples made with glucose as the carbon source. Four samples were made with different carbon sources and tested in batteries in attempts to increase conductivity and charge transfer in the batteries: 1) 2 % wt. rGO mixed in with active material/carbon black/ binder, 2) 15 % glucose mixed with the active material and calcined at 550 °C, 3) poly(ethylenimine) cationically physisorbed and calcined, and 4) GO hydrothermally mixed with LFP nanosheets to make a composite. All of this data is not shown here within due to complications with battery cycling.

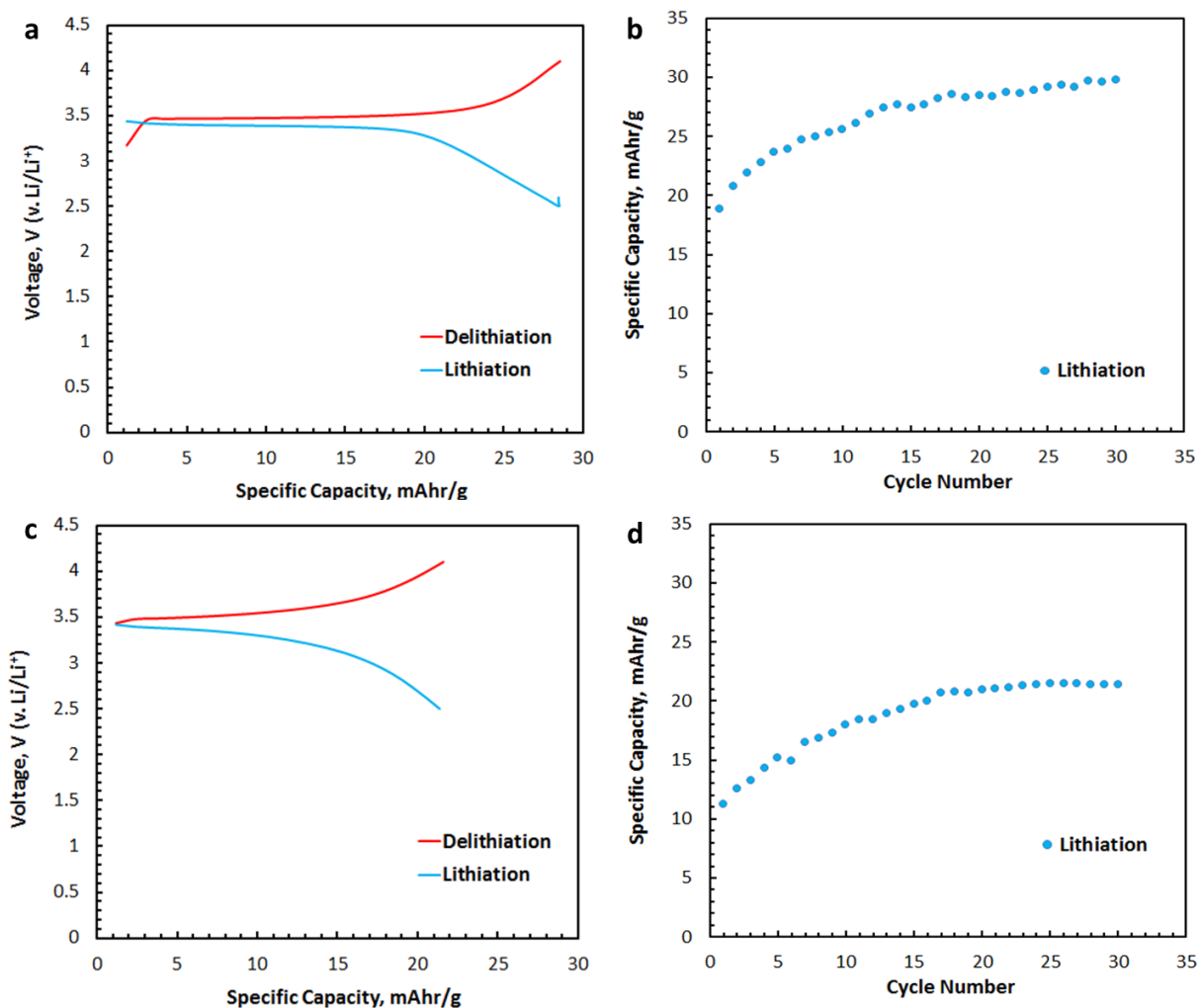


Figure 4.7. 1:1.1:1.1 FeCl₂:H₂PO₄:LiCl and 5 % Vc, a) and b) 15% wt. carbon coating and c) and d) 5 % wt. carbon (voltage v. specific capacity cycle 30).

At 15 wt. % carbon, it was initially believed that the carbon content was likely too high, and the thick layer of carbon was preventing adequate lithium ion migration into the lithium iron phosphate. Upon repeating this coating with 5 wt. % carbon, it is believed that since the specific capacity decreased significantly with decreased carbon coating content (Figure 4.3), the lithium was actually inserting in the carbon and not the LFP. It is further believed that trace amounts of oxygen were entering the furnace and causing the surface of the LFP to oxidize, blocking the Li^+ diffusion channels and making the material inactive.

Also, it was theorized in two models by Andersson and Thomas that after the first charge, unreacted FePO_4 remains at the center of large crystals, resulting in an irreversible capacity loss¹⁷², which we believe would also apply to the large ($\sim 15 \mu\text{m}$) “bird nest” shaped particles. Further, carbon coated samples undergo a process of activation during the first cycle, which can also cause an irreversible loss after the first charge¹⁷²⁻¹⁷³. It has also been noted that chlorine contaminants left from using an iron source with chlorine can undergo oxidation at elevated voltage ($\sim 3.9 \text{ V}$), leading to the partial corrosion of the current collector.¹⁷⁴

Conclusions

It is believed that the battery assembly incurred some error that prevented the achievement of high energy/high power density batteries. This could potentially be due to using stainless steel tweezers that may have provided a short circuit to the battery and thus applying too much current for the material to handle, thus destroying the active material and/or connectivity to the electrode. There could also be a lack of an intimate contact with the different shaped active material (nanosheets) with the conductive carbon (carbon nano- and micro- spheres). It is believed that the lack of positive battery results will soon be overcome and the 12 nm $\text{Li}_3\text{V}_2(\text{PO}_4)_3$ nanosheets (after carbon coating and making a composite with rGO) will achieve extremely high energy density at

very high C rates. It is believed that these thin sheets can be charged to nearly half of the theoretical capacity on the seconds scale and near the theoretical capacity on the minutes scale. LFP nanosheets of this extremely fine thickness have never before been achieved (in this case from a bottom-up synthesis approach) and have only been obtained for other battery materials through a top down approach via exfoliation of nanosheets. By recognizing the importance of the Cl^- ions as opposed to just the solvent adsorption and “soft-template” effect via hydrogen bonding, it allowed for the design of the growth-directed synthesis (without further modification) of the thinnest LFP nanosheets to date.

CHAPTER 5

PLATINUM AND PLATINUM-COBALT NANOWIRES FOR ENERGY CONVERSION IN PROTON EXCHANGE MEMBRANE FUEL CELLS (PEMFCs)

An Introduction to Proton Exchange Membrane Fuel Cells

By connecting the two half-reactions of a hydrogen fuel cell, the hydrogen oxidation reaction (HOR) and the oxygen reduction reaction (ORR), with an external circuit and a proton exchange membrane, chemical potential converts to workable electrical potential, generating only electricity and water. Proton exchange membrane fuel cells are a viable renewable energy solution for both stationary and mobile (transportation) energy demands. There are several types of fuel cells that offer solutions to provide for stationary power consumption, but the inherently lightweight, thin proton exchange (or polymer electrolyte) membrane (PEM) eliminates the need for heavy liquid electrolytes, which are typically a necessity in other electrochemical systems. In hydrogen fuel cells (PEMFCs), the PEM typically is comprised of Nafion, an ionomer that conducts protons along its polymerized sulfate groups. In this way, the oxidized hydrogen gas (protons) can easily traverse from anode to cathode by “hopping” along these sulfur-oxygen functionalities with no need for liquid electrolyte-dependent ion migration. The typical hydrogen fuel cell setup is shown in Figure 5.1¹⁷⁵:

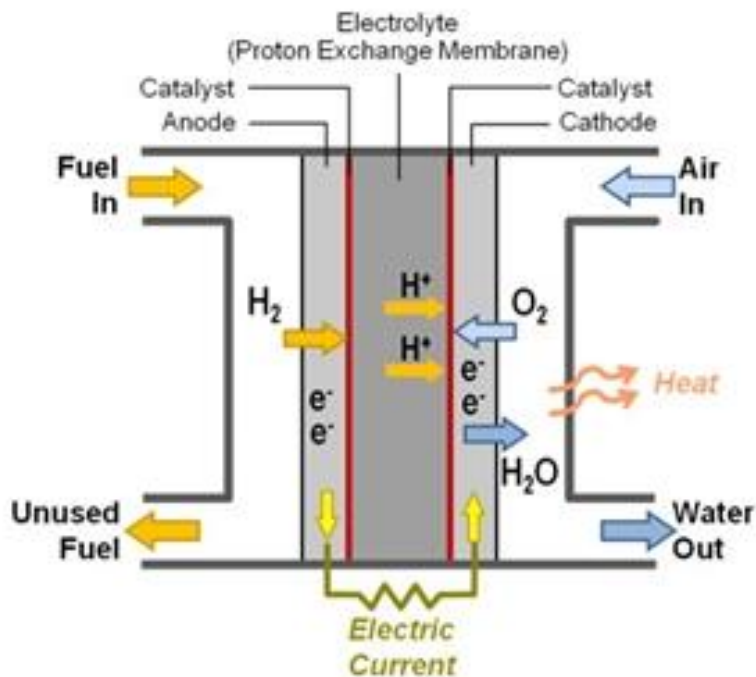


Figure 5.1. Schematic of proton exchange membrane “hydrogen” fuel cell (PEMFC) operation.¹⁷⁵

There are two serpentine tracks on each side of the fuel cell that meet flush with two sheets of catalyst-immobilized carbon paper sandwiched around a Nafion membrane (fluorinated polymer with dangling sulfate groups for proton conduction). At the anode, hydrogen enters and is oxidized by the catalyst into protons which travel across the membrane to the cathode and electrons that travel in an external circuit (generating amperage or current). These electrons arrive to the cathode, along with the protons from the membrane, and they combine with oxygen to reduce this chemical species to water.

All of this occurs around 85 °C, requiring this additional thermodynamic energy to aid the catalyst in reducing the oxygen to water. This reduction of water is the limiting factor and is more difficult to occur (requires more overpotential) than the oxidation of hydrogen.

Electrochemistry of Hydrogen Fuel Cells

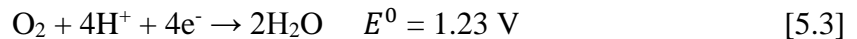
The overall electrochemical reactions that occur in a hydrogen fuel cell can be represented by the equation:



Here, the anode half-cell reduced and oxidized (respectively) species of interest are shown on the left side of the dashed line, and the cathode half-cell oxidized and reduced (respectively) species of interest are shown in the right side of the dashed line, which represents a junction that joins the electrolyte of the two half-cells and thus forms a full cell¹⁷⁶. Further, the potential difference across the full cell can be represented by:

$$E_{\text{cell}}^0 = E_{\text{cathode}}^0 - E_{\text{anode}}^0 \quad [5.2]$$

The half-reaction for the cathode can be represented:



And, the half-reaction for the anode can be represented:



These half-reactions display the redox potentials at which the half-reactions occur to the right of the chemical formulas (note that at the anode, hydrogen gas is split into two protons and two electrons, but by convention, the reduced species is shown on the right). Thus, the overall voltage that can be generated from a single hydrogen fuel cell full cell can be calculated as:

$$E_{\text{cell}}^0 = 1.23 \text{ V} - 0 \text{ V} = 1.23 \text{ V} \quad [5.5]$$

Thus, fuel cells are stacked both in series and parallel to increase the voltage and current (their product being power), respectively, to meet the power demands of an electric vehicle. Thus, single fuel cells are rarely seen and are found in fuel cell stacks to provide adequate power demands (Figure A 5.1¹⁷⁷).

E^0 is the standard electrode potential, which is measured relative to the normal hydrogen electrode (NHE), with species considered to have unit activity, $a_i = 1$. Considering half-reactions occurring at equilibrium, the potential, E , is related to E^0 by the Nernst equation¹⁷⁸:

$$E = E^0 - \frac{RT}{nF} \sum v_i \ln a_i \quad [5.6]$$

Here, the gas constant, R ($8.314 \text{ J K}^{-1} \text{ mol}^{-1}$), absolute temperature, T (K), the number of moles of electrons transferred, n (mol), the Faraday constant, F ($9.468 \times 10^4 \text{ C mol}^{-1}$), and the stoichiometric numbers for each species, v_i . Similarly, the Nernst equation can be approximated in terms of species concentrations, c_i ¹⁷⁸:

$$E = E^{0'} - \frac{RT}{nF} \sum v_i \ln c_i \quad [5.7]$$

Here, c_i is equal to a_i / γ_i , where γ_i is the activity coefficient of the species i . $E^{0'}$ represents the formal potential, including the logarithmic activity coefficient, depending on the medium. The Nernst equation can be applied when the oxidized and reduced species that take part in the electrode reaction are in equilibrium at its surface. Based on thermodynamic reversibility, this is then considered a reversible reaction. Thus, to apply this equation under reversible conditions, the ability of the electrode to reach equilibrium is dependent on time. Further, concentrations at the electrode interface depend on mass transport from the bulk solution, and to be considered a *reversible* reaction, the standard kinetic rate constant, k_o , must be much larger than the mass transfer coefficient, k_d . The opposite is true for *irreversible* reactions. Many reactions are *quasi-reversible*, meaning that under a small applied overpotential, or additional applied potential, the reactions can be reversed. For reduction, the rate constant's potential-dependent expression is as follows:

$$k_c = k_o \exp [-\alpha_c n F (E - E^{0'}) / RT] \quad [5.8]$$

And for the anode:

$$k_a = k_o \exp [-\alpha_a n F (E - E^0) / RT] \quad [5.9]$$

The charge-transfer coefficients for the cathode and anode are α_c and α_a , respectively, and represent the symmetry of the activation barrier. For a simple electron transfer process to a metallic electrode, these are close to 0.5. The standard kinetic rate constant, k_o , is the rate constant at $E = E^0$.¹⁷⁸

For experimental purposes, a more practical method studying and expressing rates of electrode reactions is through *exchange current*, I_o , representing the cathodic or anodic partial current at equilibrium potential, E_{eq} . Measuring this current is analogous to measuring the standard rate constant, k_o , as they are directly proportional. Current, I , is exponentially dependent on potential, forming a linear relationship between $\log I$ and potential, known as the *Tafel relation*. This rate is dependent on the rate constant and concentration of the reagents, and it cannot increase indefinitely due to a transport-limited, diminished supply of reactants.¹⁷⁸

Only thermodynamic and mass transport parameters can be determined for reversible reactions, whereas both kinetic and thermodynamic parameters can be determined for quasi-reversible and irreversible reactions. Further, reaction kinetics can be greatly affected by the electrode material and configuration.¹⁷⁸

The rate of electron transfer is an adiabatic process that follows the Franck-Condon principle, occurring at approximately 10^{-16} s. Thus, the electrode reaction rate constant does not measure this rate of electron transfer, but rather measures the time required for the species to arrange in their ionic atmospheres to transfer electrons upon incidence with the interfacial region.¹⁷⁸

To study reaction kinetics in the absence of diffusion, a convective-diffusion system is typically employed with a rotating disk electrode (RDE), or a modification thereof allowing for

the study of two-step reactions: the rotating ring-disk electrode (RRDE). In this type system, the electrode rotates and draws solution to the electrode surface as shown in Figure 5.2:

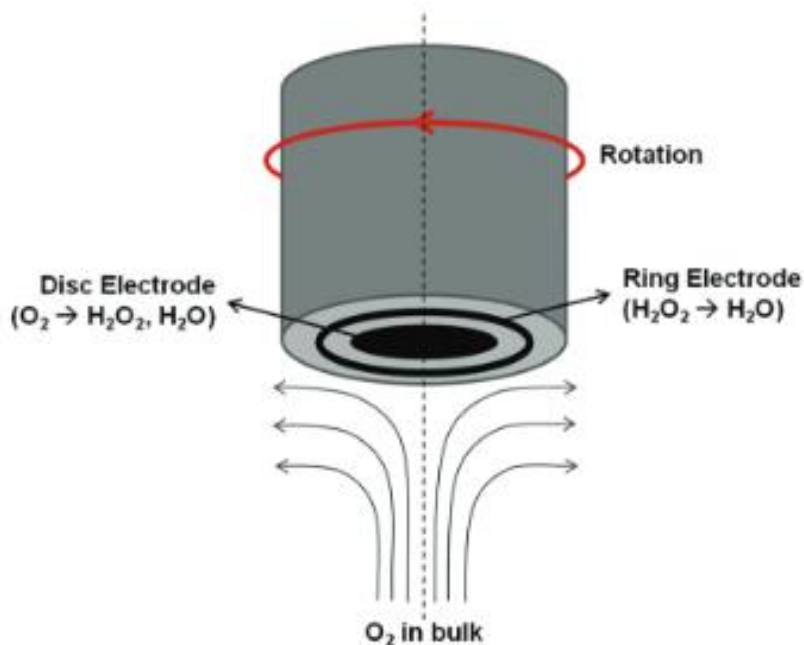


Figure 5.2. Rotating ring-disk electrode (RRDE) schematic for oxygen reduction.¹⁷⁹

In the absence of diffusion limitation, reaction kinetics can be studied to determine the reaction efficiency. Here, oxygen gas is reduced to water via a sluggish two-step, two-electron and two-proton process that forms hydrogen peroxide at the disk before repeating at the ring to form water. Also, the desired reaction process occurs on the disk, where a four-electron and four-proton process reduces oxygen directly to water. In the absence of diffusion, one can determine what fraction of oxygen is reduced by which reaction. For this, the Levich equation is employed to determine the linear range for current increase versus angular velocity of the RRDE:

$$I_L = 0.620nFAD^{\frac{2}{3}}\omega^{\frac{1}{2}}\nu^{-\frac{1}{6}}C \quad [5.10]$$

Where n is the number of electrons transferred, F (C/mol) is Faraday's constant, A (cm^2) is the cross-sectional area of the disk, D (cm^2/s) is the diffusion coefficient for the species of

interest (oxygen in the schematic), ω (rad/s) is the angular velocity of the electrode, and ν (cm^2/s) is the kinematic viscosity.

Non-Noble Metal Catalysts

Many attempts have been made to achieve high-activity non-noble metal catalysts, but it is difficult for them to compete with the catalytic nature of the electronic d-band configuration of noble metals. One example of a non-noble metal catalyst is generated through ball-milling graphite flakes with di-halides under Ar, resulting in halogenated graphene¹⁸⁰. Here, the halogen-functionalized graphene activity in alkaline solutions increased with halogen size, where the larger size halogen-halogen repulsion helped delaminate the graphene planes in the graphite sheets, and these edge sites had favorable binding affinity for O_2 molecules and weakened the O-O bonds with charge transfer induced by the halogens. Nitrogen-doped carbon nanotubes (NCNTs) serve as another example of a non-noble metal catalyst that is suggested to potentially replace platinum-based catalysts in fuel cells. In one work, chemical vapor deposition (CVD) was employed with ferrocene as a catalyst and ethylene-diamine (EDA) and pyridine (Py) as the nitrogen and carbon sources for nitrogen-doped nanotube growth, and the EDA-NCNTs had a 3-fold increased specific limiting current ($\text{j}/\text{mAcm}^{-2}$) over Py-NCNTs believed to be due to twice as many nitrogen atoms introduced per EDA as Py¹⁸¹. Also, they found the EDA-NCNTs to have a higher amount of quaternary nitrogen structure, which is more active than the pyrrolic structure of the Py-NCNTs. Here, in alkaline conditions, the EDA-NCNTs had a higher specific limiting current and lower Tafel slope than commercial Pt/C, indicative of a better catalyst; however, hydrogen fuel cell catalysts must operate in an acidic environment due to the nature of the protons, diminishing their usefulness for this application.

Small Diameter Supported Platinum Nanowires

Platinum nanowires can be formed through various routes. One method for their synthesis includes using formic acid as the reductant of hexachloroplatinic acid in water using carbon fiber paper as a substrate for the nucleation and growth of the Pt-nanowires (Pt-NWs)¹⁸². The selected-area electron diffraction (SAED) patterns of these nanowires show bright rings attributed to the ¹⁸³, {220}, {200}, and {111} Pt face-centered-cubic (fcc) crystal structure, similar to bulk Pt¹⁸⁴. This same growth mechanism has been used to grow ultrathin Pt nanowires on multiwall carbon nanotubes (MWCNTs)¹⁸⁵, nitrogen-doped carbon nanotubes(n-CNTs)¹⁸⁶, reduced graphene oxide (rGO)¹⁸⁷, sulfur-doped rGO¹⁸⁸, gold nanocores¹⁸⁹, and carbon nanospheres¹⁹⁰. In the study with sulfur-doped rGO, it was found that the electronegative sulfur groups helped the nanowires to seed and grow uniformly rather than forming patches of different length nanowires.

For this reaction method, pH and wt. % Pt were studied on carbon nanospheres (Figure 5.3), where they found pH 2.5 to result in near-exclusively nanowires, pH 4.5 to possess a mixture of nanowires and nanoparticles, and pH 10 is found to produce predominantly nanoparticles.¹⁹¹ They then studied platinum loadings of 20 wt. %, 40 wt. %, and 60 wt. % Pt at pH 2.5 and found the 20 wt. % Pt to have the highest activity on a per mass basis due to less overlap of the nanowires and unobstructed diffusion pathways. These nanowires are tens of nanometers, thus they do not incur aggregation, Ostwald ripening, and dissolution as likely as commercial Pt nanoparticles during fuel cell operations.¹⁹²

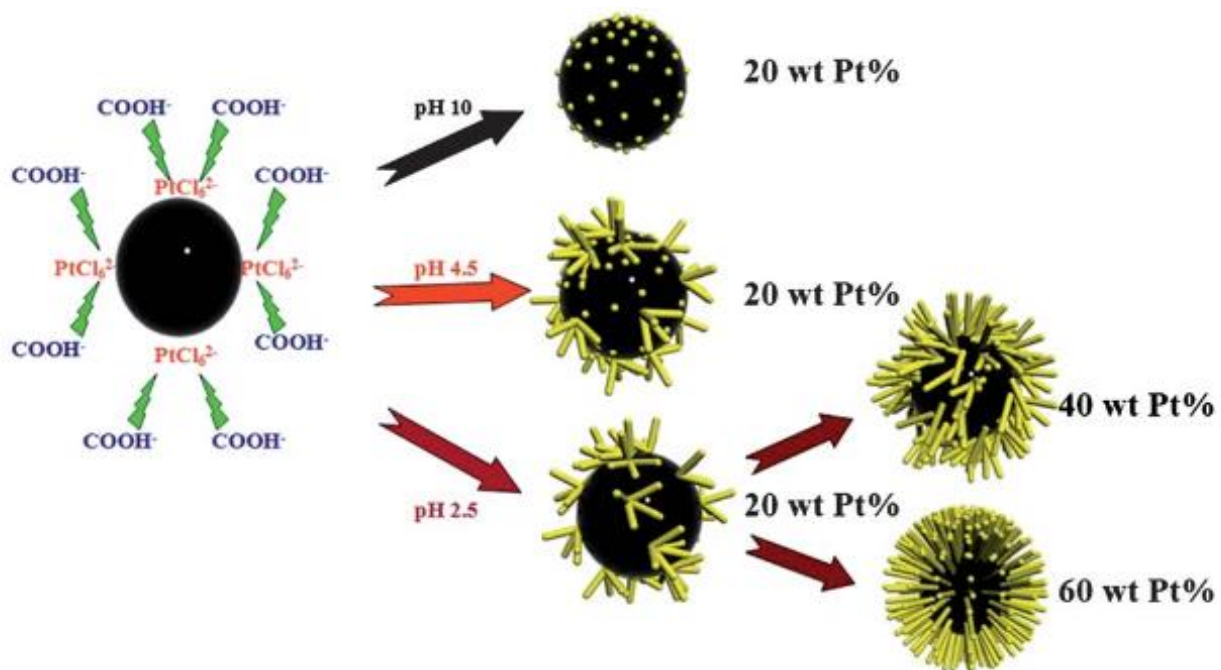


Figure 5.3. Platinum nanowire growth at different pH and wt. % Pt.¹⁹¹

Mixed Composition Nanowires

One interesting composition of unsupported nanowires consist of Pt-Co nanowire assemblies (NWAs) that stem from the center and grow to be ~ 5-10 nm in diameter and ~ 100-200 nm in length as shown in Figure 5.4.¹⁹³ These nanowires are not supported on a conductive substrate, which is usually found to provide higher activity than free-standing nanowires, but the assemblies themselves serve to keep the nanowires spaced out to prevent overlap of their electrochemically active surface area (ECSA). The lattice spacing of 0.22 nm is also slightly smaller than that of Pt (111) planes, demonstrating the successful incorporation of Co in Figure 5.4.

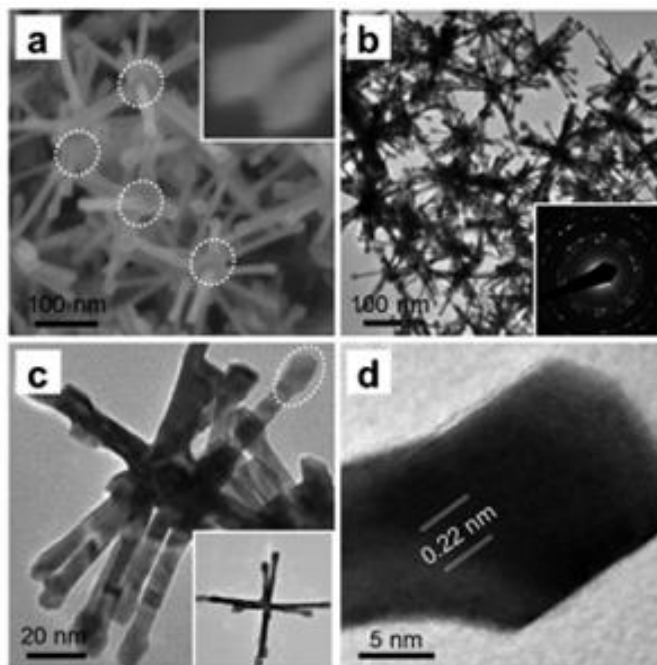


Figure 5.4. (a) SEM, (b) and (c) TEM, and (d) HRTEM images of Pt₃Co nanowire assemblies.

The inset in (b) shows the selected-area electron diffraction pattern of the NWAs.¹⁹³

Core-Shell Nanostructures

There are many core-shell architectures that have shown promise for electrochemical activity in fuel cells. One of these are Fe₃O₄-polydopamine-graphene-Pt (Fe₃O₄@PDA/RGO/Pt) yolk/shell structures¹⁹⁴. Here, the polydopamine serves as a modifier for graphene and a coupling agent for the Pt assembly. These structures are more stable and have heightened electrochemical activity in comparison to Pt/graphene with respect to the methanol oxidation reaction (MOR), and at the heterojunction interfaces between Pt nanoparticles and the support, they provide a synergistic cocatalyst effect that is further increased by the high immobilization and better dispersion of the Pt nanoparticles on the polydopamine functional groups.

Hollow Nanostructures

One form of hollow nanostructures consists of “hollow” Pt-Co/C core-shell nanoparticles that result from PEMFC operation aging due to the Kirkendall effect, a result of different diffusion rates of species in binary alloys due to a diffusion mechanism that is vacancy-mediated¹⁹⁵. These hollow nanostructures achieve a 1.5-fold higher oxygen reduction reaction (ORR) specific activity than the fresh Pt₃Co/C structures and 3-fold specific activity over the Pt/C nanoparticles. Another method of forming hollow nanostructures consists of coating ZnO nanowire arrays with Ni and then Pt, followed by etching away the ZnO with a weak sulfuric acid solution to result in PtNi nanotubes¹⁹⁶. At 0.6 V (versus a saturated calomel electrode, SCE) in 0.5 M H₂SO₄ and 0.5 M CH₃OH, these structures show a steady state current toward the MOR at 1000 s of 0.524 mA cm⁻² compared to 0.143 mA cm⁻² for Pt/C catalysts. A template wetting method coats porous alumina membranes with platinum (II) 2,4-pentanedionate (Pt(acac)₂) and poly(D,L-lactide) (PDLA) in a 3:1 ratio of chloroform, which are allowed to dry in air, followed by annealing in air for 24 hrs at 200 °C followed by 1 hr at 350 °C to reduce the Pt(acac)₂ to Pt⁰ and oxidize/remove the PDLA before etching away the template with KOH for 2 min¹⁹⁷. They found these nanotube arrays to have similar CO poisoning tolerance as commercial Pt black, yet they had a higher current response for formic acid electrooxidation due to heightened diffusion due to not requiring a polymeric binder such as Nafion as is required for the Pt black.

PtCo/C Nanoparticle Synthesis

The pH effects have been studied for PtCo nanoparticle synthesis on carbon by a sodium borohydride reduction of the metal salts, where an acidic solution (pH 2) yielded larger PtCo particles than a basic solution (pH 9).¹⁹⁸ The larger particles synthesized at the lower pH yielded higher electrochemical activity toward the ORR except at higher current densities, where the reduced electrochemically active surface area (ECSA) of the larger particles reduced the activity. The synthesis of PtCo nanoparticles by sodium formate or formate ion reduction has also been explored, where the initial composition of cobalt precursors did not match the reduced products, and the reductions had to be performed at elevated temperatures,¹⁹⁹ preventing the bi-component PtCo growth by the slow formate reduction method of the fine-diameter Pt nanowires studied by S. Sun et al.¹⁸⁵ After the reduction of these binary nanoparticles, they are typically annealed at over 700 °C to make uniform alloys that are stable in acidic solutions.¹⁹⁹ This also makes complications for 1-dimensional nanostructures, whose oblong nature makes them vulnerable to warping and morphological changes at high temperature. In another study, Pt₇₀Co₃₀ nanoparticle synthesis by the formic acid method and annealing at 900 °C proved these structures to not have as high of activity as the commercial Pt/C due to increased particle size and only partial alloying at the surface of the Pt₇₀Co₃₀ nanoparticles, where the authors concluded that the formic acid reduction is not a good way to make Pt₇₀Co₃₀ nanoparticles.²⁰⁰

Carbon Functionalization

Carbon is often functionalized by electronegative moieties before reducing the metal catalyst to help to make carbon more hydrophilic and to increase metal nanoparticle dispersion. This is often achieved with oxygen functional groups provided by a nitric acid treatment^{183,201}. There are other ways to add electronegative moieties, such as adding sulfite groups by a solvothermal treatment with sulfuric acid as well as organic replacement reactions that allow for carboxylic acid groups to be replaced via thiol esterification and amminization.

Experimental Synthesis of PtNWs/C

A nitric acid treatment¹⁸³ was used to create the functional groups C-O, C = O, and O – H²⁰¹ on the surface of carbon black. Briefly, vulcanized carbon was added to concentrated nitric acid (80 °C) and refluxed for 24 hours. This functionalized carbon was washed and filtered until pH neutral before drying overnight at 110 °C. The purpose of this was to convert the highly hydrophobic carbon black by spurning hydrophilation through functionalization. Also, these electronegative moieties are known to increase tethering and dispersion of transition metal nanoparticles and decrease the amount of overpotential necessary for catalysis²⁰². This nitric-acid treated, functionalized carbon will be referred to as C (instead of C-HNO₃ to be terse). Briefly, 2.5 mg of carbon nano- and micro-spheres (functionalized XC-72 Fuel Cell Store) were subjected to ultrasonic homogenization for 45 minutes in 2.5 mL deionized water. Next, 1.7 mg H₂PtCl₆·6H₂O (Sigma-Aldrich) was added to the vessel, followed by additional ultrasonic homogenization for 10 minutes. Then, 0.125 mL HCOOH (Sigma-Aldrich) was added, the pH was adjusted to 2.4 pH by 1 M NaOH (J.T. Baker), the system was briefly subjected to further ultrasonication, and the vessel is left to react undisturbed for more than 10 hours to ensure all of the Pt gets reduced. The structures

are then centrifugally separated, washed with deionized water twice and three times with ethanol, and are then dried in an oven at 60 °C overnight.

Experimental Synthesis of PtCoNWs/C

The second metal, cobalt, was reduced on platinum by sodium borohydride. The aforementioned procedure yielding PtNWs/C was employed again with 1.8 mg $\text{H}_2\text{PtCl}_6 \cdot 6\text{H}_2\text{O}$ to yield 21.3 % wt. Pt PtNWs/C. The structures were then added to an aqueous solution and dispersed by ultrasonication before adding 0.91 mg $\text{CoCl}_2 \cdot 6\text{H}_2\text{O}$ (times the fractional yield from the previous step; Alfa Aesar) to make a 3:1 total metal ratio for Pt:Co. The pH of the system is then adjusted to pH 11.0 by the addition of 1 M NaOH (J.T. Baker) to make the borohydride reduction yield smaller nanoparticles²⁰³. An aqueous sodium borohydride (NaBH_4 ; J.T. Baker) solution is then prepared in a 3:1 molar ratio of NaBH_4 to Co and is added dropwise to the former solution under vigorous stirring. For this, it was found that a 2:1 molar ratio of sodium borohydride to metal²⁰⁴ was the proper amount for the reduction of cobalt. Thus, we employed a 3:1 ratio to ensure that despite decomposition of sodium borohydride in water, the borohydride would still be present in excess for the complete reduction of the metal. The reaction was conducted for three hours, commencing at room temperature and increased to 70 °C for the last half-hour to ensure complete reduction. As before, the structures were again washed with water and ethanol and dried. With the assumption that all of the cobalt was reduced on the particles, PtNWs/C are covered in cobalt in a 3:1 Pt:Co ratio with 26.3 % wt. metal to carbon (19.7 % wt. Pt and 6.6 % wt. Co on carbon).

An agate mortar and pestle was used to gently grind the resulting PtCoNWs/C structures, and the ground structures were dispersed over the bottom of a Pyrex vessel and placed in an oven. They were then heated from room temperature to 200 °C under forming gas protection and held at

200 °C for two hours. After, they were allowed to cool under nitrogen protection before being removed from the oven and were collected by ethanol and oven dried.

Catalyst Ink and Electrode Preparation

The as-prepared catalyst powders were added to a glass vessel in a ratio of 1 mg catalyst to 1.5 mL isopropanol and were placed in an ultrasonic bath for 15 minutes. The solution was then vigorously stirred during the dropwise addition of a Nafion ionomer in isopropanol solution that was stirred for several hours, resulting in a catalyst ink comprising of 25 % wt. Nafion and 75 % wt. catalyst nanostructures. Next, a polishing kit was employed to polish glassy carbon (GC) electrodes using 0.05 μm alumina powder on a polishing pad for ten minutes. After polishing, the electrodes are placed in deionized water and sonicated for fifteen minutes with fresh deionized water added at the midpoint. A N_2 gun was then used to remove the remaining water.

Electrochemical Characterization

Prior to each application to the GC working electrode, the inks were ultrasonicated for 15 minutes to make sure a homogeneous suspension was attained (the small mass of catalyst was applied on a per-volume basis). All electrochemical scans were conducted in 120 mL of 0.5 M H_2SO_4 that had been O_2 saturated (O_2 percolation in excess of 1 hour). The catalyst addition was standardized at 2 μg (28.3 $\mu\text{g}\cdot\text{cm}^{-2}$) of total catalyst structure including carbon (based on total mass of catalyst powder per volume and volume applied assuming a homogeneous distribution of catalyst throughout the ink). The current was normalized by dividing the current by both the total catalyst mass applied and weight fraction of catalyst metal. Measurements were taken vs. a silver/silver chloride (Ag/AgCl) reference electrode. The resulting graphs were normalized versus a reversible hydrogen electrode (RHE), and a platinum wire was used for the counter electrode.

Results and Discussion

Characterization

Both a scanning electron microscope (SEM) and transmission electron microscope (TEM) were used to characterize the as-synthesized PtNWs/C and PtCoNWs/C structures as shown in Figure 5.5:

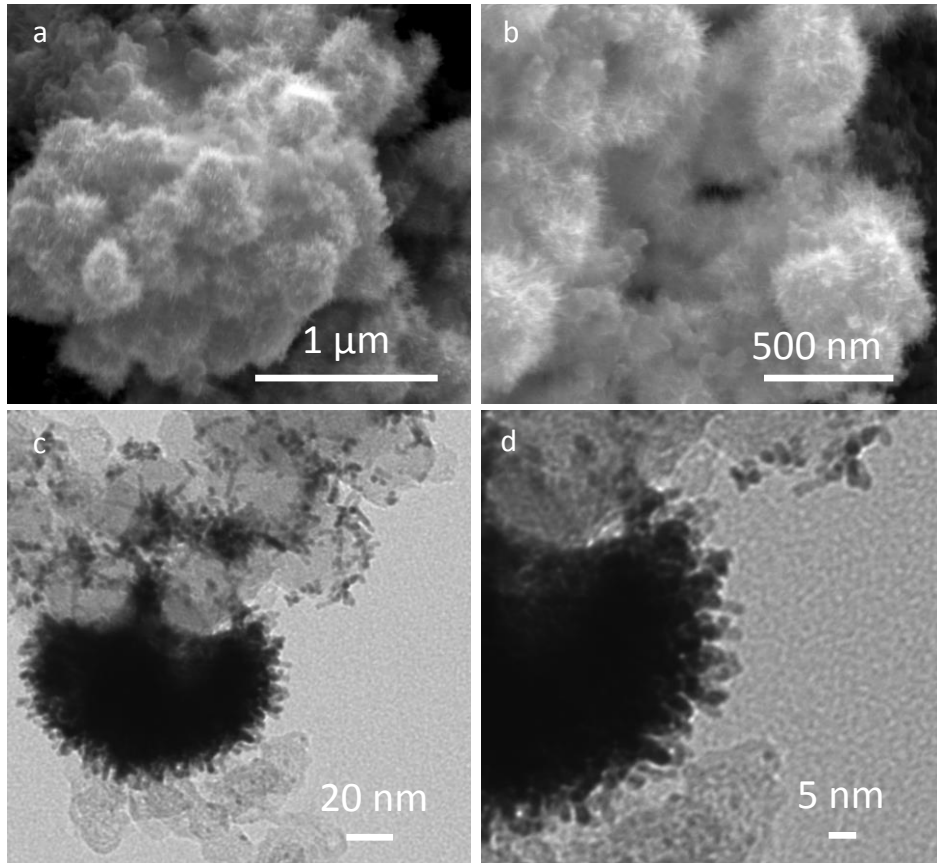


Figure 5.5. PtNWs/C (20% Pt by wt.) SEM (a,b) and TEM (c,d) images.

It has been found that the nanowires grown by this method grow along the $\langle 111 \rangle$ direction by a seeded growth mechanism²⁰⁵ and not by oriented attachment. This formation is believed to operate on the lowest energy principle, but the mechanism has not been fully elucidated²⁰⁶. 40 % PtNWs/C are shown for comparison in Figure 5.6:

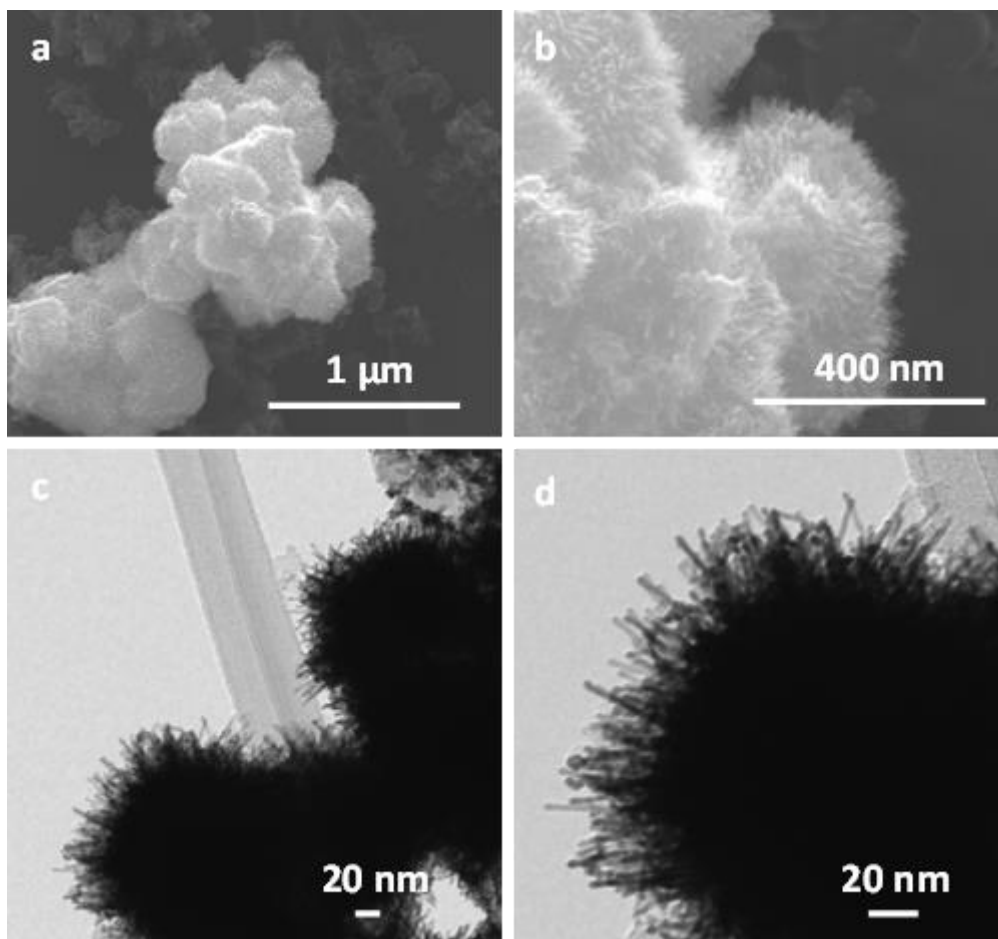


Figure 5.6. PtNWs-C (40% Pt by wt.) SEM (a,b) and TEM (c,d) images.

In these higher Pt-content structures, the increased loading is evidenced in longer nanowire formation with no noticeable change in diameter. From the TEM imaging, the 20 % wt. Pt PtNWs/C are roughly 15 nm in length and under 3 nm in diameter. The platinum to carbon ratio varies tremendously within the sample and was not as uniform as anticipated from previous studies. In this, there are regions with bare carbon, regions with nanoparticles or short nanowires, and regions with long nanowires. For this slow nucleation and growth mechanism, the reaction vessel must sit unperturbed, which we attribute to the lack of uniformity; this is likely due to carbon overlap at the bottom of the stagnant vessel, leading to sub-surface level carbon being shielded from platinum reduction (in a much shorter time frame than the reaction, carbon black precipitates

and rests at the bottom of the vessel). Thus, we employed different methods to attempt to make the nanowire growth evenly distributed on the carbon black, such as the use of surfactants, changing the precursor concentrations, and slightly agitating the system. To perturb the system in a uniform fashion, an acrylonitrile butadiene styrene (ABS) paddle was fashioned by a 3-D printer to fit securely on the shaft of a stepper motor, and the motor was programmed to turn at various rpms under both constant, slow stirring and intermittent stirring. The motor, paddle, and microcontroller platform are shown in Figure 5.7:

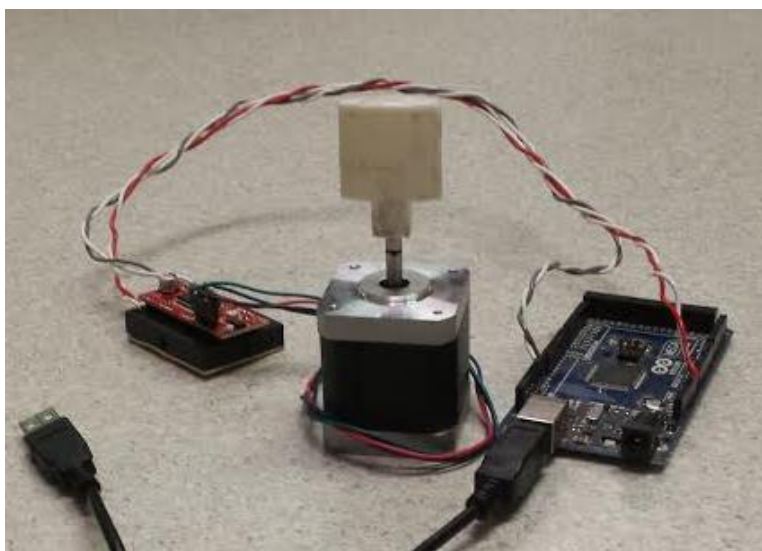
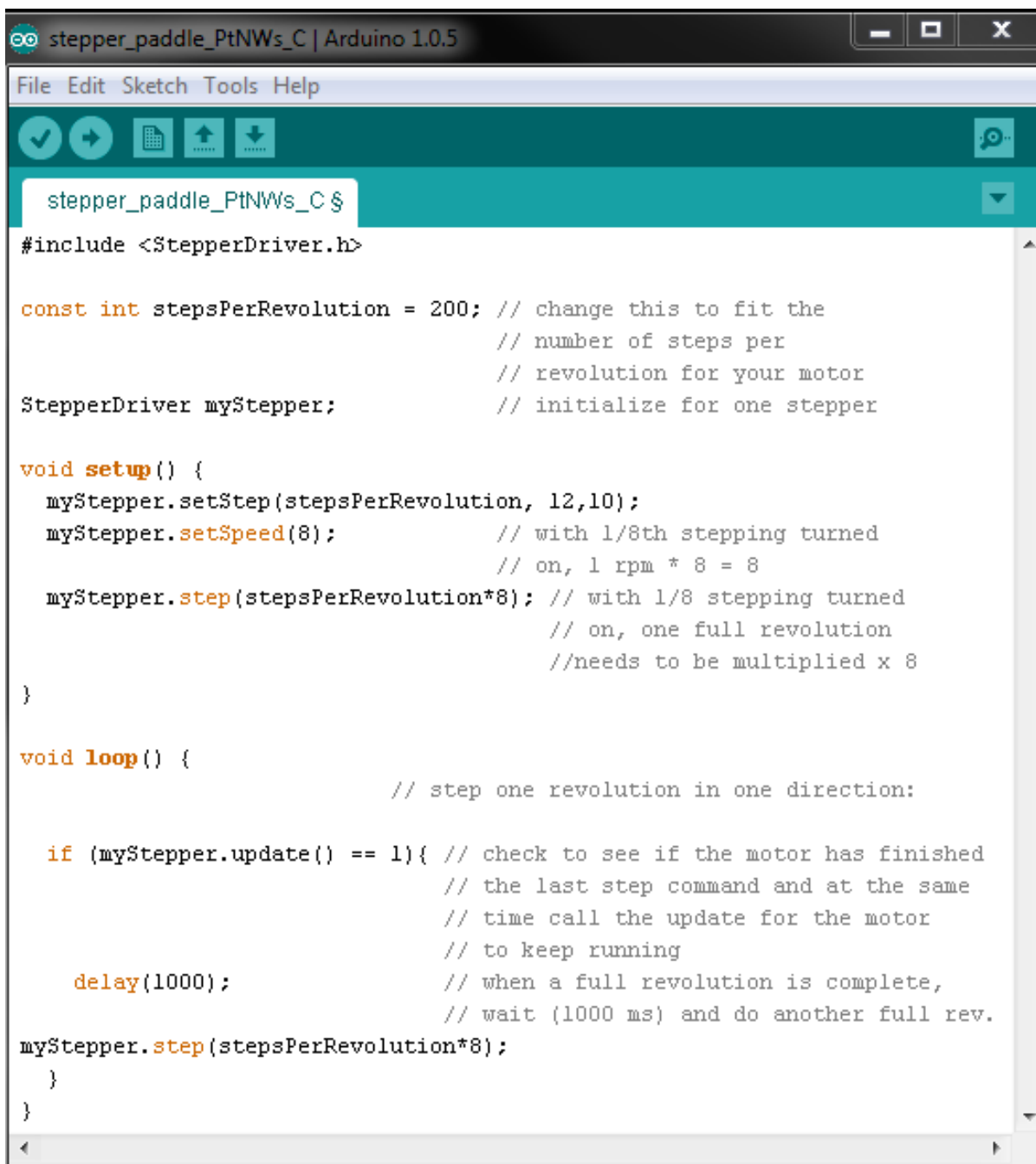


Figure 5.7. Stepper motor, acrylonitrile butadiene styrene (ABS) paddle, stepper motor driver, and microcontroller assembly.

The motors/paddles were programmed/operated according to the program below in Figure 5.8 that was modified for both different constant stir speeds and speeds and interval times between:

The image shows a screenshot of the Arduino IDE interface. The window title is "stepper_paddle_PtNWs_C | Arduino 1.0.5". The menu bar includes "File", "Edit", "Sketch", "Tools", and "Help". Below the menu bar is a toolbar with icons for a checkmark, a right arrow, a document, an upload arrow, a download arrow, and a play button. The main text area contains the following C code:

```
stepper_paddle_PtNWs_C $
#include <StepperDriver.h>

const int stepsPerRevolution = 200; // change this to fit the
                                     // number of steps per
                                     // revolution for your motor
StepperDriver myStepper;             // initialize for one stepper

void setup() {
  myStepper.setStep(stepsPerRevolution, 12,10);
  myStepper.setSpeed(8);              // with 1/8th stepping turned
                                     // on, 1 rpm * 8 = 8
  myStepper.step(stepsPerRevolution*8); // with 1/8 stepping turned
                                     // on, one full revolution
                                     //needs to be multiplied x 8
}

void loop() {
                                     // step one revolution in one direction:

  if (myStepper.update() == 1){ // check to see if the motor has finished
                                 // the last step command and at the same
                                 // time call the update for the motor
                                 // to keep running
    delay(1000);                 // when a full revolution is complete,
                                 // wait (1000 ms) and do another full rev.
  myStepper.step(stepsPerRevolution*8);
  }
}
```

Figure 5.8. Arduino program (written in C programming language) to control the stepper motor speed and/or pause between rotations.

The effects of stirring, however, seemed negligible through SEM and electrochemical analysis. Similarly, the effects from using surfactants and adjusting precursor concentrations also proved negligible or made the structures have less uniform nanowires and lower electrochemical

activity. Thus, we proceeded to add cobalt to the structures obtained by the previous method without uniformity optimization. Similarly, images are shown for PtCoNWs/C in Figure 5.9:

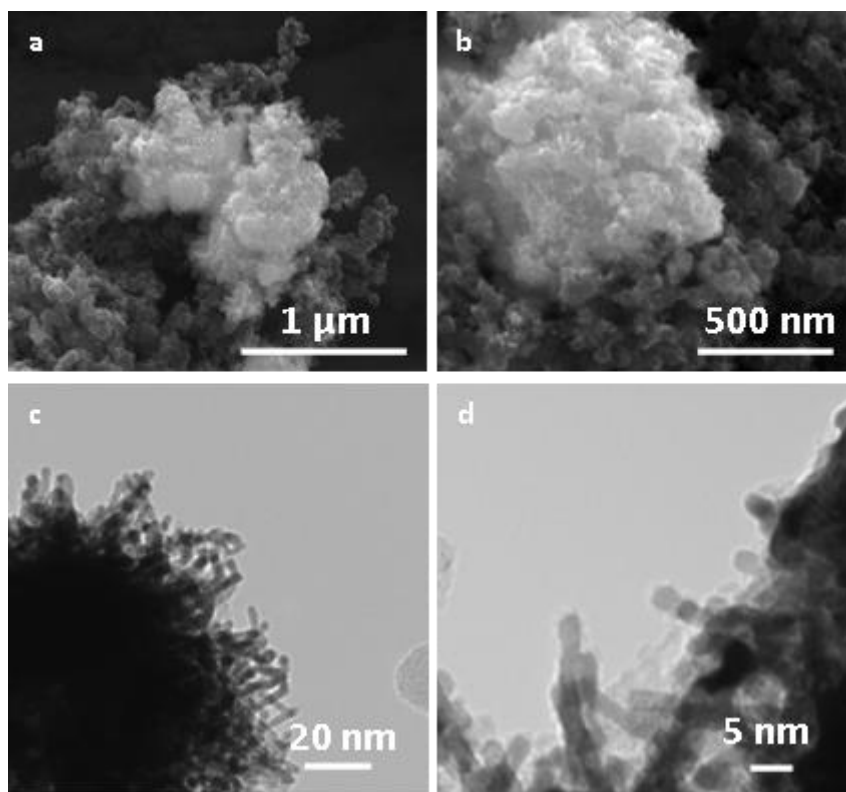


Figure 5.9. PtCoNWs/C SEM (a,b) and TEM (c,d) images.

Here, it is observed that the morphology of the nanowires is preserved in the bi-metallic structures, yet the nanowires were slightly larger in diameter due to the incorporation of Co into Pt. Energy dispersive x-ray spectroscopy was also used to confirm Co exists in the structures (data not shown). The relative amount of Co is less in regions of dense Pt nanowire formation, and the relative amount of Co is more in the regions with less platinum. Thus, much of the sample possesses ratios of different proportions than the optimal, highly active 3:1 Pt:Co structures found in literature. On account of Co not being stable in highly acidic environments (such as PEMFC cathodes), forming an alloy with platinum is crucial to prevent Co dissolution. To determine if alloying of Pt and Co exists or whether they remain independent, x-ray diffraction (XRD) studies

could be employed, but this technique requires a much larger sample size than was synthesized. XRD was not used in this study due to a scaled-up sample not accurately representing the small batches utilized for the rest of the analysis (the same electrochemical activity was not observed when the structures were synthesized in larger quantities). Alloying can be observed as an XRD peak shift, but this likely would not be observed due to literature reporting alloying at temperatures of 700 °C¹⁹⁸ or 900 °C²⁰⁷, temperatures that could not be withstood by the temperature sensitive nanowires. Also, from the TEM images of the PtCoNWs/C, it can be observed that the nanowires began to curl under the thermal treatment and are not as straight as they were before the treatment.

Electrochemical Analysis

As mentioned, modified electrodes were prepared using inks generated from both the PtNWs/C and PtCoNWs/C, as well as the commercial XC-72 catalyst (20 wt. % Pt:C) for comparison to study their mass-specific activity toward the oxygen reduction reaction. For this, all electrochemical scans were conducted at 20 mV·s⁻¹ in a potential window of 0.9 to 0 V (v. Ag/AgCl) in O₂ saturated 0.5 M H₂SO₄. For an initial comparison of the structure activity, cyclic voltammetry (CV) was used, and an overlay of the CVs (total metal basis normalized) for PtNWs/C, PtCoNWs/C, and XC-72 Pt/C are shown in Figure 5.10:

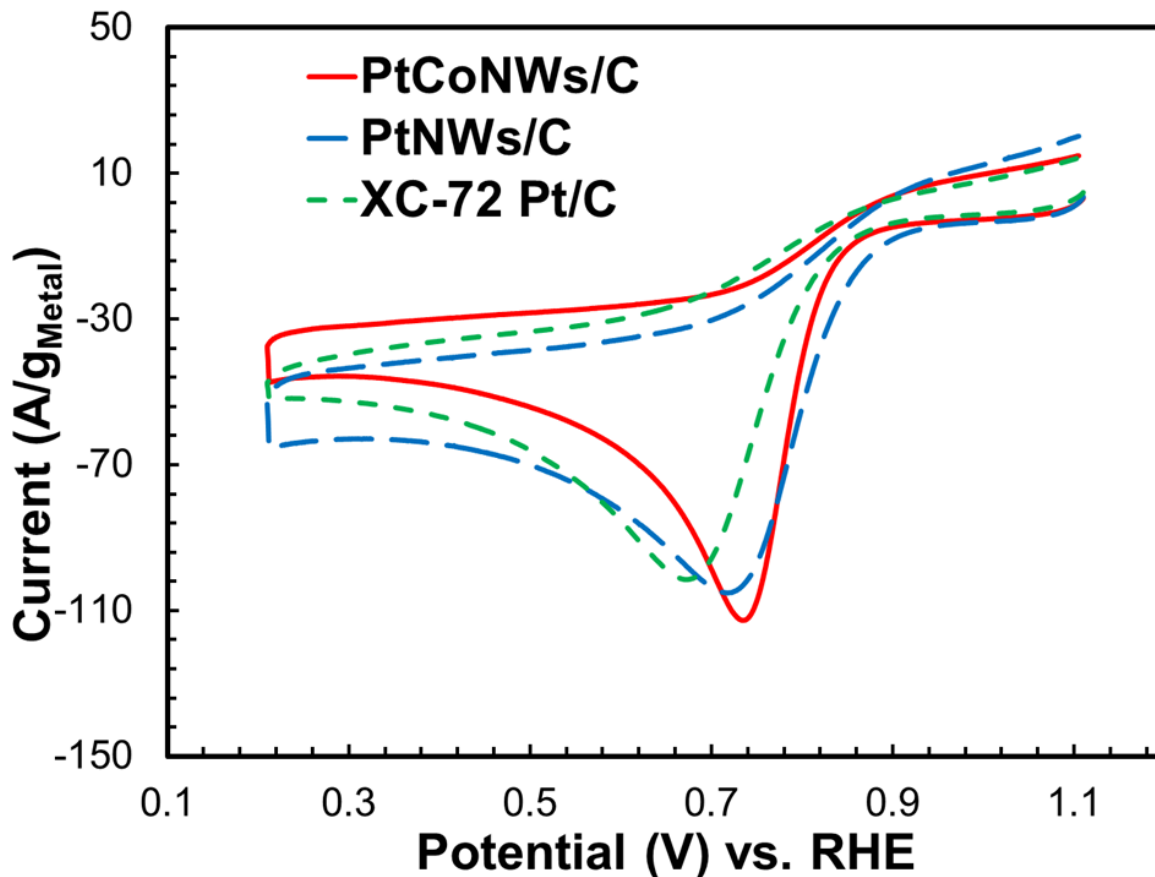


Figure 5.10. Cyclic Voltammograms: glassy carbon modified with PtNWs/C, PtCoNWs/C, and Standard XC-72 Pt/C, in O₂ saturated 0.5 M H₂SO₄ at a scan rate of 20 mV·s⁻¹ normalized based on a total metal mass basis.

From this scan, it is shown that the PtNWs/C and PtCoNWs/C both demonstrate a higher normalized peak current than the XC-72 Pt/C regarding the ORR. There is also a 40 mV and 30 mV higher (more positive) onset potential for the PtNWs/C and PtCoNWs/C, respectively towards the ORR than the XC-72 Pt/C. This means the nanowire structures take less overpotential (less voltage difference from the redox potential of water ~1.23 V v. RHE), or less driving energy, for oxygen reduction, typically signifying a better catalyst; however, the PtCoNWs/C require slightly more overpotential to initiate the reaction than do the PtNWs/C, which is believed to be due to the surface area loss on account of metal agglomeration during annealing process of the PtCoNW/C.

The PtCoNWs/C also exhibit a steeper ORR slope than the other samples, proving it takes less overpotential per current increase.

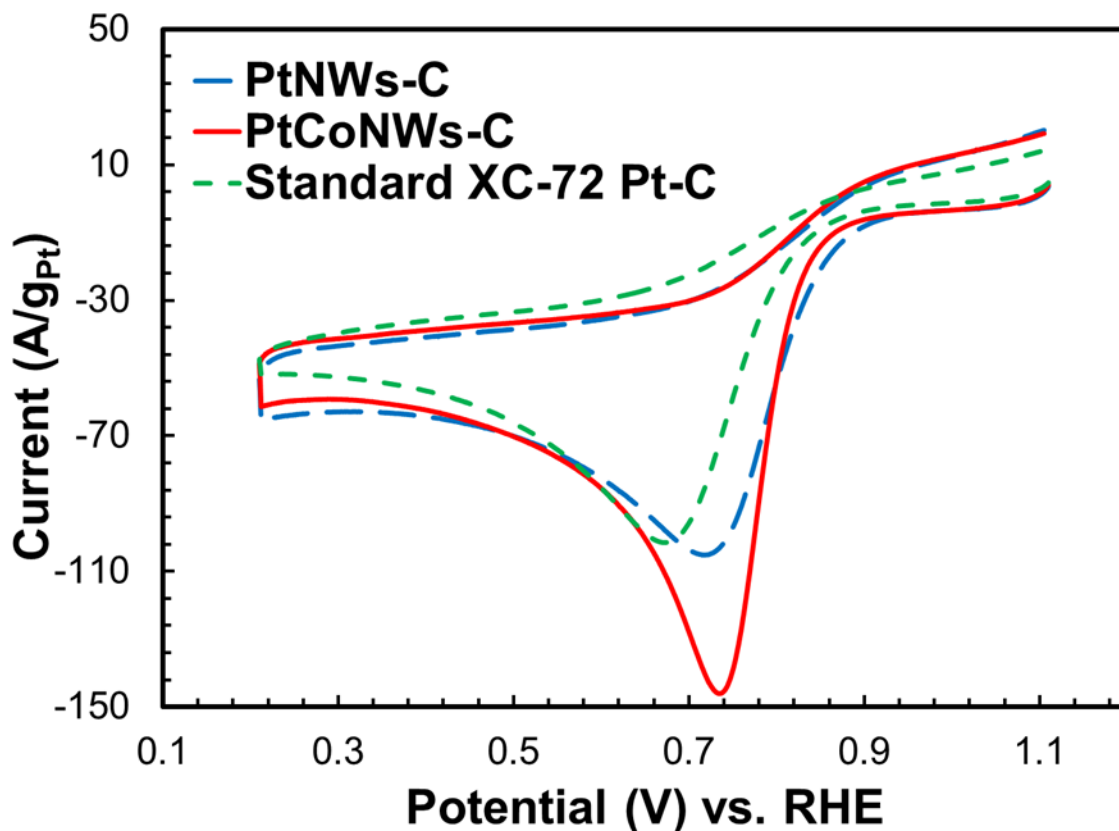


Figure 5.11. Cyclic Voltammograms: glassy carbon modified with PtNWs-C, PtCoNWs-C, and Standard XC-72 Pt-C, in O_2 saturated $0.5\text{ M H}_2\text{SO}_4$ at a scan rate of $20\text{ mV}\cdot\text{s}^{-1}$ normalized based on a Pt mass basis.

Figure 5.11 does not factor in the extra Co in the PtCoNWs/C (so it has extra transition metal catalyst material), but it shows the difference between the samples based on the amount of extremely expensive platinum used.

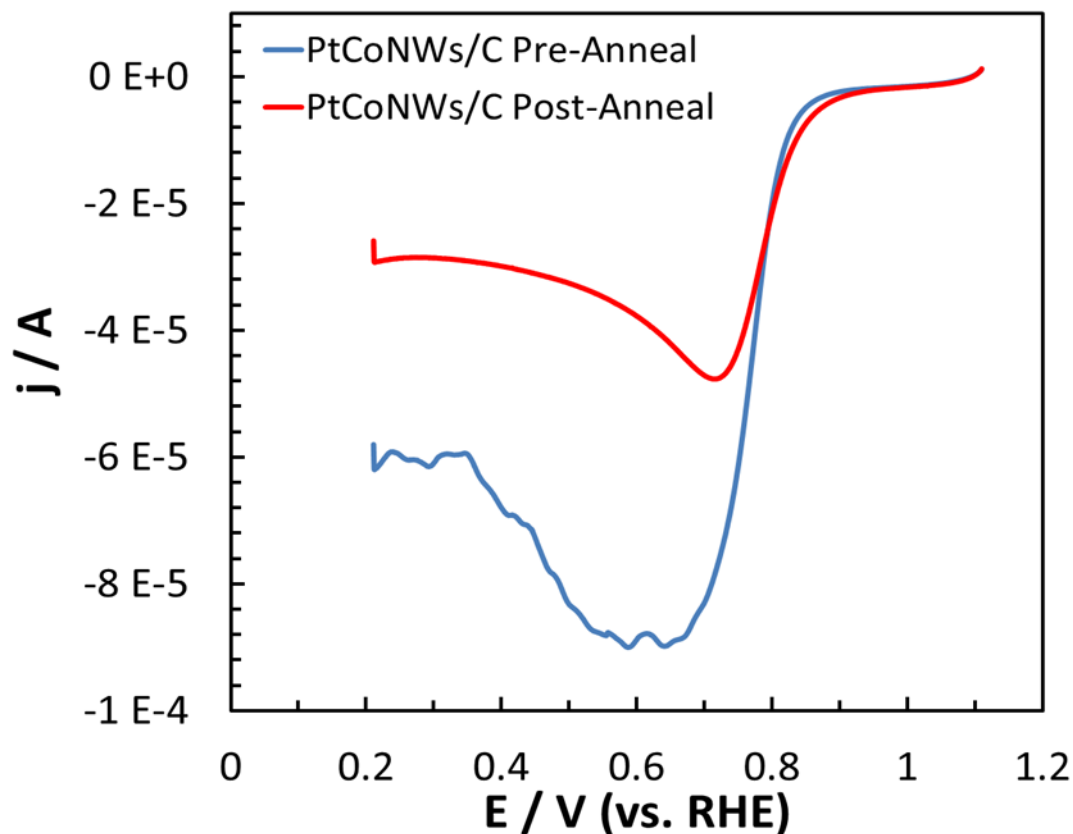


Figure 5.12. Linear Sweep Voltammograms: glassy carbon modified with 3:2 Pt:Co PtCoNWs/C, Pre- and Post-Anneal in O_2 saturated 0.5 M H_2SO_4 at a scan rate of $20 \text{ mV}\cdot\text{s}^{-1}$ of normalized catalyst loading.

These structures used a slightly higher ratio of Co to Pt 2:3, opposed to the usual 1:3 to accentuate the difference in activity pre- and post-annealing the PtCoNWs/C structures. Here, it shows that pre-annealing, there is a substantially higher peak current and more steep ORR slope, yet the pre-annealed structures appear to be unstable due to the noisy nature of the scan. It is believed that the decrease in the ORR slope and peak current (of the post-annealed structures) is due to annealing decreasing the surface area from both cobalt particle merging/agglomeration and cobalt diffusing into the Pt nanowires.

To better understand the electrokinetics of the structures in the absence of diffusion, linear sweep voltammetry (LSV) was performed using a rotating ring-disk electrode (RRDE). Here, a ring potential was applied at 1.11 V v. RHE (0.9 V v. Ag/AgCl) to detect hydrogen peroxide formation (an undesired intermediate product that slows the kinetics of the ORR). Figure 5.13 shows the LSVs (monitoring ring and disk currents versus potential) at increasing rotational speeds for all of the structures shown in Figure 5.13:

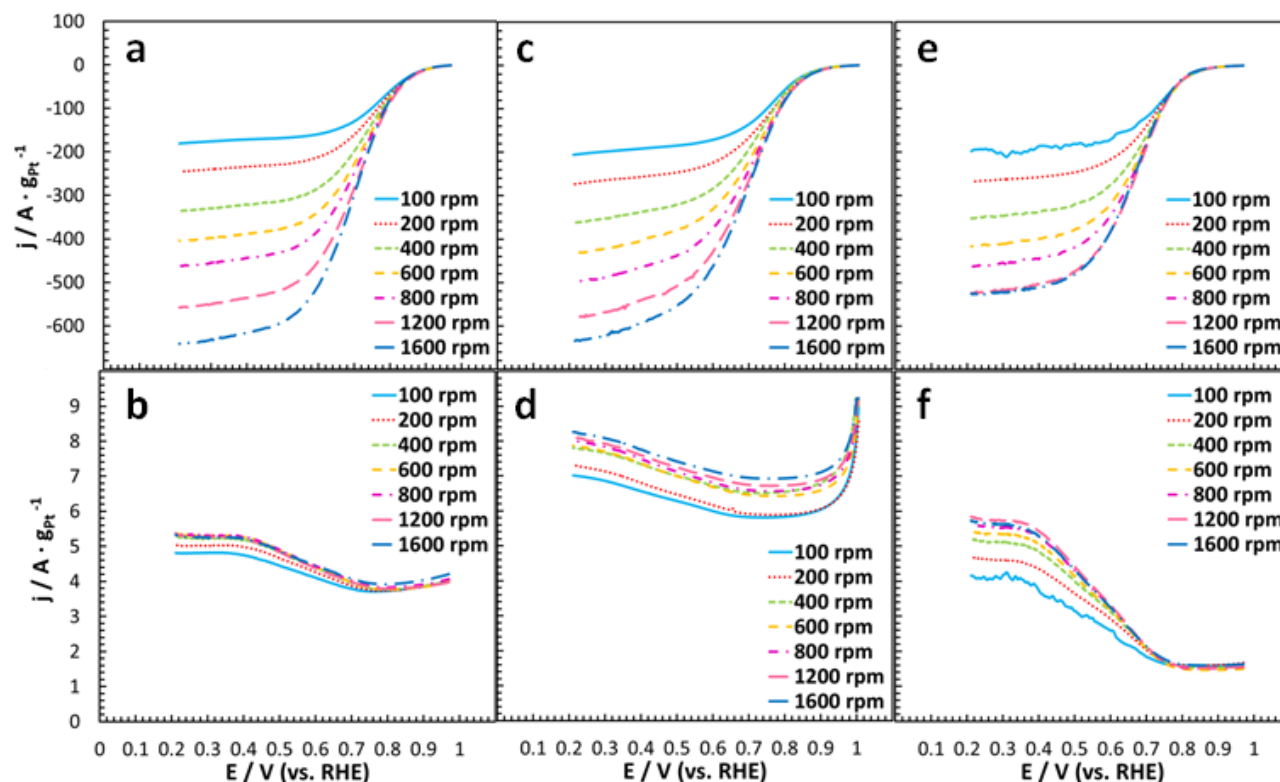


Figure 5.13. Disk and ring-currents for PtNWs/C (a,b), PtCoNWs/C (c,d), and Standard XC-72 Pt/C (e,f) at increasing rpms at a scan rate of $20 \text{ mV} \cdot \text{s}^{-1}$ in $0.5 \text{ M H}_2\text{SO}_4$.

Here, the graphs are normalized to the Pt mass-specific current to compare the activity based on the amount of precious metal used. Here, it is believed that the total metal comparison is not appropriate for the PtCoNWs/C due to not all of the nominal amount of Co reduced on the structures diffusing into the Pt, causing it to be left vulnerable to break-down and dissolution in

the harsh acidic environment. As shown in the figure, the PtCoNWs/C have the highest limiting current at the rotational speeds, followed by the PtNWs/C and then the XC-72 Pt/C commercial catalyst. The ring current is lower than the commercial catalyst for the PtNWs/C at high rotational speeds (desirable), yet there is a higher ring current for the PtCoNWs/C, which was expected due to its higher disk current. The sub-optimal diffusion at the disk could have caused higher ring current for the PtCoNWs/C (bent/agglomerated nanowire structure), resulting in O₂ reduction at the ring.

The Tafel and Levich plots are shown in Figure 5.14. For a 4-electron process, the theoretical Tafel slope is 14.75 mV (= 59 mV / n, with n equaling 4) per decade (ten-fold gain) of kinetic current increase. The slope will always be above this value, but the closer they are to the theoretical value, the better the electrocatalyst for the ORR. The Tafel plot was generated from the 1200 rpm disk LSVs (at 20 mV beyond each structure's onset potential), and it was calculated that the Tafel slopes are roughly 33 and 37 mV/decade for the PtNWs/C and XC-72 Pt/C, respectively, while the PtCoNWs/C show increased activity at approximately 24 mV/decade. This difference is easily seen in the Tafel plot, where the PtCoNWs/C have the lowest slope at low current density. Then, at high current density, the commercial catalyst has the lowest slope, followed by the PtNWs/C and then the PtCoNWs/C. It is believed that this is due to the commercial catalyst having the highest surface area (spheres have more surface area per volume than rods of the same diameter), followed by the PtNWs/C and then PtCoNWs/C. Thus, the higher surface area catalyst has the ability to interact with more O₂ at higher current density.

The Levich plot corresponds to Equation 9 (shown again for easy reference) and is generated by plotting the limiting current v. rotational speed.

$$I_L = 0.620nFAD^{\frac{2}{3}}\omega^{\frac{1}{2}}\nu^{-\frac{1}{6}}C \quad [5.11]$$

Where I_L , the limiting current, is proportional to the number of electrons transferred per reaction, n , Faradays constant, F ($96,485 \text{ C} \cdot \text{mol}^{-1}$), the geometrical area of the unmodified electrode, A , the diffusion coefficient of oxygen, D_{O_2} ($1.61 \times 10^{-5} \text{ cm}^2 \cdot \text{s}^{-1}$)²⁰⁸, the kinematic viscosity of the fluid, ν , the concentration of dissolved oxygen in the solution, C_{O_2} ($1.15 \times 10^{-6} \text{ mol} \cdot \text{cm}^{-3}$)²⁰⁸, and the angular velocity, ω (in $\text{rad} \cdot \text{s}^{-1}$).

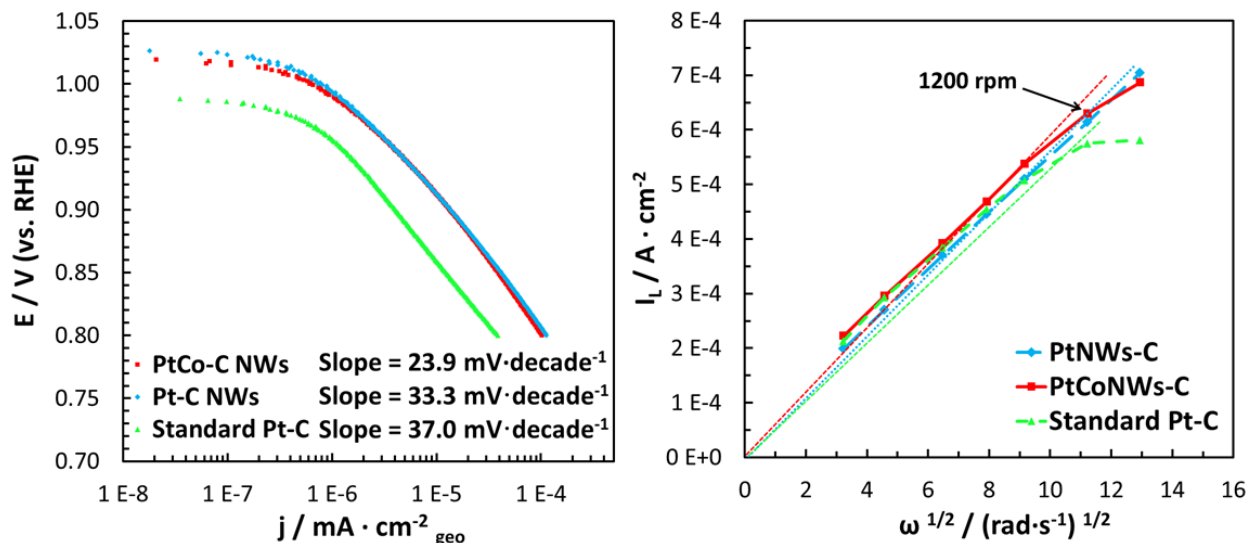


Figure 5.14. Tafel plot (at 1200 rpm) (a) and Levich plot (b) for the structures generated from the data shown in Figure 5.13.

It can be observed that the PtNWs/C structures have the largest linear Levich region, believed to be due to facile diffusion of dioxygen to and from the electrocatalytic sites than for XC-72 Pt/C, which possesses nanoparticles that do not provide for these nice diffusion channels as hypothesized previously for the PtNWs/C¹⁹¹. The PtCoNWs/C should experience the same benefit of diffusion enhancement with respect to the commercial catalyst, but it is not seen as definitively, likely due to nanowire deformation (bending) and Pt-Co agglomeration during annealing. As seen in the PtCoNWs/C TEM images in Figure 5.9 c and 5.9 d, the nanowires are slightly curled, which is believed to decrease the diffusion efficiency to and from the catalytic sites for the analyte.

Koutecky-Levich (K-L) plots have been generated using data from the linear Levich region, where inverse current density at 0.25, 0.35, 0.45, and 0.55 V is plotted versus the inverse square root of the angular velocity in accordance with the K-L equation:

$$\frac{1}{j} = \frac{1}{j_k} + \frac{1}{\beta\omega^{1/2}} \quad [5.12]$$

In this equation, j_k is the kinetic current, and $\beta\omega^{1/2}$ is the limiting current from the Levich equation, where β is equal to all of the coefficients listed before $\omega^{1/2}$, as previously defined. These plots resulted in straight lines, and the β values (inversely proportional to the slope) were determined from the average of the four slopes of these lines for each catalyst. From this, it was observed that the PtCoNWs/C and XC-72 Pt/C yielded a near four-electron process, where the PtNWs/C showed a number of electrons approximately halfway between three and four.

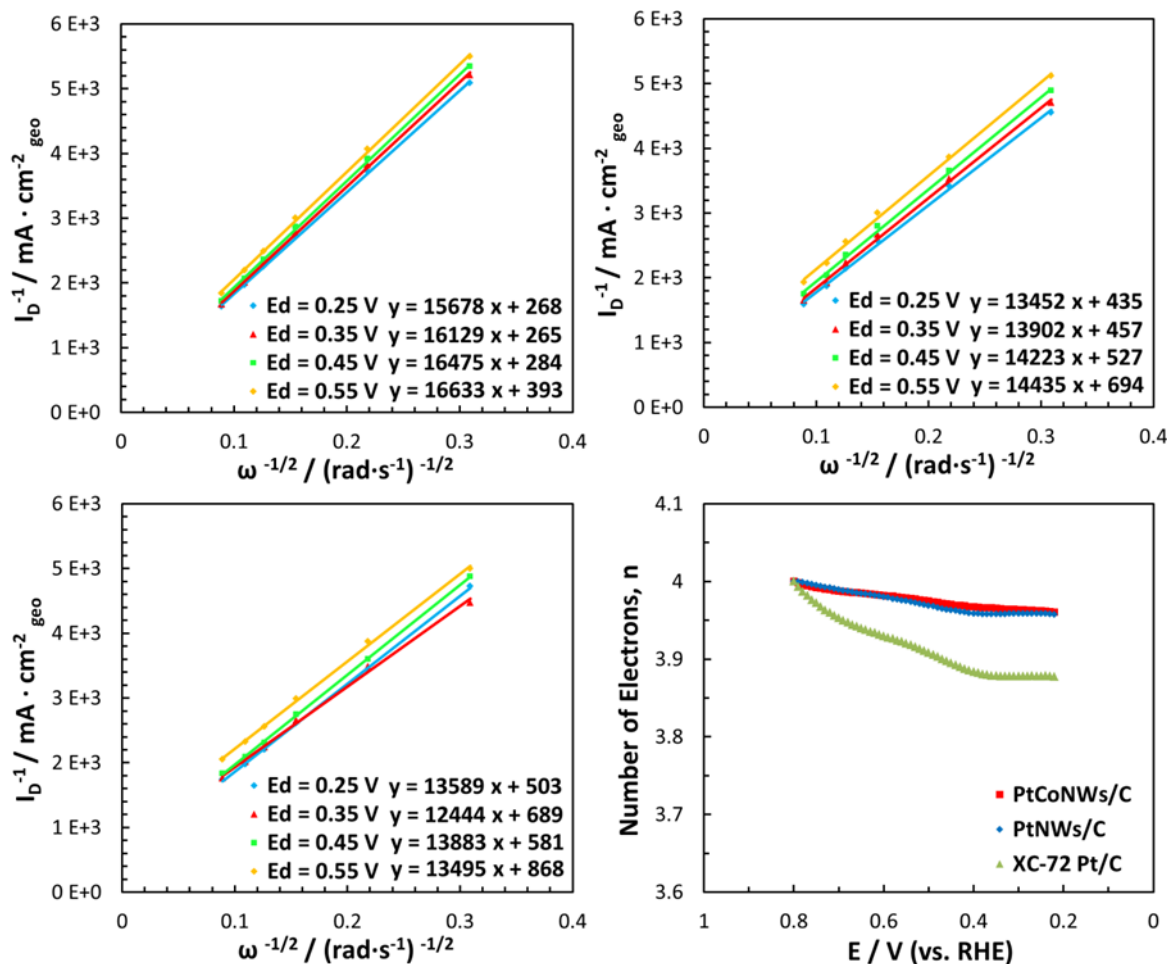


Figure 5.15. Koutecky-Levich plots for the PtNWs/C (a), PtCoNWs/C (b), and XC-72 Pt/C (c), and Number of Electrons plot at 1200 rpm (d), all from the data in Figure 5.13.

For comparison of the electrokinetics at various potentials, a plot of number of electrons transferred v. disk potential was formed according to the equation:

$$n = \frac{1}{1 + \frac{I_R}{NI_D}} \quad [5.13]$$

In this equation, I_R and I_D are the ring and disk currents, respectively, and N is a geometric parameter determined to be 0.256 by the RRDE developers. The collection efficiency, N , refers to the fraction of H_2O_2 that is collected at the ring after being formed at the disk. From this number of electrons plot, it shows the PtNWs/C and PtCoNWs/C have a nearly 4-electron process

throughout the potential region, where the XC-72 Pt/C begins at 4 electrons and drops to just below 3.9-electrons through the high current density or limiting current region. Some discrepancy is observed regarding the number of electrons calculated from the number of electrons plot and the K-L plot, which could be due to noise and/or the chosen potentials for the K-L analysis.

Conclusions

PtCoNWs/C and PtNWs/C both demonstrate an increase in the mass-specific current toward the ORR, and they feature more positive onset potentials for the ORR, indicative of less overpotential with respect to the commercial catalyst. The PtNWs/C exhibit a slightly lower Tafel slope than the commercial catalyst, whereas the PtCoNWs/C feature a substantially lower Tafel slope than both of the other structures. PtCoNWs/C also conduct a near four-electron kinetics process, demonstrating their single-step reduction of oxygen to water with no peroxide intermediate and high ORR activity. This was expected, since literature shows that platinum-cobalt alloys covered in a Pt-skin have higher affinity than Pt for the ORR. This is the case if a thin-layer of platinum diffused to the surface during annealing, which yields the highly active Pt-skin surrounding 3:1 Pt:Co; however, the structures synthesized in this work do not approach the results attained for Pt₃Ni and Pt₃Co surrounded by a Pt skin. This is believed to be due partly to a sub-optimal ratio of Pt to Co in the nanowires, due to the cobalt being reduced independently after the PtNWs, affording Co to be reduced on both the Pt nanowires and the carbon substrate (potentially making less Co be reduced in the nanowires and a sub-optimal ratio).

However, the higher surface area of the commercial catalyst often exhibits higher activity at high current density based on more analyte being able to come in contact with the surface, and the more active surfaces of the Pt-Co nanowires should likely be higher at low current density and

the suffer due to lower surface area at high current density, but the heightened catalysis must outweigh the surface area.

Also, the annealing process applied in this work featured a much lower temperature due to nanowire destruction at high temperature. True alloying typically occurs at 900 °C²⁰⁹, which makes it highly likely that Co only experienced partial diffusion into the Pt at the surface of the nanowires. Future work regarding this project includes optimizing the procedure to produce large-scale batches of the same or similar electrochemical activity, optimizing the annealing method using lower temperatures and longer times to avoid nanowire deformation, as well as to test the durability/stability of the PtCoNWs/C via an accelerated durability test.

APPENDIX

Appendix Figures

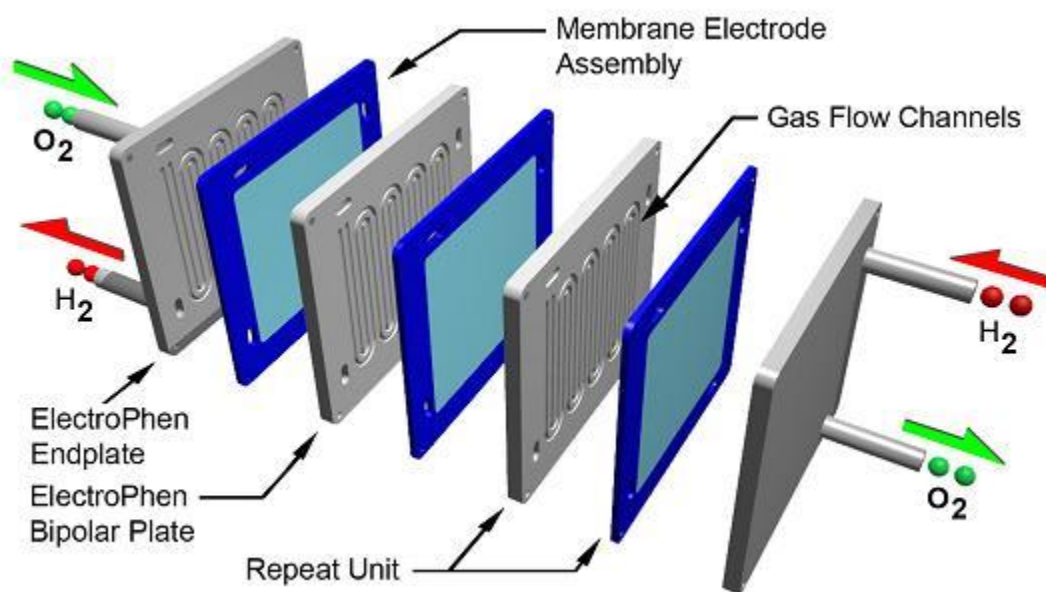


Figure A 5.1. Schematic of a small fuel cell stack utilizing a cheap and lightweight ElectroPhen™ material showing hydrogen and oxygen gas flow through endplates and bipolar plates (with serpentine gas flow channels) and membrane electrode assemblies.¹⁷⁷

REFERENCES

1. P.J. Shields, Bragg's Law and Diffraction: How waves reveal the atomic structure of crystals. *What is Bragg's Law and Why is it Important?* Oct. 11, 2004, (May 7, 2015), <http://skuld.bmsc.washington.edu/~merritt/bc530/bragg/>.
2. M. Fang, X-ray in Characterization Techniques. *Science 2.0* June 28, 2010, (June 5, 2015), http://www.science20.com/mei/blog/xray_characterization_techniques.
3. X-ray Diffraction (XRD). <http://web.pdx.edu/~pmoeck/phy381/Topic5a-XRD.pdf> March 31, 2004, (June 27, 2015).
4. S. Swapp, Scanning Electron Microscopy (SEM). *Geochemical Instrumentation and Analysis* (December 12, 2014), http://serc.carleton.edu/research_education/geochemsheets/techniques/SEM.html.
5. J. Goldstein, D.E. Newbury, P. Echlin, D.C. Joy, A.D. Romig, C.E. Lyman, C. Fiori, and E. Lifshin, Scanning Electron Microscopy. *Scanning Electron Microscopy and X-Ray Microanalysis: A Text for Biologists, 2nd Ed.* 1992, 86-93.
6. Introduction to Electron Microscopes: Transmission Electron Microscope (TEM), Electron Gun. *University of Liverpool* 1997-2007, <http://www.materials.ac.uk/elearning/matter/IntroductionToElectronMicroscopes/TEM/electron-gun.html>.
7. Introduction to Electron Microscopes: Transmission Electron Microscope (TEM), Camera and Display. *University of Liverpool* 1997-2007, matter (November 25, 2014), <http://www.materials.ac.uk/elearning/matter/IntroductionToElectronMicroscopes/TEM/camera-and-display.html>.
8. C. Woodford, Explain That Stuff! Electron Microscopes. 2010, March 3, 2015, www.explainthatstuff.com/electronmicroscopes.html.
9. J.E. Bonevich, Measuring the Size of Nanoparticles Using Transmission Electron Microscopy (TEM). *NIST-NCL Joint Assay Protocol, PCC-7* 2010, Version 1.1 (February 17, 2015), http://ncl.cancer.gov/NCL_Method_PCC-7.pdf.
10. W. Mai, Fundamental Theory of Atomic Force Microscopy. *Zhong L. Wang's Nano Researchs* (April 24, 2015), <http://www.nanoscience.gatech.edu/zlwang/research/afm.html>.
11. P. Eaton, AFM: Beginner's Guide. *AFMHELP.COM* 2015, July 10, 2015, http://www.afmhelp.com/index.php?option=com_content&view=article&id=51&Itemid=57.
12. T. Pike, L. Fielder, and M. Anderson, Combined Raman-Atomic Force Microscope. *Research: Optical and Semiconductor Devices* 2015, June 27, 2015, <http://www3.imperial.ac.uk/opticalandsemidev/microelectronics/ramanafm>.
13. What is Raman Spectroscopy. *InPhotonics, Inc.* 2012, January 23, 2015, <http://www.inphotonics.com/raman.htm>.

14. N. Birkner and Q. Wang, How an FTIR Spectrometer Operates. *UC Davis Chem Wiki July 7, 2015*, http://chemwiki.ucdavis.edu/Physical_Chemistry/Spectroscopy/Vibrational_Spectroscopy/Infrared_Spectroscopy/How_an_FTIR_Spectrometer_Operates.
15. K. Gable, FTIR Spectroscopy. *Oregon State 2013, December 13, 2015*, <http://chemistry.oregonstate.edu/courses/ch361-464/ch362/irinstrs.htm>.
16. Introduction to Fourier Transform Infrared Spectrometry. *Thermo Nicolet 2001, October 21, 2014*, <http://mmrc.caltech.edu/FTIR/FTIRintro.pdf>.
17. B. Hafner, Energy Dispersive Spectroscopy on the SEM: A Primer. *University of Minnesota 2013, June 6, 2015*, http://www.charfac.umn.edu/instruments/eds_on_sem_primer.pdf.
18. V.A. Sole and E. Papillon, PyMCA-X-Ray Spectrum Analysis in Python. *European Synchrotron Radiation Facility (July 7, 2015)*, <http://www.esrf.eu/computing/bliss/downloads/pymca/PyMCA.pdf>.
19. S. Wang, D. Y., and L. Dai, Polyelectrolyte Functionalized Carbon Nanotubes as Efficient Metal-free Electrocatalysts for Oxygen Reduction. *Journal of the American Chemical Society 2011, 133*, 5182-5185.
20. N. I. Kovtyukhova, P. O., B. R. Martin, T. Mallouk, S. Chizhik, E. Buzaneva, and A. Gorchinsky, Layer-by-Layer Assembly of Ultrathin Composite Films from Micron-Sized Graphite Oxide Sheets And Polycations. *Chem. Mater. 1999, 11*, 771-778.
21. Li, X.; Cai, W.; An, J.; Kim, S.; Nah, J.; Yang, D.; Piner, R.; Velamakanni, A.; Jung, I.; Tutuc, E.; Banerjee, S. K.; Colombo, L.; Ruoff, R. S., Large-area synthesis of high-quality and uniform graphene films on copper foils. *Science 2009, 324* (5932), 1312-4.
22. (a) Yamada, T.; Kim, J.; Ishihara, M.; Hasegawa, M., Low-temperature graphene synthesis using microwave plasma CVD. *Journal of Physics D: Applied Physics 2013, 46* (6), 063001; (b) Kobayashi, T.; Bando, M.; Kimura, N.; Shimizu, K.; Kadono, K.; Umezumi, N.; Miyahara, K.; Hayazaki, S.; Nagai, S.; Mizuguchi, Y.; Murakami, Y.; Hobar, D., Production of a 100-m-long high-quality graphene transparent conductive film by roll-to-roll chemical vapor deposition and transfer process. *Applied Physics Letters 2013, 102* (2), 023112.
23. X. Li, G. Zhang, X. Bai, X. Sun, S. Wang, E. Wang, and H. Dai, Highly conducting graphene sheets and Langmuir-Blodgett films. *Nature nanotechnology 2008, 3*, 538-542.
24. W. S. Hummers, R. E. O., Preparation of Graphitic Oxide. *J. Am. Chem. Soc. 1958, 80*, 1339.
25. D. Dikin, S. S., E. Zimney, R. Piner, G. Dommett, G. Evmenenko, S. Nguyen and R. S. Ruoff, Preparation and characterization of graphene oxide paper. *Nature Letters 2007, 448*, 457-460.
26. D. C. Marcano, D. V. K., J. Berlin, J. Tour, Improved Synthesis of Graphene Oxide *ACS Nano 2010, 4* (8), 4806-4814.
27. Wei, Z.; Wang, D.; Kim, S.; Kim, S. Y.; Hu, Y.; Yakes, M. K.; Laracuente, A. R.; Dai, Z.; Marder, S. R.; Berger, C.; King, W. P.; de Heer, W. A.; Sheehan, P. E.; Riedo, E., Nanoscale tunable reduction of graphene oxide for graphene electronics. *Science 2010, 328* (5984), 1373-6.
28. W. Chen, L. Y., P. Bangal, Preparation of graphene by the rapid and mild thermal reduction of graphene oxide induced by microwaves. *Carbon 2010, 48*, 1146-1152.
29. S. Stankovich, D. D., R. Piner, K. Kohlhaas, A. Kleinhammes, Y. Jia, Y. Wu, Synthesis of graphene-based nanosheets via chemical reduction of exfoliated graphite oxide. *Carbon 2007, 45*, 1558-1565.
30. Li, D.; Muller, M. B.; Gilje, S.; Kaner, R. B.; Wallace, G. G., Processable aqueous dispersions of graphene nanosheets. *Nature nanotechnology 2008, 3* (2), 101-5.

31. W. Chen, L. Y., P.R. Bangal, Chemical Reduction of Graphene Oxide to Graphene by Sulfur-Containing Compounds. *J. Phys. Chem. C* **2010**, *114*, 19885-19890.
32. Chavez-Valdez, A.; Shaffer, M. S.; Boccaccini, A. R., Applications of graphene electrophoretic deposition. A review. *The journal of physical chemistry. B* **2013**, *117* (6), 1502-15.
33. Yang, J.; Gunasekaran, S., Electrochemically reduced graphene oxide sheets for use in high performance supercapacitors. *Carbon* **2013**, *51*, 36-44.
34. Lin, J. Y.; Chan, C. Y.; Chou, S. W., Electrophoretic deposition of transparent MoS₂-graphene nanosheet composite films as counter electrodes in dye-sensitized solar cells. *Chemical communications* **2013**, *49* (14), 1440-2.
35. Zhitomirsky, Y. S. a. I., Electrophoretic Nanotechnology of Composite Electrodes for Electrochemical Supercapacitors. *J. Phys. Chem. B* **2013**, *117*, 1563-1570.
36. Zhang, H.; Zhang, X.; Zhang, D.; Sun, X.; Lin, H.; Wang, C.; Ma, Y., One-step electrophoretic deposition of reduced graphene oxide and Ni(OH)₂ composite films for controlled syntheses supercapacitor electrodes. *The journal of physical chemistry. B* **2013**, *117* (6), 1616-27.
37. Zhu, G.; Pan, L.; Sun, H.; Liu, X.; Lv, T.; Lu, T.; Yang, J.; Sun, Z., Electrophoretic deposition of a reduced graphene-Au nanoparticle composite film as counter electrode for CdS quantum dot-sensitized solar cells. *Chemphyschem: a European journal of chemical physics and physical chemistry* **2012**, *13* (3), 769-73.
38. Wu, Z.-S.; Pei, S.; Ren, W.; Tang, D.; Gao, L.; Liu, B.; Li, F.; Liu, C.; Cheng, H.-M., Field Emission of Single-Layer Graphene Films Prepared by Electrophoretic Deposition. *Advanced Materials* **2009**, *21* (17), 1756-1760.
39. V. Strong, S. D., M. F. El-Kady, A. Lech, Y. Wang, B. H. Weiller and R. B. Kaner, Patterning and Electronic Tuning of Laser Scribed Graphene for Flexible All-Carbon Devices. *ACS Nano* **2012**, *6* (2), 1395-1403.
40. Prezioso, S.; Perrozzi, F.; Donarelli, M.; Bisti, F.; Santucci, S.; Palladino, L.; Nardone, M.; Treossi, E.; Palermo, V.; Ottaviano, L., Large area extreme-UV lithography of graphene oxide via spatially resolved photoreduction. *Langmuir: the ACS journal of surfaces and colloids* **2012**, *28* (12), 5489-95.
41. G. Williams, B. S., and P. V. Kamat, TiO₂-Graphene Nanocomposites. UV-Assisted Photocatalytic Reduction of Graphene Oxide. *ACS Nano* **2008**, *2* (7), 1487-1491.
42. Gengler, R. Y.; Badali, D. S.; Zhang, D.; Dimos, K.; Spyrou, K.; Gournis, D.; Miller, R. J., Revealing the ultrafast process behind the photoreduction of graphene oxide. *Nature communications* **2013**, *4*, 2560.
43. Virojanadara, C.; Syväjarvi, M.; Yakimova, R.; Johansson, L.; Zakharov, A.; Balasubramanian, T., Homogeneous large-area graphene layer growth on 6H-SiC(0001). *Physical Review B* **2008**, *78* (24).
44. Z. Juang, C. W., W. Chen, C. Huang, J. Hwang, F. Chen, K. Leou, and C. Tsai, Synthesis of graphene on silicon carbide substrates at low temperature. *Carbon* **2009**, *47*, 2026-2031.
45. J. Chan, A. V., A. Pirkle, S. McDonnell, D. Hinojos, C. W. Magnuson, R. S. Ruoff, L. Colombo, R. M. Wallace and E. M. Vogel, <Reducing Extrinsic Performance-Limiting Factors in Graphene Grown by Chemical Vapor Deposition>. *ACS Nano* **2012**, *6* (4), 3224-3229.
46. Chen, S.; Ji, H.; Chou, H.; Li, Q.; Li, H.; Suk, J. W.; Piner, R.; Liao, L.; Cai, W.; Ruoff, R. S., Millimeter-Size Single-Crystal Graphene by Suppressing Evaporative Loss of Cu During Low Pressure Chemical Vapor Deposition. *Advanced Materials* **2013**.

47. L. Tao, J. L., H. Chou, M. Holt, R. S. Ruoff, D. Akinwande, <Synthesis of High Quality Monolayer Graphene at Reduced Temperature on Hydrogen-Enriched Evaporated Copper (111) Films>. *ACS Nano* **2012**, *6* (3), 2319-2325.
48. Hawaldar, R.; Merino, P.; Correia, M. R.; Bdkin, I.; Gracio, J.; Mendez, J.; Martin-Gago, J. A.; Singh, M. K., Large-area high-throughput synthesis of monolayer graphene sheet by Hot Filament Thermal Chemical Vapor Deposition. *Scientific reports* **2012**, *2*, 682.
49. Chen, S.; Cai, W.; Piner, R. D.; Suk, J. W.; Wu, Y.; Ren, Y.; Kang, J.; Ruoff, R. S., Synthesis and characterization of large-area graphene and graphite films on commercial Cu-Ni alloy foils. *Nano letters* **2011**, *11* (9), 3519-25.
50. Suk, J. W.; Lee, W. H.; Lee, J.; Chou, H.; Piner, R. D.; Hao, Y.; Akinwande, D.; Ruoff, R. S., Enhancement of the electrical properties of graphene grown by chemical vapor deposition via controlling the effects of polymer residue. *Nano letters* **2013**, *13* (4), 1462-7.
51. K. M. Daniels, B. D., R. Zhang, I. Chowdhury, A. Obe, J. Weidner, C. Williams, T.S. Sudarshan, M. V. S. Chandrashekar, <Graphene to Graphane: Novel Electrochemical Conversion>. **2010**.
52. Y. Wang, X. X., J. Lu, M. Lin, Q. Bao, B. Ozyilmaz, and K. P. Loh, Toward High Throughput Interconvertible Graphane-to-Graphene Growth and Patterning. *ACS Nano* **2010**, *4* (10), 6146-6152.
53. Y. Li, Z. Z., P. Shen, Z. Chen, Structural and Electronic Properties of Graphane Nanoribbons. *J. Phys. Chem. C* **2009**, *113*, 15043-15045.
54. Du, W.; Jiang, X.; Zhu, L., From graphite to graphene: direct liquid-phase exfoliation of graphite to produce single- and few-layered pristine graphene. *Journal of Materials Chemistry A* **2013**, *1* (36), 10592.
55. Xia, Z. Y.; Pezzini, S.; Treossi, E.; Giambastiani, G.; Corticelli, F.; Morandi, V.; Zanelli, A.; Bellani, V.; Palermo, V., The Exfoliation of Graphene in Liquids by Electrochemical, Chemical, and Sonication-Assisted Techniques: A Nanoscale Study. *Advanced Functional Materials* **2013**, n/a-n/a.
56. Indium Tin Oxide. *Wikipedia* (http://en.wikipedia.org/wiki/Indium_tin_oxide).
57. Jiang, G.; Lin, Z.; Chen, C.; Zhu, L.; Chang, Q.; Wang, N.; Wei, W.; Tang, H., TiO₂ nanoparticles assembled on graphene oxide nanosheets with high photocatalytic activity for removal of pollutants. *Carbon* **2011**, *49* (8), 2693-2701.
58. Pan, X.; Zhao, Y.; Liu, S.; Korzeniewski, C. L.; Wang, S.; Fan, Z., Comparing graphene-TiO₂ nanowire and graphene-TiO₂ nanoparticle composite photocatalysts. *ACS applied materials & interfaces* **2012**, *4* (8), 3944-50.
59. Sher Shah, M. S.; Park, A. R.; Zhang, K.; Park, J. H.; Yoo, P. J., Green synthesis of biphasic TiO₂-reduced graphene oxide nanocomposites with highly enhanced photocatalytic activity. *ACS applied materials & interfaces* **2012**, *4* (8), 3893-901.
60. Zhang, Y.; Zhang, N.; Tang, Z. R.; Xu, Y. J., Improving the photocatalytic performance of graphene-TiO₂ nanocomposites via a combined strategy of decreasing defects of graphene and increasing interfacial contact. *Physical chemistry chemical physics:PCCP* **2012**, *14* (25), 9167-75.
61. Kim, H.-i.; Moon, G.-h.; Monllor-Satoca, D.; Park, Y.; Choi, W., Solar Photoconversion Using Graphene/TiO₂Composites: Nanographene Shell on TiO₂Core versus TiO₂Nanoparticles on Graphene Sheet. *The Journal of Physical Chemistry C* **2012**, *116* (1), 1535-1543.

62. Manga, K. K.; Zhou, Y.; Yan, Y.; Loh, K. P., Multilayer Hybrid Films Consisting of Alternating Graphene and Titania Nanosheets with Ultrafast Electron Transfer and Photoconversion Properties. *Advanced Functional Materials* **2009**, *19* (22), 3638-3643.
63. Zhou, K.; Zhu, Y.; Yang, X.; Jiang, X.; Li, C., Preparation of graphene-TiO₂ composites with enhanced photocatalytic activity. *New Journal of Chemistry* **2011**, *35* (2), 353.
64. Cheng, P.; Yang, Z.; Wang, H.; Cheng, W.; Chen, M.; Shangguan, W.; Ding, G., TiO₂-graphene nanocomposites for photocatalytic hydrogen production from splitting water. *International Journal of Hydrogen Energy* **2012**, *37* (3), 2224-2230.
65. Lin, Y.; Geng, Z.; Cai, H.; Ma, L.; Chen, J.; Zeng, J.; Pan, N.; Wang, X., Ternary Graphene-TiO₂-Fe₃O₄ Nanocomposite as a Recollectable Photocatalyst with Enhanced Durability. *European Journal of Inorganic Chemistry* **2012**, *2012* (28), 4439-4444.
66. Wu, Y.; Zhang, X.; Jie, J.; Xie, C.; Zhang, X.; Sun, B.; Wang, Y.; Gao, P., Graphene Transparent Conductive Electrodes for Highly Efficient Silicon Nanostructures-Based Hybrid Heterojunction Solar Cells. *The Journal of Physical Chemistry C* **2013**, *117* (23), 11968-11976.
67. Peters, E. C.; Lee, E. J. H.; Burghard, M.; Kern, K., Gate dependent photocurrents at a graphene p-n junction. *Applied Physics Letters* **2010**, *97* (19), 193102.
68. Yan, K.; Wu, D.; Peng, H.; Jin, L.; Fu, Q.; Bao, X.; Liu, Z., Modulation-doped growth of mosaic graphene with single-crystalline p-n junctions for efficient photocurrent generation. *Nature communications* **2012**, *3*, 1280.
69. Sun, R.; Zhang, Y.; Li, K.; Hui, C.; He, K.; Ma, X.; Liu, F., Tunable photoresponse of epitaxial graphene on SiC. *Applied Physics Letters* **2013**, *103* (1), 013106.
70. Bernardi, M.; Palummo, M.; Grossman, J. C., Extraordinary sunlight absorption and one nanometer thick photovoltaics using two-dimensional monolayer materials. *Nano letters* **2013**, *13* (8), 3664-70.
71. Walker, K., Graphene Valley? Top 5 uses of Graphene that could change the world. *AZOnano Graphene Paint*, <http://www.azonano.com/article.aspx?ArticleID=3553>.
72. Zheng, H.; Neo, C. Y.; Ouyang, J., Highly efficient iodide/triiodide dye-sensitized solar cells with gel-coated reduce graphene oxide/single-walled carbon nanotube composites as the counter electrode exhibiting an open-circuit voltage of 0.90 V. *ACS applied materials & interfaces* **2013**, *5* (14), 6657-64.
73. G. Wang, W. X., and S. Zhuo, Nitrogen-doped graphene as low-cost counter electrode for high-efficiency dye-sensitized solar cells. *Electrochimica Acta* **2013**, *92*, 269-275.
74. Al-Mamun, M.; Kim, J.-Y.; Lee, K.-J.; Ko, Y.-H.; Lee, J.-H.; In, I.-S.; Lee, J.-W.; Sung, Y.-E.; Kim, S.-R., Highly electrocatalytic hybrid silver nanowire-graphene counter electrode for Co^{3+/2+} redox mediator based dye-sensitized solar cells. *Synthetic Metals* **2013**, *177*, 77-81.
75. M. Al-Mamun, J. K., Y. Sung, J. Lee, S. Kim, <Pt and TCO free hybrid bilayer silver nanowire-graphene counter electrode for dye-sensitized solar cells>. *Chemical Physics Letters* **2013**, *561-562*, 115-119.
76. H. Bi, W. Z., S. Sun, H. Cui, T. Lin, F. Huang, X. Xie and M. Jiang, <Graphene films decorated with metal sulfide nanoparticles for counter electrodes of dye-sensitized solar cells>. *Carbon* **2013**, *61*, 116-123.
77. Shanmugam, M.; Durcan, C.; Gedrim, R. J.; Bansal, T.; Yu, B., Oxygenated-graphene-enabled recombination barrier layer for high performance dye-sensitized solar cell. *Carbon* **2013**, *60*, 523-530.

78. B. Tang, G. H., H. Gao and Z. Shi, <Three-dimensional graphene network assisted high performance dye sensitized solar cells>. *Journal of Power Sources* **2013**, *234*, 60-68.
79. B. Ohtani, O. O. P.-M., D. Li and R. Abe, <What is Degussa (Evonik) P25? Crystalline composition analysis, reconstruction from isolated pure particles and photocatalytic activity test>. *Journal of Photochemistry and Photobiology A: Chemistry* **2010**, *216*, 179-182.
80. T. J. Bandosz, J. M., M. Seredych, M.S.Z. Islam, and R. Alfano, Photoactivity of S-doped nanoporous activated carbons: A new perspective for harvesting solar energy on carbon-based semiconductors. *Applied Catalysis A: General* **2012**, *445-446*, 159-165.
81. Hou, Y.; Zuo, F.; Dagg, A.; Feng, P., Visible light-driven alpha-Fe(2)O(3) nanorod/graphene/BiV(1)-xMoxO(4) core/shell heterojunction array for efficient photoelectrochemical water splitting. *Nano letters* **2012**, *12* (12), 6464-73.
82. Lv, X.-J.; Zhou, S.-X.; Zhang, C.; Chang, H.-X.; Chen, Y.; Fu, W.-F., Synergetic effect of Cu and graphene as cocatalyst on TiO2 for enhanced photocatalytic hydrogen evolution from solar water splitting. *Journal of Materials Chemistry* **2012**, *22* (35), 18542.
83. Novoselov, A. K. G. a. K. S., The rise of graphene. *Nature Materials* **2007**, *6*, 183-191.
84. Kholmanov, I. N.; Magnuson, C. W.; Aliev, A. E.; Li, H.; Zhang, B.; Suk, J. W.; Zhang, L. L.; Peng, E.; Mousavi, S. H.; Khanikaev, A. B.; Piner, R.; Shvets, G.; Ruoff, R. S., Improved electrical conductivity of graphene films integrated with metal nanowires. *Nano letters* **2012**, *12* (11), 5679-83.
85. Petrone, N.; Meric, I.; Hone, J.; Shepard, K. L., Graphene field-effect transistors with gigahertz-frequency power gain on flexible substrates. *Nano letters* **2013**, *13* (1), 121-5.
86. Y. D. Kim, M. B., J. Seo, Y. S. Kim, H. Kim, J. H. Lee, J. R. Ahn, S. W. Lee, S. Chun, Y. D. Park, <Focused-Laser-Enabled p-n Junctions in Graphene Field-Effect Transistors>. *ACS Nano* **2013**, *7* (7), 5850-5857.
87. S. Cheng, K. Z., H. R. Gutierrez, A. Gupta, N. Shen, P. C. Eklund, J. O. Sofo, J. Zhu, Reversible Fluorination of Graphene: towards a Two-Dimensional Wide Bandgap Semiconductor. **2010**.
88. F. Xia, H. Y. a. P. A., <The Interaction of Light and Graphene: Basics, Devices, and Applications>. *Proceedings of the IEEE* **2013**, *101* (7), 1717-1731.
89. A. L. M. Reddy, A. S., S. R. Gowda, H. Gullapalli, M. Dubey and P. M. Ajayan, <Synthesis Of Nitrogen-Doped Graphene Films for Lithium Battery Application>. *ACS Nano* **2010**, *4* (11), 6337-6342.
90. Li, Y.; Wang, J.; Li, X.; Geng, D.; Banis, M. N.; Li, R.; Sun, X., Nitrogen-doped graphene nanosheets as cathode materials with excellent electrocatalytic activity for high capacity lithium-oxygen batteries. *Electrochemistry Communications* **2012**, *18*, 12-15.
91. Wang, L.; He, X.; Li, J.; Gao, J.; Fang, M.; Tian, G.; Wang, J.; Fan, S., Graphene-coated plastic film as current collector for lithium/sulfur batteries. *Journal of Power Sources* **2013**, *239*, 623-627.
92. Stoller, M. D.; Park, S.; Zhu, Y.; An, J.; Ruoff, R. S., Graphene-based ultracapacitors. *Nano letters* **2008**, *8* (10), 3498-502.
93. B. Li, H. C., J. Shao, M. Qu, and J. Warner, Superparamagnetic Fe₃O₄ nanocrystals@graphene composites for energy storage devices. *Journal of Materials Chemistry* **2011**, *21*, 5069-5075.
94. Fan, Z.; Yan, J.; Zhi, L.; Zhang, Q.; Wei, T.; Feng, J.; Zhang, M.; Qian, W.; Wei, F., A three-dimensional carbon nanotube/graphene sandwich and its application as electrode in supercapacitors. *Adv Mater* **2010**, *22* (33), 3723-8.

95. Ouyang, W.; Sun, J.; Memon, J.; Wang, C.; Geng, J.; Huang, Y., Scalable preparation of three-dimensional porous structures of reduced graphene oxide/cellulose composites and their application in supercapacitors. *Carbon* **2013**, *62*, 501-509.
96. Xu, K.; Xu, C.; Xie, Y.; Deng, J.; Zhu, Y.; Guo, W.; Mao, M.; Xun, M.; Chen, M.; Zheng, L.; Sun, J., GaN nanorod light emitting diodes with suspended graphene transparent electrodes grown by rapid chemical vapor deposition. *Applied Physics Letters* **2013**, *103* (22), 222105.
97. Youn, D. H.; Yu, Y. J.; Choi, H.; Kim, S. H.; Choi, S. Y.; Choi, C. G., Graphene transparent electrode for enhanced optical power and thermal stability in GaN light-emitting diodes. *Nanotechnology* **2013**, *24* (7), 075202.
98. Son, D. I.; Kwon, B. W.; Park, D. H.; Seo, W. S.; Yi, Y.; Angadi, B.; Lee, C. L.; Choi, W. K., Emissive ZnO-graphene quantum dots for white-light-emitting diodes. *Nature nanotechnology* **2012**, *7* (7), 465-71.
99. Wu, H.; Wang, J.; Kang, X.; Wang, C.; Wang, D.; Liu, J.; Aksay, I. A.; Lin, Y., Glucose biosensor based on immobilization of glucose oxidase in platinum nanoparticles/graphene/chitosan nanocomposite film. *Talanta* **2009**, *80* (1), 403-6.
100. K. Zhou, Y. Z., X. Yang, J. Lou, C. Li, S. Luan, A novel hydrogen peroxide biosensor based on Au-graphene-HRP-chitosan biocomposites. *Electrochimica Acta* **2010**, *55*, 3055-3060.
101. Mao, S.; Yu, K.; Chang, J.; Steeber, D. A.; Ocola, L. E.; Chen, J., Direct growth of vertically-oriented graphene for field-effect transistor biosensor. *Scientific reports* **2013**, *3*, 1696.
102. Wang, R.; Higgins, D. C.; Hoque, M. A.; Lee, D.; Hassan, F.; Chen, Z., Controlled growth of platinum nanowire arrays on sulfur doped graphene as high performance electrocatalyst. *Scientific reports* **2013**, *3*, 2431.
103. Luo, Z.; Yuwen, L.; Bao, B.; Tian, J.; Zhu, X.; Weng, L.; Wang, L., One-pot, low-temperature synthesis of branched platinum nanowires/reduced graphene oxide (BPtNW/RGO) hybrids for fuel cells. *Journal of Materials Chemistry* **2012**, *22* (16), 7791.
104. (a) Byon, H. R.; Suntivich, J.; Shao-Horn, Y., Graphene-Based Non-Noble-Metal Catalysts for Oxygen Reduction Reaction in Acid. *Chemistry of Materials* **2011**, *23* (15), 3421-3428; (b) Jeon, I. Y.; Choi, H. J.; Choi, M.; Seo, J. M.; Jung, S. M.; Kim, M. J.; Zhang, S.; Zhang, L.; Xia, Z.; Dai, L.; Park, N.; Baek, J. B., Facile, scalable synthesis of edge-halogenated graphene nanoplatelets as efficient metal-free electrocatalysts for oxygen reduction reaction. *Scientific reports* **2013**, *3*, 1810.
105. Potts, J. R.; Shankar, O.; Du, L.; Ruoff, R. S., Processing–Morphology–Property Relationships and Composite Theory Analysis of Reduced Graphene Oxide/Natural Rubber Nanocomposites. *Macromolecules* **2012**, *45* (15), 6045-6055.
106. Shen, B.; Zhai, W.; Tao, M.; Lu, D.; Zheng, W., Chemical functionalization of graphene oxide toward the tailoring of the interface in polymer composites. *Composites Science and Technology* **2013**, *77*, 87-94.
107. S. Chandrasekaran, G. F., L. Prado, F. Toelle, R. Mulhaupt, K. Schulte, Thermally reduced graphene oxide acting as a trap for multiwall carbon nanotubes in bi-filler epoxy composites. *Composites: Part A* **2013**, *49*, 51-57.
108. Park, O.-K.; Hwang, J.-Y.; Goh, M.; Lee, J. H.; Ku, B.-C.; You, N.-H., Mechanically Strong and Multifunctional Polyimide Nanocomposites Using Amimophenyl Functionalized Graphene Nanosheets. *Macromolecules* **2013**, *46* (9), 3505-3511.

109. Yousefi, N.; Gudarzi, M. M.; Zheng, Q.; Lin, X.; Shen, X.; Jia, J.; Sharif, F.; Kim, J.-K., Highly aligned, ultralarge-size reduced graphene oxide/polyurethane nanocomposites: Mechanical properties and moisture permeability. *Composites Part A: Applied Science and Manufacturing* **2013**, *49*, 42-50.
110. Chen, M.; Tao, T.; Zhang, L.; Gao, W.; Li, C., Highly conductive and stretchable polymer composites based on graphene/MWCNT network. *Chemical communications* **2013**, *49* (16), 1612-4.
111. Fryczkowski, R.; Gorczowska, M.; Ślusarczyk, C.; Fryczkowska, B.; Janicki, J., The possibility of obtaining graphene/polymer composites from graphene oxide by a one step process. *Composites Science and Technology* **2013**, *80*, 87-92.
112. Super-tall (30km) carbon structures (graphene and nanotube mesh). *NVIREUK*, <http://nvireuk.wordpress.com/category/graphene-uses/>.
113. Kim, Y.; Lee, J.; Yeom, M. S.; Shin, J. W.; Kim, H.; Cui, Y.; Kysar, J. W.; Hone, J.; Jung, Y.; Jeon, S.; Han, S. M., Strengthening effect of single-atomic-layer graphene in metal-graphene nanolayered composites. *Nature communications* **2013**, *4*, 2114.
114. HEAD Tennis Racquet-Graphene | New Dimension for Racquet Weight Distribution. *Khelmart-Wordpress Blog* **October 19, 2013**, *October 10, 2013*.
115. Xu, C.; Cui, A.; Xu, Y.; Fu, X., Graphene oxide–TiO₂ composite filtration membranes and their potential application for water purification. *Carbon* **2013**, *62*, 465-471.
116. NVIREUK, Graphene drinking straw. <http://nvireuk.wordpress.com/category/graphene-uses/>.
117. Gao, H.; Sun, Y.; Zhou, J.; Xu, R.; Duan, H., Mussel-inspired synthesis of polydopamine-functionalized graphene hydrogel as reusable adsorbents for water purification. *ACS applied materials & interfaces* **2013**, *5* (2), 425-32.
118. Yang, Y.; Xie, Y.; Pang, L.; Li, M.; Song, X.; Wen, J.; Zhao, H., Preparation of reduced graphene oxide/poly(acrylamide) nanocomposite and its adsorption of Pb(II) and methylene blue. *Langmuir:the ACS journal of surfaces and colloids* **2013**, *29* (34), 10727-36.
119. Bi, H.; Xie, X.; Yin, K.; Zhou, Y.; Wan, S.; He, L.; Xu, F.; Banhart, F.; Sun, L.; Ruoff, R. S., Spongey Graphene as a Highly Efficient and Recyclable Sorbent for Oils and Organic Solvents. *Advanced Functional Materials* **2012**, *22* (21), 4421-4425.
120. Sun, X.; Liu, Z.; Welsher, K.; Robinson, J. T.; Goodwin, A.; Zaric, S.; Dai, H., Nano-Graphene Oxide for Cellular Imaging and Drug Delivery. *Nano research* **2008**, *1* (3), 203-212.
121. Rana, V. K.; Choi, M.-C.; Kong, J.-Y.; Kim, G. Y.; Kim, M. J.; Kim, S.-H.; Mishra, S.; Singh, R. P.; Ha, C.-S., Synthesis and Drug-Delivery Behavior of Chitosan-Functionalized Graphene Oxide Hybrid Nanosheets. *Macromolecular Materials and Engineering* **2011**, *296* (2), 131-140.
122. Shen, J.; Zhu, Y.; Yang, X.; Li, C., Graphene quantum dots: emergent nanolights for bioimaging, sensors, catalysis and photovoltaic devices. *Chemical communications* **2012**, *48* (31), 3686-99.
123. Yang, K.; Zhang, S.; Zhang, G.; Sun, X.; Lee, S. T.; Liu, Z., Graphene in mice: ultrahigh in vivo tumor uptake and efficient photothermal therapy. *Nano letters* **2010**, *10* (9), 3318-23.
124. Robinson, J. T.; Tabakman, S. M.; Liang, Y.; Wang, H.; Casalogue, H. S.; Vinh, D.; Dai, H., Ultrasmall reduced graphene oxide with high near-infrared absorbance for photothermal therapy. *Journal of the American Chemical Society* **2011**, *133* (17), 6825-31.
125. Walker, K., Graphne Valley? Top 5 uses of Graphene that could change the world. *AZOnano Graphene in Living Tissue*, <http://www.azonano.com/article.aspx?ArticleID=3553>.

126. Templeton, G., Geek Answers: Why aren't we building a space elevator? *Geek.com* **September 17, 2013**, October 29, 2013 (<http://www.geek.com/science/geek-answers-why-arent-we-building-a-space-elevator-1570891/>).
127. Holmes, K., Turn Your Clothes Into Wearable Computers With Graphene. *the creators project* **May 4, 2012**, November 12, 2013 (<http://thecreatorsproject.vice.com/blog/turn-your-clothes-into-wearable-computers-with-graphene>).
128. Inventory of U.S. Greenhouse Gas Emissions and Sinks: 1990-2012. *EPA Executive Summary*.
129. Sources of Greenhouse Gas Emissions: Total U.S. Greenhouse Gas Emissions by Economic Sector in 2012. *EPA* **2014**, <http://www.epa.gov/climatechange/ghgemissions/sources/electricity.html>.
130. Xue-Ping Gao and Han-Xi Yang, Multi-electron reaction materials for high energy density batteries. *Energy & Environmental Science* **2009**, 3, 174-189.
131. (a) A.K. Padhi, K.S. Nanjundaswamy, J.B. Goodenough, Phospho-olivines as positive-electrode materials for rechargeable lithium batteries. *Journal of The Electrochemical Society* **1997**, 144 (4), 1188-1194; (b) A.K. Padhi, K.S. Nanjundaswamy, C. Masquelier, S. Okada, J.B. Goodenough, Effect of structure on the Fe³⁺/Fe²⁺ redox couple in iron phosphates. *Journal of The Electrochemical Society* **1997**, 144 (5), 1609-1613.
132. K. Saravanan, P. Balaya, M.V. Reddy, B.V.R. Chowdari, and J.J. Vittal, Morphology controlled synthesis of LiFePO₄/C nanoplates for Li-ion batteries. *Energy & Environmental Science* **2010**, 3, 457-464.
133. C. Delacourt, P. Poizot, J. Tarascon and C. Masquelier, The existence of a temperature-driven solid solution in Li_xFePO₄ for 0 ≤ x ≤ 1 *Nature Materials* **2005**, 4, 254-260.
134. S.F. Yang, P.Y. Zavalij, and M.S. Whittingham, Hydrothermal synthesis of lithium iron phosphate cathodes. *Electrochemistry Communications* **2001**, 3 (9), 505-508.
135. S.F. Yang, Y.N. Song, K. Ngala, P.Y. Zavalij, and M.S. Whittingham, Performance of LiFePO₄ as lithium battery cathode and comparison with manganese and vanadium oxides. *Journal of Power Sources* **2003**, 119, 239-246.
136. Y. Xia, W. Zhang, H. Huang, Y. Gan, Z. Xiao, L. Qian, and X. Tao, Biotemplating of phosphate hierarchical rechargeable LiFePO₄/C spirulina microstructures. *Journal of Materials Chemistry* **2011**, 21, 6498-6501.
137. J. Ni, M. Morishita, Y. Kawabe, M. Watada, N. Takeichi, and T. Sakai, Hydrothermal preparation of LiFePO₄ nanocrystals mediated by organic acid. *Journal of Power Sources* **2010**, 195, 2877-2882.
138. K. Dokko, S. Koizumi, H. Nakano, and K. Kanamura, Particle morphology, crystal orientation, and electrochemical reactivity of LiFePO₄ synthesized by the hydrothermal method at 443 K. *Journal of Materials Chemistry* **2007**, 17, 4803-4810.
139. (a) S. Zhu, H. Zhou, T. Miyoshi, M. Hibino, I. Honma, and M. Ichihara, Self-Assembly of the Mesoporous Electrode Material Li₃Fe₂(PO₄)₃. *Advanced Materials* **2004**, 16 (22), 2012-2017; (b) M. Estermann, L.B. McCusker, A Synthetic Gallophosphate Molecular Sieve with a 20-Tetrahedral-Atom Pore Opening. *Nature* **1991**, 352, 320-323.
140. M. Sato, S. Tajimi, H. Okawa, K. Uematsu, K. Toda, Preparation of iron phosphate cathode material of Li₃Fe₂(PO₄)₃ by hydrothermal reaction and thermal decomposition processes. *Solid State Ionics* **2002**, 152-153, 247-251.

141. K. Dokko, S. Koizumi, K. Shiraishi, and K. Kanamura, Electrochemical properties of LiFePO₄ prepared via hydrothermal route. *Journal of Power Sources* **2007**, *165*, 656-659.
142. K. Dokko, S. Koizumi, H. Nakano, and K. Kanamura, Particle morphology, crystal orientation, and electrochemical reactivity of LiFePO₄ synthesized by the hydrothermal method at 443 K. *J. Mater. Chem.* **2007**, *17*, 4803-4810.
143. D. Rangappa, K. Sone, T. Kudo, and I. Honma, Directed growth of nanoarchitected LiFePO₄ electrode by solbothermal synthesis and their cathode properties. *Journal of Power Sources* **2010**, *195*, 6167-6171.
144. K. Dokku, S. Koizumi, H. Nakano and K. Kanamura, Particle morphology, crystal orientation, and electrochemical reactivity of LiFePO₄ synthesized by the hydrothermal method at 443 K. *Journal of Materials Chemistry* **2007**, *17* (4803-4810).
145. B. Guo, H. Raun, C. Zheng, H. Fei ad M. Wei, Heirarchical LiFePO₄ with a controllable growth of the (010) facet for lithium-ion batteries. *Scientific reports* **2013**, *3*:2788, 1-6.
146. K. Saravanan, P. Balaya, M.V. Reddy, B.V.R. Chowdari and J.J. Vittal, Morphology controlled synthesis of LiFePO₄/C nanoplates for Li-ion batteries. *Energy & Environmental Science* **2010**, *3* (457-464).
147. Y. Zhao, L. Peng, B. Liu and G. Yu, Single-Crysstalline LiFePO₄ Nanosheets for High-Rate Li-Ion Batteries. *Nano letters* **2014**, *14*, 2849-2853.
148. Q. Wang, W. Zhang, Z. Yang, S. Weng and Z. Jin, Solvothermal synthesis of hierarchical LiFePO₄ microflowers as cathode materials for lithium ion batteries. *Journal of Power Sources* **2011**, *196*, 10176-10182.
149. (a) H. Colfen and S. Mann, Higher-Order Organization bby Mesoscale Self-Assembly and Transformation of Hybrid Nanostructures. *Angewandte Chemie International Edition* **2003**, *42*, 2350-2365; (b) E. Matijevic, Peparation and Properties of Uniform Size Colloids. *Chem. Mater.* **1993**, *5*, 412-426; (c) Y. Zhang, Y. Liu, S. Fu, F. Guo, and Y. Qian, Morphology-controlled synthesis of Co₃O₄ crystals by soft chemical method. *Materials Chemistry and Physics* **2007**, *104*, 166-171; (d) S.H. Kim, B.S. Choi, K. Kang, Y. Choi, and S.I. Yang, Low temperature synthesis and growth mechanism of Ag nanowires. *Journal of Alloys and Compounds* **2007**, *433*, 261-264; (e) Y. Chang, Y. Lu, and K. Chou, Diameter Control of Silver Nanowires by Chloride Ions and Its Application as Transparent Conductive Coating. *Chem. Lett.* **2011**, *40*, 1352-1353.
150. Y. Zhao, L. Peng, B. Liu and G. Yu, Single-Crystalline LiFePO₄ Nanosheets for High-Rate Li-Ion Batteries. *Nano letters* **2014**, *14*, 2849-2853.
151. (a) X. Yin, K. Huang, S. Liu, H. Wang, H. Wang, Preparation and characterization of Na-doped LiFePO₄/C composites as cathode materials for lithium-ion batteries. *Journal of Power Sources* **2010**, *195*, 4308-4312; (b) Y. Chen and J. Chen, A Study of Electrochemical Performance of LiFePO₄/C Composites Doped with Na and V. *Int. J. Electrochem. Sci.* **2012**, *7*, 8128-8139.
152. C. Nan, J. Lu, C. Chen, Q. Peng, and Y. Li, Solvothermal synthesis of lithium iron phosphate nanoplates. *Journal of Materials Chemistry* **2011**, *21*, 9994-9996.
153. C.M. Julien, K. Zaghib, A. Mauger, M. Massot, A. Ait-Saleh, M. Selmane, and F. Gendron, Characterization of the carbon coating onto LiFePO₄ particles used in lithium batteries *Journal of Applied Physics* **2006**, *100* (6), 063511.
154. T.T. Nagaura, Lithium ion rechargeable battery. *Progress in Batteries & Solar Cells* **1990**, *9* (209).

155. J. Molenda and M. Molenda, Composite Cathode Material for Li-Ion Batteries Based on LiFePO₄ System. *Metal, Ceramic and Polymeric Composites for Various Uses* **2011**, Chapter 30, John Cuppoletti, July 20, 2011.
156. J.B. Goodenough and K. Park, The Li-Ion Rechargeable Battery: A Perspective. *J. Am. Chem. Soc.* **2013**, *135*, 1167-1176.
157. P. P. Prosini, M. Lisi, D. Zane, and M. Pasquali, Determination of the chemical diffusion coefficient of lithium in LiFePO₄. *Solid State Ionics* **2002**, *148*, 45-51.
158. A.V. Churikov, A.V. Ivanishchev, I.A. Ivanishcheva, V.O. Sycheva, N.R. Khasonova, and E.V. Antipov, Determination of lithium diffusion coefficient in LiFePO₄ electrode by galvanostatic and potentiostatic intermittent titration techniques. *Electrochimica Acta* **2010**, *55*, 2939-2950.
159. A.K. Padhi, K.S. Nanjundaswamy, and J.B. Goodenough, Phospho-olivines as Positive-Electrode Materials for Rechargeable Lithium Batteries. *J. Electrochem. Soc.* **1997**, *144* (4), 1188-1194.
160. H. Gao, L. Jiao, J. Yang, Z. Qi, Y. Wang, and H. Yuan, High rate capability of Co-doped LiFePO₄/C. *Electrochimica Acta* **2013**, *97*, 143-149.
161. J. Song, G. Shao, M. Shi, Z. Ma, W. Song, C. Wang, and S. Liu, The effect of doping Co on the electrochemical properties of LiFePO₄/C nanoplatees synthesized by solvothermal route. *Solid State Ionics* **2013**, *253*, 39-46.
162. S. Novikova, S. Yaroslavtsev, V. Rusakov, T. Kulova, A. Skundin, and A. Yaroslavtsev, LiFe_{1-x}M^{II}xPO₄/C (M^{II} = Co, Ni, Mg) as cathode materials for lithium-ion batteries. *Electrochimica Acta* **2014**, *122*, 180-186.
163. J. Wang and X. Sun, Understanding and recent development of carbon coating on LiFePO₄ cathode materials for lithium-ion batteries. *Energy & Environmental Science* **2012**, *5*, 5163.
164. M.M. Doeff, Y. Hu, F. McLarnon, and R. Kostecki, Effect of Surface Carbon Structure on the Electrochemical Performance of LiFePO₄. *Lawrence Berkeley National Lab and the University of California* **2003**, 1-14.
165. S. Hong, D.H. Kim, K.Y. Chung, W. Chang, J. Yoo, and J. Kim, Toward uniform and ultrathin carbon layer coating on lithium iron phosphate using liquid carbon dioxide for enhanced electrochemical performance. *Journal of Power Sources* **2014**, *262*, 219-223.
166. X. Qin, J. Wang, J. Xie, F. Li, L. Wen and X. Wang, Hydrothermally synthesized LiFePO₄ crystals with enhanced electrochemical properties: simultaneous suppression of crystal growth along [010] and antisite defect formation. *Phys. Chem. Chem. Phys.* **2012**, *14*, 269-2677.
167. Y. Tao, X. Xie, W. Lv, D. Tang, D. Kong, Z. Huang, H. Nishihara, R. Ishii, B. Li, D. Golberg, F. Kang, T. Kyotani, and Q. Yang, Towards ultrahigh volumetric capacitance: graphene derived highly dense but porous carbons for supercapacitors. *Scientific reports* **2013**, *3* (2975), 1-8.
168. Y. Zhang, W. Wang, P. Li, Y. Fu, and X. Ma, A simple solvothermal route to synthesize graphene-modified LiFePO₄ cathode for high power lithium ion batteries. *Journal of Power Sources* **2012**, *210*, 47-53.
169. J. Jegal, K. Kim, M. Kim, and K. Kim, A lithium iron phosphate/nitrogen-doped reduced graphene oxide nanocomposite as a cathode material for high-power lithium ion batteries. *J. Mater. Chem. A* **2014**, *2*, 9594-9599.
170. L. Hu, F. Wu, C. Lin, A. Khlobystov and L. Li, Graphene-modified LiFePO₄ cathode for lithium ion battery beyond theoretical capacity. *Nature communications* **2013**, *4*:1687, 1-7.
171. J. Liu et al., Lithium ion batteries with titania/graphene anodes. *US 8450014 B2* **2013**, Grant.

172. A.S. Andersson and J.O. Thomas, The source of first-cycle capacity loss in LiFePO₄. *Journal of Power Sources* **2001**, 97-98, 498-502.
173. P.P. Prosini, D. Zane, and M. Pasquali, Improved electrochemical performance of a LiFePO₄-based composite cathode. *Electrochimica Acta* **2001**, 46, 3517-3523.
174. J. Popovic, R. Demir-Cakan, J. Tornow, M. Morcrette, D.S. Su, R. Schlogl, M. Antonietti, and M. Titirici, LiFePO₄ Mesocrystals for Lithium-ion Batteries. *small* **2011**, 7 (8), 1127-1135.
175. Hyundai Offers ix35 Fuel Cell Hydrogen-powered Electric Vehicle to Retail Customers in 2014. *Hyundai* **2015**, April 8, 2015, <http://www.hyundai.com.au/about-hyundai/news/articles/hyundai-offers-ix35-fuel-cell-hydrogen-powered-electric-vehicle-to-retail-customers-in-2014>.
176. A.J. Bard, R. Parsons, and J. Jordan (ed.), Standard Potentials in Aqueous Solution. *Dekker, New York, 1985*.
177. Fuel Cell Power. *Future Energies* **2006**, (July 8, 2015), <http://www.futureenergies.com/modules.php?op=modload&name=News&file=article&sid=959>.
178. Brett, Christopher M. A. and Brett, Ana Maria Oliveira, *Electrochemistry Principles, Methods, and Applications*. New York: Oxford University Press, 1993, p. 2-4.
179. N.S. Parimi, Y. Umasankar, P. Atanassov, and R.P. Ramasamy, Kinetic and Mechanistic Parameters of Laccase Catalyzed Direct Electrochemical Oxygen Reduction Reaction. *ACS Catalysis* **2012**, 2, 38-44.
180. I. Jeon, H. Choi, M. Choi, J. Seo, S. Jung, M. Kim, S. Zhang, L. Zhang, Z. Xia, L. Dai, N. Park, and J. Baek, Facile, scalable synthesis of edge-halogenated graphene nanoplatelets as efficient metal-free electrocatalysts for oxygen reduction reaction. *Scientific reports* **2013**, 3 (1810), DOI: 10.1038/srep01810.
181. Z. Chen, D. Higgins, H. Tao, R. Hsu, and Z. Chen, Highly Active Nitrogen-Doped Carbon Nanotubes for Oxygen Reaction Reaction in Fuel Cell Applications. *J. Phys. Chem. C* **2009**, 113, 21008-21013.
182. S. Sun, D. Yang, D. Villers, G. Zhang, E. Sacher, and J.P. Dodelet, Template- and Surfactant-free Room Temperature Synthesis of Self-Assembled 3D Pt Nanoflowers from single-Crystal Nanowires. *Adv. Mater.* **2008**, 20, 571-574.
183. M. Carmo, M. Linardi, and J.G.R. Poco, Characterization of nitric acid functionalized carbon black and its evaluation as electrocatalyst support for direct methanol fuel cell applications. *Applied Catalysis A: General* **2009**, 355 (1-2), 132-138.
184. J. Chen, T. Herricks, M. Geissler, and Y. Xia, Single-Crystal Nanowires of Platinum Can Be Synthesized by Controlling the Reaction Rate of a Polyol Process. *Journal of the American Chemical Society* **2004**, 126, 10854-10855.
185. S. Sun, D. Yang, G. Zhang, E. Sacher, and J.P. Dodelet, Synthesis and Characterization of Platinum Nanowire-Carbon Nanotube Heterostructures. *Chem. Mater.* **2007**, 19, 6376-6378.
186. S. Sun, G. Zhang, Y. Zhong, H. Liu, R. Li, Z. Zhou, and X. Sun, Ultrathin single crystal Pt nanowires grown on N-doped carbon nanotubes. *Chem. Commun.* **2009**, 7048-7050.
187. Z. Luo, L. Yuwen, B. Bao, J. Tian, X. Zhu, L. Weng, and L. Wang, One-pot, low-temperature synthesis of branched platinum nanowires/reduced graphene oxide (BPtNW/RGO) hybrids for fuel cells. *J. Mater. Chem.* **2012**, 22, 7791-7796.

188. R. Wang, D. Higgins, M. oque, D. Lee, F. Hassan, and Z. Chen, Controlled Growth of Platinum Nanowire Arrays of Sulfur Doped Graphene as High Performance Electrocatalyst. *Scientific reports* **2013**, *3*, 2431.
189. L. Chen, L. Kuai, and B. Geng, Shell structure-enhanced electrocatalytic performance of Au-Pt core-shell catalyst. *CrystEngComm* **2013**, *10.1039/c3ce27058k*.
190. S. Sun, F. Jaouen, and J.P. Dodelet, Controlled Growth of Pt Nanowires on Carbon Nanospheres and Their Enhanced Performance as Electrocatalysts in PEM Fuel Cells. *Adv. Mater.* **2008**, *20*, 3900-3904.
191. H. Meng, F. Xie, J. Chen, S. Sun and P.K. Shen, Morphology controllable growth of Pt nanoparticles/nanowires on carbon powders and its application as novel electro-catalyst for methanol oxidation. *Nanoscale* **2011**, *3*, 5041-5048.
192. Z.W. Chen, M. Waje, W.Z. Li, Y.S. Yan, Supportless Pt and PtPd Nanotubes as Electrocatalysts for Oxygen-Reduction Reactions. *Angew. Chem.* **2007**, *119* (4138).
193. B.Y. Xia, H.B. Wu, N. Li, Y. Yan, X.W. Lou, and X. Wang, One-Pot Synthesis of Pt-Co Alloy Nanowire Assemblies with Tunable Composition and Enhanced Electrocatalytic Properties. *Agnew. Chem. Int. Ed.* **2015**, *54*, 1-6.
194. Y. Huang, Y. Liu, Z. Yang, J. Jia, X. Li, Y. Luo, and Y. Fang, Synthesis of yolk/shell Fe₃O₄-polydopamine-graphene-Pt nanocomposite with high electrocatalytic activity for fuel cells. *Journal of Power Sources* **2014**, *246*, 868-875.
195. M. Lopez-Haro, L. Dubau, L. Guetaz, P. Bayle-Guillemaud, M. Chatenet, J. Andre, N. Caque, E. Rossinot, and F. Maillard, Atomic-scale structure and composition of Pt₃Co/C nanocrystallites during real PEMFC operation: A STEM-EELS study. *Applied Catalysis B: Environmental* **2014**, *152-153*, 300-308.
196. L. Ding, G. Li, Z. Wang, Z. Liu, H. Liu, and Y. Tong, Porous Ni@Pt Core-Shell Nanotube Array Electrocatalyst with High Activity and Stability for Methanol Oxidation. *Chem. Eur. J.* **2012**, *18*, 8386-8391.
197. E. Broaddus, A. Wedell, and S.A. Gold, Formic Acid Electrooxidation by a Platinum Nanotubule Array Electrode. *International Journal of Electrochemistry* **2013**, *2013* (Article ID 424561), 7 pages.
198. J.R.C. Salgado, E. Antolini, and E.R. Gonzalez, Preparation of Pt-Co/C electrocatalysts by reduction with borohydride in acid and alkaline media: the effect on the performance of the catalyst. *Journal of Power Sources* **2004**, *138*, 56-60.
199. L. Xiong, A.M. Kannan, and A. Manthiram, Pt-M (M = Fe, Co, Ni and Cu) electrocatalysts synthesized by an aqueous route for proton exchange membrane fuel cells. *Electrochemistry Communications* **2002**, *4*, 898-903.
200. J.R.C. Salgado, E. Antolini, and E.R. Gonzalez, Carbon supported Pt₇₀Co₃₀ electrocatalyst prepared by the formic acid method for the oxygen reduction reaction in polymer electrolyte fuel cells. *Journal of Power Sources* **2005**, *141*, 13-18.
201. M.V. Naseh, Y. Mortazavi, O.A. Sahraei, F. Pourfayaz, and S.M. Sedghi, Functionalization of Carbon Nanotubes Using Nitric Acid Oxidation and DBD Plasma. *World Academy of Science, Engineering and Technology* **2009**, *49*, 177-199.
202. Y. Zhou, T. Olson, S. Pylypenko, J. Bult, H. Dinh, T. Gennett, Z. Shao, and R. O'Hayre, Enhancement of Pt and Pt-alloy fuel cell catalyst activity and durability via nitrogen-modified carbon supports. *Energy & Environmental Science* **2010**, *3*, 1437-1446.

203. J.R.C. Salgado, E. Antolini, and E.R. Gonzalez, Preparation of Pt-Co/C electrocatalysts by reduction with borohydride in acid and alkaline media: the effect on the performance of the catalyst. *Journal of Power Sources* **2004**, *138* (1-2), 56-60.
204. K.J. Carroll et al., Annealing of amorphous Fe_xCo_{100-x} nanoparticles synthesized by a modified aqueous reduction using NaBH₄. *Journal of Applied Physics* **2010**, *107* (9), 09A303.
205. J.D. Hoefelmeyer, K. Niesz, G.A. Somorjai, and T.D. Tilley, Radial anisotropic growth of rhodium nanoparticles. *Nano letters* **2005**, *20*, 435-438.
206. S. Sun, F. Jaouen, and J.P. Dodelet, Controlled Growth of Pt Nanowires on Carbon Nanospheres and Their Enhanced Performance as Electrocatalysts in PEM Fuel Cells. *Advanced Materials* **2008**, *20*, 3900-3904.
207. A.K. Shukla, M. Neergat, P. Bera, V. Jayaram, and M.S. Hegde, An XPS study of binary and ternary alloys of transition metals with platinized carbon and its bearing upon oxygen electroreduction in direct methanol fuel cells. *Journal of Electroanalytical Chemistry* **2001**, *504*, 111-119.
208. A.L. Ocampo, R.H. Castellanos, and P.J. Sebastian, Kinetic Study of the Oxygen Reduction Reaction on Ru_y(CO)_n in Acid Medium with Different Concentrations of Methanol. *Journal of New Materials for Electrochemical Systems* **2002**, *5*, 163-168.
209. E. Antolini, J.R.C. Salgado, and E.R. Gonzalez, The stability of Pt-M (M=first row transition metal) alloy catalysts and its effect on the activity in low temperature fuel cells: A literature review and tests on a Pt-Co catalyst. *Journal of Power Sources* **2006**, *160*, 957-968.